NASA TECHNICAL NOTE

NASA TN D-7272

NASA TN D-7272

STABILITY ANALYSIS AND TREND STUDY OF A BALLOON TETHERED IN A WIND, WITH EXPERIMENTAL COMPARISONS

by L. Tracy Redd, Samuel R. Bland, and Robert M. Bennett

Langley Research Center
Hampton, Va. 23665

NATIONAL AERONAUTICS AND SPACE ADMINISTRATION • WASHINGTON, D. C. • OCTOBER 1973

1 Report No	2 Government Accession No	3 Recipient's Catalog No
NASA TN D-7272		

4 Title and Subtitle	5 Report Date
STABILITY ANALYSIS AND TREND STUDY OF A BALLOON TETHERED IN A WIND, WITH EXPERIMENTAL COMPARISONS	October 1973
	6 Performing Organization Code

7 Author(s)	8 Performing Organization Report No
L. Tracy Redd, Samuel R. Bland, and Robert M. Bennett	L-8523
	10 Work Unit No
	501-22-04-01

9 Performing Organization Name and Address	11 Contract or Grant No
NASA Langley Research Center Hampton, Va. 23665	
	13 Type of Report and Period Covered
	Technical Note

12 Sponsoring Agency Name and Address	14 Sponsoring Agency Code
National Aeronautics and Space Administration Washington, D.C. 20546	

15 Supplementary Notes

Technical Film Supplement L-1118 available on loan.

16 Abstract

A stability analysis and trend study for a balloon tethered in a steady wind are presented. The linearized, stability-derivative type analysis includes balloon aerodynamics, buoyancy, mass (including apparent mass), and static forces resulting from the tether cable.

The analysis has been applied to a balloon 7.64 m in length, and the results are compared with those from tow tests of this balloon. This comparison shows that the analysis gives reasonable predictions for the damping, frequencies, modes of motion, and stability boundaries exhibited by the balloon.

A trend study for the 7.64-m balloon was made to illustrate how the stability boundaries are affected by changes in individual stability parameters. The trends indicated in this study may also be applicable to many other tethered-balloon systems.

17 Key Words (Suggested by Author(s))	18 Distribution Statement
Tethered balloon Stability analysis Trend studies	Unclassified – Unlimited

19. Security Classif (of this report)	20 Security Classif (of this page)	21 No of Pages	22 Price*
Unclassified	Unclassified	109	Domestic, $4.25 Foreign, $6.75

*For sale by the National Technical Information Service, Springfield, Virginia 22151

CONTENTS

STABILITY ANALYSIS AND TREND STUDY OF A BALLOON TETHERED IN A WIND, WITH EXPERIMENTAL COMPARISONS

By L. Tracy Redd, Samuel R. Bland,
and Robert M. Bennett
Langley Research Center

SUMMARY

A stability analysis and trend study for a balloon tethered in a steady wind are presented. The linearized, stability-derivative type analysis includes balloon aerodynamics, buoyancy, mass (including apparent mass), and static forces resulting from the tether cable.

The analysis has been applied to a balloon 7.64 m in length, and the results are compared with those from tow tests of this balloon. This comparison shows that the analysis gives reasonable predictions for the damping, frequencies, modes of motion, and stability boundaries exhibited by the balloon.

A trend study for the 7.64-m balloon was made to illustrate how the stability boundaries are affected by changes in individual stability parameters. The trends indicated in this study may also be applicable to many other tethered-balloon systems.

INTRODUCTION

A tethered balloon is useful for a number of purposes, such as supporting antennas or providing an aerial platform. Such operations are often impaired by the occurrence of dynamic instabilities, especially during strong wind conditions. Although information relating to the stability of towed and tethered bodies, including balloons, has been published (see refs. 1 to 4, for example), a systematic procedure for the analysis of tethered-balloon stability is needed. In an attempt to fill this need, the NASA Langley Research Center undertook a general research study to develop improved techniques for predicting the stability of tethered balloons. The scope of this study includes: derivation of the stability equations, adaptation of these equations for use in computer programs, formulation of methods for determining stability derivatives, verification of the stability analysis by the use of tow-test experiments, and an investigation of the effects of changes in stability parameters on the balloon stability boundaries.

Portions of the tethered-balloon stability study are given in references 5 to 8. References 5 and 6 describe the methods used to obtain the physical properties of the tow-test balloon. Reference 7 contains a description of the computer programs used for calculating and plotting the analytical results. A brief overview of the complete study is given in reference 8.

The purpose of the present paper is to derive the equations of motion for a tethered balloon and to assess the accuracy of these equations by comparing the analytical results with results from tow-test experiments. The equations of motion include balloon aerodynamics, apparent mass, structural weight, buoyancy, and static forces resulting from the tether cable. An additional purpose is to present a trend study which illustrates the effects of changes in balloon properties on the stability boundaries.

SYMBOLS

a	distance along balloon center line from nose to reference point, m (see fig. 4)
B	buoyancy force, N
C_D	drag coefficient, $\left.\frac{D}{\rho V_\infty{}^2 S/2}\right\|_t$
C_{D_c}	tether-cable drag coefficient
C_L	lift coefficient, $\left.\frac{L}{\rho V_\infty{}^2 S/2}\right\|_t$
C_l	rolling-moment coefficient, $\left.\frac{M_{X,A}}{\rho V_\infty{}^2 S\bar{c}/2}\right\|_t$
C_m	pitching-moment coefficient, $\left.\frac{M_{Y,A}}{\rho V_\infty{}^2 S\bar{c}/2}\right\|_t$
C_n	yawing-moment coefficient, $\left.\frac{M_{Z,A}}{\rho V_\infty{}^2 S\bar{c}/2}\right\|_t$
C_Y	side-force coefficient, $\left.\frac{F_{Y,A}}{\rho V_\infty{}^2 S/2}\right\|_t$
$\bar{c}$	balloon length, m

D aerodynamic drag force, N

d_c tether-cable diameter, m

F_X, F_Y, F_Z external forces acting on balloon parallel to X-, Y-, and Z-axes, respectively, N (see fig. 2)

$F_{X'}, F_{Y'}, F_{Z'}$ external forces acting on balloon parallel to X'-, Y'-, and Z'-axes, respectively, N (see fig. 1 for axis system)

$f = \cos \gamma$

h_{br} component of distance from reference point to center of buoyancy, positive for center of buoyancy below reference point, m (see fig. 4)

h_{cg} component of distance from reference point to center of mass, positive for center of mass below reference point, m (see fig. 4)

h_{k_1}, h_{k_2} coordinates defined by equations (A23)

h_{sr} component of distance from reference point to center of mass of balloon structure, positive for center of mass below reference point, m (see fig. 4)

I_x, I_y, I_z rolling, pitching, and yawing moments of inertia, respectively, about balloon center of mass in the stability axis system (including aerodynamic apparent inertias), kg-m^2

I_{xx}, I_{yy}, I_{zz} rolling, pitching, and yawing moments of inertia, respectively, about balloon center of mass in the body-reference principal axis system (including aerodynamic apparent inertias), kg-m^2

I_{xy}, I_{xz}, I_{yz} products of inertia about balloon center of mass in the XY-plane, XZ-plane, and YZ-plane, respectively (including aerodynamic apparent inertias), kg-m^2

k_{xx} tether x-force per unit of x-displacement at bridle confluence point, N/m (see eq. (B21a))

k_{xz} tether x-force per unit of z-displacement, N/m (see eq. (B21b))

$k_{x\theta}$ tether x-force per unit of pitch displacement, N/rad (see eq. (A27a))

k_{yy} tether y-force per unit of y-displacement at bridle confluence point, N/m (see eq. (B24))

$k_{y\phi}$ tether y-force per unit of roll displacement, N/rad (see eq. (A27h))

$k_{y\psi}$ tether y-force per unit of yaw displacement, N/rad (see eq. (A27i))

k_{zx} tether z-force per unit of x-displacement, N/m (see eq. (B21c))

k_{zz} tether z-force per unit of z-displacement at bridle confluence point, N/m (see eq. (B21d))

$k_{z\theta}$ tether z-force per unit of pitch displacement, N/rad (see eq. (A27b))

$k_{\theta x}$ tether pitching moment per unit of x-displacement, N-m/m (see eq. (A27c))

$k_{\theta z}$ tether pitching moment per unit of z-displacement, N-m/m (see eq. (A27d))

$k_{\theta\theta}$ total tether pitching moment per unit of pitch displacement in the body-axis system for pitch about center of mass, N-m/rad (see eq. (A27e))

$k_{\theta\theta_D}$ portion of $k_{\theta\theta}$ due to rotation of balloon relative to steady tension vector at bridle confluence point, N-m/rad (see eq. (A27f))

$k_{\theta\theta_T}$ portion of $k_{\theta\theta}$ due to displacement of bridle confluence point, N-m/rad (see eq. (A27g))

$k_{\phi y}$ tether rolling moment per unit of y-displacement, N-m/m (see eq. (A27j))

$k_{\phi\phi}$ tether rolling moment per unit of roll displacement in the body-axis system for roll about center of mass, N-m/rad (see eq. (A27k))

$k_{\phi\psi}$ tether rolling moment per unit of yaw displacement, N-m/rad (see eq. (A27l))

$k_{\psi y}$ tether yawing moment per unit of y-displacement, N-m/m (see eq. (A27m))

$k_{\psi\phi}$ tether yawing moment per unit of roll displacement, N-m/rad (see eq. (A27n))

$k_{\psi\psi}$ tether yawing moment per unit of yaw displacement in the body-axis system for yaw about center of mass, N-m/rad (see eq. (A27o))

L aerodynamic lift force, N

l tether cable length, m

l_{br} component of distance from reference point to center of buoyancy, positive for center of buoyancy forward of reference point, m (see fig. 4)

l_{cg} component of distance from reference point to center of mass, positive for center of mass forward of reference point, m (see fig. 4)

l_{sr} component of distance from reference point to center of mass of balloon structure, positive for center of mass aft of reference point, m (see fig. 4)

l_{tr} component of distance from reference point to bridle confluence point, positive for confluence point forward of reference point, m (see fig. 4)

M_{s_1}, M_{s_2} moments defined by equations (A31)

M_X, M_Y, M_Z rolling, pitching, and yawing moments about X-, Y-, and Z-axes, respectively, N-m (see fig. 2)

m mass of balloon, kg

m_a apparent mass of air associated with accelerations of balloon, kg

$m_{a_1}, m_{a_2}, m_{a_3}$ apparent masses associated with accelerations in x-, y-, and z-directions, respectively, kg (see eqs. (A10) and (A11))

m_g mass of inflation gas, kg

m_s balloon structural mass (including bridle, test instruments, and payload), kg

m_T combined mass of balloon structure and inflation gas, $m_g + m_s$, kg

m_x, m_y, m_z masses defined by equations (A32)

$m_{x,a}, m_{y,a}, m_{z,a}$ aerodynamic apparent masses associated with balloon acceleration along X''-, Y''-, and Z''-axes, respectively, kg (see fig. 1 for axis system)

$m_{x,o}, m_{y,o}, m_{z,o}$ total masses of balloon for accelerations in x-, y-, and z-directions, respectively, kg (see eqs. (A10))

n cable drag per unit length for cable normal to the wind, N/m

P,Q,R total rolling, pitching, and yawing rates about X-, Y-, and Z-axes, respectively, rad/sec (see fig. 2)

P_n cable drag force defined by equation (B1)

p,q,r perturbation rolling, pitching, and yawing rates about X-, Y-, and Z-axes, respectively, rad/sec

$\bar{p} = \frac{w_c}{2n}$

$\bar{q} = \sqrt{1 + \bar{p}^2}$

S characteristic area of balloon, $V_b^{2/3}$, m^2

T tether-cable tension, N

T_0, T_1 tensions of tether cable at lower and upper ends, respectively, N (see fig. 1)

t time, sec

t_{tr} component of distance from reference point to bridle confluence point, positive for confluence point below reference point, m (see fig. 4)

U,V,W velocities of balloon center of mass along X-, Y-, and Z-axes, respectively, m/sec (see fig. 2)

u,v,w perturbation velocities of balloon center of mass along X-, Y-, and Z-axes, respectively, m/sec

V_∞ steady wind velocity, m/sec

V_b volume of balloon hull (i.e., gas bag), m^3

V_n component of wind velocity normal to cable, $V_\infty \sin \gamma$, m/sec

v^* y-perturbation velocity of balloon with respect to airstream, $v - V_\infty \psi$, m/sec

W_s structural weight of balloon (including bridle, payload, and test instruments), N

w^* z-perturbation velocity of balloon with respect to airstream, $w + V_\infty \theta$, m/sec

w_c tether-cable weight per unit length, N/m

x,y,z perturbation displacements in the stability axis system, m (see fig. 1 for axis system)

x',y',z' perturbation displacements in the earth-fixed axis system, m (see fig. 1 for axis system)

x'',y'',z'' perturbation displacements in the balloon-fixed axis system, m (see fig. 1 for axis system)

x'_c,y'_c,z'_c perturbation displacements of upper end of tether cable (e.g., bridle confluence point) in the earth-fixed axis system, m

x_t distance parallel to X-axis from reference point to center of mass, positive for center of mass forward of reference point, m (see appendix C)

x_1,z_1 coordinates of balloon center of mass with respect to tether-cable anchor point; x_1 is horizontal and positive in downstream direction, z_1 is vertical and positive upwards, m (see fig. 1 for tether anchor point)

z_t distance parallel to Z-axis from reference point to center of mass, positive for center of mass below reference point, m (see appendix C)

α perturbation angle of attack of X-axis, $\frac{\dot{z}'}{V_\infty} + \theta$, rad

α_t balloon angle of attack at trim, rad

β angle of sideslip, $\frac{\dot{y}'}{V_\infty} - \psi$, rad

γ	tether-cable angle with respect to the horizontal (see appendix B), rad
γ_0,γ_1	angles between the horizontal and tether cable at lower and upper ends, respectively, rad (see fig. 1)
δ	displacement defined by equation (B22)
ϵ	angle between principal X-axis of balloon and stability X-axis, rad
η	real part of characteristic root of stability equations, damping parameter, 1/sec
Θ,Φ,Ψ	Euler angles of pitch, roll, and yaw, respectively, rad (see fig. 3)
θ,ϕ,ψ	perturbations of Θ, Φ, and Ψ, respectively, rad
λ	characteristic root of stability equations, $\eta \pm i\omega$, 1/sec
$\bar{\lambda}$	variable defined by equation (B12)
$\bar{\lambda}_0,\bar{\lambda}_1$	$\bar{\lambda}$ at lower and upper ends, respectively, of tether cable
ρ	atmospheric density, kg/m^3
τ	variable defined by equation (B9b)
τ_0,τ_1	τ at lower and upper ends, respectively, of tether cable
ω	imaginary part of characteristic root of stability equations, circular frequency, rad/sec

Subscripts:

A	aerodynamic force term
B	buoyancy force term
C	tether-cable force term
G	gravity force term

R reference point (see fig. 4)

t equilibrium trim condition

0 lower end of tether cable

1 upper end of tether cable

Subscripts used with the aerodynamic coefficients denote derivatives as follows:

α with respect to α

$\dot{\alpha}$ with respect to $\dot{\alpha}\bar{c}/2V_\infty$

β with respect to β

$\dot{\beta}$ with respect to $\dot{\beta}\bar{c}/2V_\infty$

p with respect to $p\bar{c}/2V_\infty$

q with respect to $q\bar{c}/2V_\infty$

r with respect to $r\bar{c}/2V_\infty$

u with respect to u/V_∞

Dots over a symbol indicate derivatives with respect to time.

ANALYSIS

General Comments and Assumptions

The stability analysis presented is for a balloon tethered from an earth-fixed anchor point and flying in a steady wind. The balloon's motions consist of small perturbations about a steady-flight reference condition.

The analysis is essentially a linearized, stability-derivative type of analysis similar to that for a conventional airplane (ref. 9). In contrast with conventional-airplane analyses, however, the equations of motion for the tethered balloon include buoyancy forces, apparent mass terms, and static forces resulting from the tether cable.

The coordinate systems, forces, and moments used in deriving the equations of motion for the tethered balloon are shown in figures 1 to 4. The three different sets of right-hand Cartesian coordinates used in this analysis are as follows:

(1) The stability axis system (X-, Y-, and Z-axes) is a balloon-fixed coordinate system with its origin located at the balloon center of mass. When the balloon is in the reference steady-state condition, the X-axis points into the direction of the wind and the Z-axis points downward. The XZ-plane is the plane of symmetry.

(2) The X'-, Y'-, and Z'-axes are an earth-fixed coordinate system. When the balloon is in a reference steady-state condition, the origin of the coordinate system is located at the balloon center of mass. The Z'-axis points vertically downward, the Y'-axis points normal to the wind, and the X'-axis points forward.

(3) X''-, Y''-, and Z''-axes are a balloon-fixed coordinate system with its origin located at the balloon center of mass. The X''-axis is parallel to the axis of symmetry of the balloon and is positive toward the nose. The X''- and Z''-axes are in the plane of symmetry, and the Y''-axis points toward the right side of the balloon.

The mathematical model used in the analysis includes the following considerations and assumptions:

(1) The equations of motion are referenced to the center of mass of the balloon. The balloon mass includes the mass of the balloon structure (including bridle and payload), the buoyant gas inside the balloon, and the apparent air mass; hence, the balloon center of mass is at a different location than the structural center of mass (see fig. 4). The apparent air mass is defined as the mass of air surrounding the balloon which moves with the balloon when it is accelerated.

(2) There are four kinds of external forces acting on the balloon, namely, aerodynamic forces, tether-cable forces, buoyancy forces, and gravity forces (fig. 1).

(3) The balloon is symmetric laterally and has yaw, roll, and sideslip angles equal to zero in the reference steady-state trimmed condition $\left(\text{i.e.,}\ \Psi_t = \Phi_t = \beta_t = 0\right)$.

(4) The steady wind velocity V_∞ is parallel to the horizon. Thus for steady-state equilibrium conditions, the pitch angle of the X-axis is zero $\left(\text{i.e.,}\ \Theta_t = 0\right)$ and the stability and earth-fixed axes systems are coincident.

(5) The balloon and bridle form a rigid system.

(6) The tether cable is flexible, but inextensible, has negligible mass compared to that of the balloon, and contributes only static forces at the bridle confluence point.

(7) The cable weight and drag normal to the cable are needed only for determining the static cable forces, equilibrium shape of the cable, and the cable derivatives.

(8) The longitudinal and lateral equations of motion are uncoupled.

The preceding assumptions simplify the stability analysis, but they also restrict the analysis to balloons with light tether cables. One difficulty is that the tether cable effectively increases the mass of the balloon system by approximately one-third the mass of the cable (ref. 10). Consequently, if the effective cable mass is considered to be concentrated at the bridle confluence point, then its contribution to the balloon's mass properties can be appreciable. The mass of the tether cable can also cause coupling of the cable and balloon motions, but this effect is neglected in the present study. Because of these difficulties, it is believed that the present analysis should be restricted to cases where the cable mass is small compared to that of the balloon mass (including the apparent mass). Data which are presented later, however, indicate that the present analysis gives good correlation with experimental results for tether-cable masses as large as 16 percent of the balloon mass.

Although the present analysis is somewhat restrictive, it can be used for a large class of tethered-balloon systems. Furthermore, the analysis yields a system of second-order ordinary differential equations which can be solved by methods used in conventional-aircraft stability analyses. Recent analyses (refs. 11 and 12) have been developed which include the mass and dynamics of the tether cable, but these analyses involve rather complex methods of solution.

The equations of motion for the mathematical model used in the analysis are derived in appendices A and B. Note that the mass and inertia terms in these equations (see eq. (A10)) include the apparent mass of air associated with the balloon accelerations. In contrast with conventional-airplane analysis, the balloon analysis must include the apparent mass because it accounts for greater than 60 percent of the total mass for some balloon systems.

Although the equations of motion shown in appendix A are derived for a balloon tethered in a steady wind to an earth-fixed anchor point, the equations are also valid for a balloon towed at a constant velocity over a horizontal surface.

Equilibrium Trim Conditions

The steady-state trimmed conditions are obtained from equations (A30a), (A30c), and (A30e) of appendix A by setting the perturbation quantities equal to zero. The results are:

$$\frac{\rho V_\infty{}^2 S}{2} C_D - T_1 \cos \gamma_1 = 0 \tag{1}$$

$$\frac{\rho V_\infty{}^2 S}{2} C_L + B - W_S - T_1 \sin \gamma_1 = 0 \tag{2}$$

$$-\frac{\rho V_\infty{}^2 S\bar{c}}{2} C_m + h_{k_1} T_1 \sin\gamma_1 - h_{k_2} T_1 \cos\gamma_1 - M_{s_2} = 0 \tag{3}$$

Substituting equations (1) and (2) into equation (3) to eliminate the cable tension T_1 and angle γ_1 gives the following trim equation:

$$h_{k_1}\left(\frac{\rho V_\infty{}^2 S}{2} C_L + B - W_s\right) - h_{k_2}\left(\frac{\rho V_\infty{}^2 S}{2} C_D\right) - \frac{\rho V_\infty{}^2 S\bar{c}}{2} C_m - M_{s_2} = 0 \tag{4}$$

where from equations (A23) and (A31b)

$$h_{k_1} = (l_{tr} - l_{cg})\cos\alpha_t + (t_{tr} - h_{cg})\sin\alpha_t$$

$$h_{k_2} = (t_{tr} - h_{cg})\cos\alpha_t - (l_{tr} - l_{cg})\sin\alpha_t$$

$$M_{s_2} = \left[(l_{br} - l_{cg})B + (l_{sr} + l_{cg})W_s\right]\cos\alpha_t - \left[(h_{cg} - h_{br})B + (h_{sr} - h_{cg})W_s\right]\sin\alpha_t$$

Equation (4) can be solved by Newton iteration to find the equilibrium trim angle of attack α_t for various wind velocities, provided the aerodynamic coefficients C_L, C_D, and C_m are known functions of α_t. Once the trim angle of attack is determined, then equations (1) to (3) can be solved to find T_1 and γ_1. The α-dependent stability coefficients can also be evaluated.

Stability Equations

The stability equations are obtained by setting the equilibrium trim portions of the equations of motion (eqs. (A30a) to (A30f)) equal to zero. The remaining expressions give six linear stability perturbation equations, three of which involve only longitudinal variables and three of which involve only lateral variables. For convenience, the primes on the x', y', and z' variables are dropped. Thus, the following working forms of the stability equations written about the balloon center of mass are obtained.

Longitudinal equations of motion.- The equations of longitudinal motion may be written as follows:

x-force

$$\ddot{x} + \frac{\rho V_\infty S}{2m_x}(2C_D + C_{D_u})\dot{x} + \frac{k_{xx}}{m_x} x + \frac{\rho V_\infty S}{2m_x}(C_{D_\alpha} - C_L)\dot{z} + \frac{k_{xz}}{m_x} z + \left(\frac{k_{x\theta}}{m_x} + \frac{\rho V_\infty{}^2 S C_{D_\alpha}}{2m_x}\right)\theta = 0 \tag{5a}$$

z-force

$$\frac{\rho V_\infty S}{2m_z}\left(2C_L + C_{L_u}\right)\dot{x} + \frac{k_{zx}}{m_z}x + \ddot{z} + \frac{\rho V_\infty S}{2m_z}\left(C_{L_\alpha} + C_D\right)\dot{z} + \frac{k_{zz}}{m_z}z$$

$$+ \frac{\rho V_\infty S\bar{c}}{4m_z}\left(C_{L_{\dot{\alpha}}} + C_{L_q}\right)\dot{\theta} + \left(\frac{k_{z\theta}}{m_z} + \frac{\rho V_\infty{}^2 S C_{L_\alpha}}{2m_z}\right)\theta = 0 \tag{5b}$$

Pitching moment

$$-\frac{\rho V_\infty S\bar{c}}{2I_y}\left(2C_m + C_{m_u}\right)\dot{x} + \frac{k_{\theta x}}{I_y}x - \frac{\rho S\bar{c}^2}{4I_y}C_{m_{\dot{\alpha}}}\ddot{z} - \frac{\rho V_\infty S\bar{c}}{2I_y}C_{m_\alpha}\dot{z} + \frac{k_{\theta z}}{I_y}z + \ddot{\theta}$$

$$-\frac{\rho V_\infty S\bar{c}^2}{4I_y}\left(C_{m_{\dot{\alpha}}} + C_{m_q}\right)\dot{\theta} + \left(\frac{M_{s_1}}{I_y} - \frac{\rho V_\infty{}^2 S\bar{c}}{2I_y}C_{m_\alpha} + \frac{k_{\theta\theta}}{I_y}\right)\theta = 0 \tag{5c}$$

Lateral equations of motion.- The equations of lateral motion may be written as follows:

y-force

$$\ddot{y} - \frac{\rho V_\infty S}{2m_y}C_{Y_\beta}\dot{y} + \frac{k_{yy}}{m_y}y - \frac{\rho V_\infty S\bar{c}}{4m_y}C_{Y_p}\dot{\phi} + \left(\frac{k_{y\phi}}{m_y} - \frac{\rho V_\infty{}^2 S C_L}{2m_y}\right)\phi$$

$$+ \frac{\rho V_\infty S\bar{c}}{4m_y}\left(C_{Y_{\dot{\beta}}} - C_{Y_r}\right)\dot{\psi} + \left[\frac{\rho V_\infty{}^2 S\left(C_{Y_\beta} + C_D\right)}{2m_y} + \frac{k_{y\psi}}{m_y}\right]\psi = 0 \tag{6a}$$

Rolling moment

$$-\frac{\rho S\bar{c}^2}{4I_x}C_{l_{\dot{\beta}}}\dot{y} - \frac{\rho V_\infty S\bar{c}}{2I_x}C_{l_\beta}\dot{y} + \frac{k_{\phi y}}{I_x}y + \ddot{\phi} - \frac{\rho V_\infty S\bar{c}^2}{4I_x}C_{l_p}\dot{\phi}$$

$$+ \frac{k_{\phi\phi} + h_{k_2}T_1 \sin\gamma_1 + M_{s_1}}{I_x}\phi - \frac{I_{xz}}{I_x}\ddot{\psi}$$

$$+ \frac{\rho V_\infty S\bar{c}^2}{4I_x}\left(C_{l_{\dot{\beta}}} - C_{l_r}\right)\dot{\psi} + \left[\frac{k_{\phi\psi}}{I_x} + \frac{\rho V_\infty{}^2 S\left(\bar{c}C_{l_\beta} - h_{k_2}C_D\right)}{2I_x}\right]\psi = 0 \tag{6b}$$

Yawing moment

$$-\frac{\rho S\bar{c}^2}{4I_Z} C_{n_{\dot{\beta}}} \ddot{y} - \frac{\rho V_\infty S\bar{c}}{2I_Z} C_{n_\beta} \dot{y} + \frac{k_{\psi y}}{I_Z} y - \frac{I_{xz}}{I_Z} \ddot{\phi} - \frac{\rho V_\infty S\bar{c}^2}{4I_Z} C_{n_p} \dot{\phi}$$

$$+ \frac{k_{\psi\phi} + M_{s_2} - h_{k_1} T_1 \sin \gamma_1}{I_Z} \phi + \ddot{\psi} + \frac{\rho V_\infty S\bar{c}^2}{4I_Z} \left(C_{n_{\dot{\beta}}} - C_{n_r}\right) \dot{\psi}$$

$$+ \left[\frac{k_{\psi\psi}}{I_Z} + \frac{\rho V_\infty^2 S\left(\bar{c} C_{n_\beta} + h_{k_1} C_D\right)}{2I_Z}\right] \psi = 0 \tag{6c}$$

Although the stability equations and equilibrium trim equations are written about the balloon center of mass, the aerodynamic forces and moments may be referenced to an arbitrary point (see the reference point in fig. 4) which is generally not located at the center of mass. In such cases it is necessary to transfer the aerodynamic terms to the balloon center of mass through the use of the transfer equations given in appendix C.

The aerodynamic forces are treated in this manner in the present study because it is more convenient to use aerodynamic inputs to the computer programs (ref. 7) which are referenced to a fixed point in the balloon rather than to a variable center of mass. The location of the balloon center of mass varies with changes in altitude because the mass of the buoyancy gas and apparent mass are both functions of atmospheric density. The location of the center of mass also changes as the payload position and weight are varied.

Balloon Stability Characteristics

The longitudinal and lateral stability characteristics of the balloon are determined independently from equations (5) and (6), respectively, in a manner similar to that used in conventional-airplane stability analysis (ref. 9). Since the stability equations are ordinary linear differential equations with constant coefficients, they have transient solutions which are always exponential in form. For example, a typical variable such as θ is of the form $\theta = \bar{\theta} e^{\lambda t}$, where $\bar{\theta}$ is a complex constant. If these exponential forms are substituted into the longitudinal and lateral stability equations and the determinants of the coefficients are set equal to zero, solutions for the characteristic roots λ can be obtained.

Solving equations (5) and (6) in this manner gives six characteristic roots for each of the longitudinal and lateral cases. These roots appear as complex conjugate pairs (i.e., $\lambda = \eta \pm i\omega$) for oscillatory modes of motion or as real numbers (i.e., $\lambda = \eta$) for the aperiodic modes. Thus, in each of the longitudinal and lateral cases, it is possible

for the balloon to exhibit from three to six modes of motion, depending on whether the roots are real or complex conjugate pairs. For any mode, the balloon system is stable when $\eta < 0$, neutrally stable when $\eta = 0$, and unstable when $\eta > 0$.

Computer programs based on equations (5) and (6) were developed for calculating the stability characteristics and plotting the results. These programs are described in detail in reference 7. Some typical results from these programs are given in the section entitled "Results and Discussion."

TOW TESTS

In order to provide experimental data for comparison with analytical results, a balloon was towed from a truck. Some instabilities were measured and some frequencies and dampings were obtained for the stable cases.

Description of the Balloon and Tow-Test Apparatus

Balloon.- The balloon used for the tow tests is shown attached to the tow truck in figure 5. The balloon is 7.64 m long and has a basic shape similar to the Navy C-class airship configuration (ref. 13), except that the aft section is conical and the nose is nearly spherical. The essential components of the balloon consist of an inflatable hull and a rigid (i.e., not inflated) tail-fin assembly. A load band is attached to the lower portion of the hull which permits variations in the bridle attachment points and, hence, makes it possible to change the balloon equilibrium trim angle of attack. A more detailed description of the balloon is given in reference 6.

The aerostatic, mass, inertia and aerodynamic properties of the balloon for the reference configuration are given in table I. The reference configuration used in the present study was arbitrarily chosen such that the balloon would fly stably at small trim angles of attack for a large range of tow velocities. The balloon properties shown in table I were determined by procedures described in reference 6.

Test equipment and procedures.- The panel truck used in the tests (fig. 5) provided space for data recording equipment and acted as a towing vehicle. The test instrumentation on the truck included a load cell to measure cable tension, potentiometers to measure cable inclination angles, and an anemometer (i.e., wind sensor) to measure speed and sideslip angle. Instruments were also suspended rigidly beneath the balloon to measure pitch and roll motions. Outputs from the instruments were recorded on strip charts during the tests. Motions of the balloon were also recorded by a camera mounted on the truck.

There were several features of the test equipment and procedures which limited the range of the tow tests. The primary limitation was that 61 m was as long a tether cable

as was practical or convenient to use. The maximum speed of the tow truck with the balloon attached was 29 m/sec.

Test Description and Data Reduction

A list of the tow tests and test variables is given in table II. The test variables are tow velocity V_∞, bridle-confluence-point location l_{tr}, and tether-cable length l, weight w_c, and diameter d_c. The balloon trim angle of attack α_t depends upon the tow velocity and bridle-confluence-point location. The range over which these properties are varied is indicated in table II.

Each test result shown in table II represents the average of several runs at essentially the same relative airspeed. These runs were made during periods of calm air when the ambient wind velocity was less than 2.5 m/sec.

During tests 10 to 14, the balloon was initially displaced with an auxiliary line from its equilibrium trim angle and released when the tow vehicle was at the proper speed. This was done in order to produce disturbances from which the frequency and damping of the balloon motion could be determined. The oscillations observed in tests 15 to 18 were self-excited unstable motions requiring no initial displacements.

The pitch angle, roll angle, velocity V_∞, and tether-cable data were recorded on the strip charts. The x-, y-, and ψ-displacements of the balloon were obtained from the movie film. No attempt was made to measure the z-displacements.

RESULTS AND DISCUSSION

Since the longitudinal and lateral equations of motion are uncoupled, the longitudinal and lateral results are presented separately. In each case, the results for the 7.64-m balloon in the reference configuration (i.e., the configuration for tests 12 and 15 of table II) are presented first. These results are followed by data for the balloon in the other test configurations (i.e., the configurations for tests 10, 11, 13, 14, 16, 17, and 18). A parameter trend study is also presented for both the longitudinal and lateral cases.

Where possible, the results from the analysis are compared with experimental data from the tow tests. The quantities compared are the oscillatory frequencies, damping rates, modes of motion, and stability boundaries for the 7.64-m balloon.

Longitudinal Stability Characteristics

Reference configuration.- The calculated values of the longitudinal frequencies ω and damping rates η for the balloon in the reference configuration are plotted as a function of wind velocity in figure 6(a). These same values of ω and η are given in root-locus form with velocity as the varying parameter in figure 6(b). These figures indicate that the reference configuration has three oscillatory modes of motion at velocities less

than 13.5 m/sec. For velocities greater than this value, mode 1 splits into two real nonoscillatory modes. The figures also show that the calculated value for mode 2 becomes unstable (i.e., $\eta \geq 0$) at 22.4 m/sec.

The measured results from the tow tests of the balloon in the reference configuration (i.e., tests 12 and 15 of table II) are shown in figure 6(a). In comparing these results with the calculated data, it appears that the measured frequencies and damping rates correspond to those calculated for mode 2, except at a velocity of 12.5 m/sec. At this velocity, two different frequencies were observed – one corresponding to mode 2 and the other to mode 3 – but the data were insufficient to determine the damping rates for either mode.

The measured data show the balloon to be unstable at velocities greater than 24 m/sec, which is in good agreement with the calculated results. The instabilities observed at these velocities were quite violent. In several cases the motions become so excessive that either the tether cable or load band broke and the balloon was severely damaged.

As a means of illustrating the longitudinal modes of motion, the tethered balloon and its center of mass are shown for a sequence of time intervals in figures 7(a), (b), and (c). The plots in these figures are drawn from the calculated data by means of a computer program given in reference 7. Except for the middle and lower portions of figure 7(a), the time sequence shown for each velocity and value of λ represents one cyle of free oscillation for a single mode. The time sequences for the plots in the middle and lower portions of figure 7(a) are just long enough to allow the nonoscillatory balloon motions to reach steady-state equilibrium conditions.

Each mode of motion shown in figure 7 was obtained by substituting the value of the characteristic root λ of the mode into equation (5) and solving for the ratios of the displacements to the pitch angle. The initial pitch-angle amplitude was an input to the computer program (ref. 7) and its value could be arbitrarily selected. Thus the initial amplitude of the balloon's displacements could be adjusted as desired.

The modes of motion shown in figure 7 do not represent transient response in the usual sense. During transient motions, all of the modes of a dynamic system generally participate in the motion simultaneously, the relative degree of participation depending on the initial conditions or excitation. The purpose of figure 7 is simply to illustrate the character of each mode individually. When one of the modes becomes lightly damped or unstable, however, it may dominate the transient motions. Such was the case in the runs of test 15 for velocities greater than about 20 m/sec. At these velocities the observed transient motions of the balloon were very similar to those shown for mode 2 in the lower portion of figure 7(b).

The effect of damping on a given mode, at a particular velocity, can be observed in figure 7 by comparing the balloon displacements at the beginning and end of each time

sequence. For example, in figure 7(b) it can be seen that the balloon motion is highly damped (i.e., $\eta < 0$) at a velocity of 10 m/sec since the displacement is almost zero at the end of the time sequence. At $V_\infty = 30$ m/sec, it is observed that the balloon is unstable (i.e., $\eta > 0$) since the displacement at the end of the sequence is larger than that at the beginning of the cycle.

It was mentioned previously that mode 1 splits into two nonoscillatory modes (i.e., modes 1a and 1b) at velocities above 13 m/sec. Figure 7(a) shows that mode 1a is predominantly translational motion while mode 1b is predominantly rotational motion. Figure 7(c) indicates graphically the result presented in figure 6(a), that is, the balloon motions for mode 3 become more damped as velocity increases.

A computer generated motion-picture supplement (L-1118) has been made which shows the balloon modes of motion in more detail for both the longitudinal and lateral cases. This film is available on loan and a request card is included at the back of this report.

Additional configurations.- Results for the configurations corresponding to tests 10, 11, 13, 14, 16, 17, and 18 of table II are presented in figures 8 to 13. These figures show that the calculated values of ω and η are in fair agreement with the measured values at the test velocities indicated. Note that in some of the figures there are fewer measured values of η presented than of ω. For those cases where η is omitted, the measured data were inadequate to determine the damping of the balloon motions.

The primary purpose of tests 10 to 14 was to check the accuracy of the frequencies and damping rates calculated from the analysis. An additional objective was to determine experimentally the effects of the tether-cable length, diameter, and weight on the modes of motion. Neither of these test objectives required the use of high tow velocities; thus, tests 10 to 14 were conducted at velocities well below the predicted velocities of instability (see figs. 6 and 8 to 11).

By comparing the data from tests 10, 11, and 12 (figs. 8, 9, and 6 and table II) it can be seen that changes in the tether-cable length have large effects on all three modes of motion. These data show that the velocity at which mode 1 becomes nonoscillatory decreases as the tether length increases. The velocity at which mode 2 becomes unstable also decreases as the tether length increases. (The trend study for the present balloon configuration, which is presented later, indicates that the velocity of instability increases as the tether length increases for lengths longer than 90 m.) At a given velocity, the frequencies of all the modes decrease as the tether length increases, but mode 3 shows the greatest change in frequency.

The effects of changes in the tether-cable weight and diameter on the longitudinal modes of motion can be determined by comparing the data for tests 11, 13, and 14 (figs. 9 to 11 and table II). These data show that the velocity at which mode 2 becomes unstable

decreases as the cable weight and diameter increase. Based on the trend study, which is presented later, the modes of motion are affected more by changes in the tether-cable diameter than by changes in cable weight. It should be noted that the tether cable for tests 14 and 18 (fig. 11) was the heaviest cable used in the tow tests. The mass of this cable was about 16 percent of the balloon mass (including apparent mass).

The data presented in figures 11 to 13 (and also fig. 6) indicate that the stability analysis does predict the damping and frequencies near the point of instability (i.e., near $\eta = 0$) quite well. Note that in figures 11 and 13 the slopes of the damping curve are almost flat near $\eta = 0$. For these two cases a slight error in η makes a large difference in the velocity at which the balloon goes unstable. This result is particularly true for figure 13. For this case the calculated and measured damping values seem to correspond quite well. The calculations, however, indicate that the motions are very lightly damped and may never go unstable, whereas the measured results show that the motions become slightly unstable for velocities greater than about 23 m/sec. It is possible for this case that the measured damping may be slightly in error since it was difficult to determine from the recorded motions whether the balloon was very lightly damped, neutrally damped, or slightly unstable. There is some evidence to indicate that the motions may have been very lightly damped since the cable loads during the test did not become excessive and the motions were quite mild compared to those in test 15.

The calculations shown in figure 12 are for the case where the balloon is tethered at a high angle of attack (see table II). For this case the balloon is unstable at low wind velocities. This unstable condition is consistent with the results of reference 11 and is primarily due to interactions between the balloon's lift and drag forces. For this condition the lift acts as a forcing function and the drag acts as a damping function, and thus a high lift-drag ratio aggravates the balloon's motions (ref. 11). The two experimental points shown in figure 12 indicate that the balloon was not quite unstable as analytically predicted, but was very lightly damped. The motions were quite large, however, and may have been either lightly damped or limit-cycle oscillations which are considered unstable motions. The analysis predicted that the balloon would be more stable at higher velocities because, for this case, the angle of attack decreases with increasing velocity. Nevertheless, because the balloon was experiencing quite large motions at such low velocities and visual observations gave evidence that this configuration may be unstable, no test velocities higher than those shown were attempted.

Longitudinal trend study.- Analytical trend studies for the 7.64-m balloon in the reference configuration are presented in figures 14 to 27. These figures show how changes in individual stability parameters affect the frequency and velocity of instability. The properties of the test balloon in the reference configuration are indicated in each of the figures.

The parameters considered in the longitudinal-stability trend study, and a list of the corresponding figures in which these parameters appear, are given in table III. A preliminary investigation indicated that only those parameters shown have a major effect on the longitudinal stability of the balloon in the reference configuration. Notice that several of the aerodynamic parameter symbols shown in the table have the prefix Δ. This prefix indicates an incremental difference between two values of the same parameter, where one of the values is for the balloon in the reference configuration (e.g., $\Delta C_D = C_D - C_{D_{reference}}$).

The effects of the balloon mass and inertia properties on the stability boundaries are shown in figures 14 to 17. These figures indicate that a reduction in the balloon mass m_T and pitch inertia should raise the instability speed. They also show an increase in stability speed (fig. 16) with the center of mass located lower and farther forward on the hull. Further, figure 17 indicates that reducing $m_{x,a}$ and increasing $m_{z,a}$ would increase stability.

The effects of buoyancy are shown in figure 18. This figure indicates that for better stability the buoyancy force should be larger and located farther forward in the hull, but not so far forward as to get into low speed instabilities.

The effect of the tether-cable length on the stability boundary has been discussed previously in relation to figures 6, 8, and 9, and additional information is presented in figure 19(a). A plot showing the equilibrium position of the balloon as a function of tether length and wind velocity is given in figure 19(b). Note that in figure 19(a) the measured points of instability for test 15 are compared with the calculated data. Because of the previously mentioned limitations in the test equipment, points of instability were measured only for the 61-m tether length. A number of tow tests were conducted using tether cables of shorter lengths; but because the maximum speed of the tow truck was 29 m/sec, no additional longitudinal instabilities were observed for the balloon using the same bridle arrangement and cable diameter as the reference configuration.

Figure 20 shows that the location of the tether-cable attachment point (i.e., bridle confluence point) has a large effect on the stability boundary and balloon trim angle of attack. The analytical results in this figure show that the instability speed increases as the attachment point is moved forward. In contrast with the analytical results, the measured data for tests 15 and 17 indicate that the instability speed may decrease slightly with increasing l_{tr}. As discussed earlier, however, the measured instabilities shown for test 17 may be somewhat questionable since it is possible that the balloon motions may have been very lightly damped for the velocities shown. Note that in figure 20(b) the trim angle decreases with increasing velocity for small values of l_{tr}, but the opposite is true for large values of l_{tr}. Thus, ideally, there is a value for l_{tr} for which the trim angle is independent of wind speed.

The effects of tether-cable diameter and weight per unit length are shown in figures 21 and 22. The cable diameter affects the cable drag which, in turn, has a large effect on the stability boundaries, as shown in figure 21. A comparison of figures 21 and 22 indicates that the cable diameter has a much greater effect on the stability boundaries than the cable weight. These figures also show that the tether cable should be small in diameter and light in weight.

Plots showing the variation of the balloon's position with changes in wind velocity for several different cable diameters are shown in figures 21(b) and (c). These plots indicate that for velocities greater than 35 m/sec, the position of the balloon does not change appreciably as the wind velocity increases for the cable diameters shown. On the other hand, the balloon position does change considerably for high wind velocities as the cable diameter changes.

The results shown in figure 23 indicate that the longitudinal stability boundary is sensitive to variations in the tether-cable derivatives. Thus, these derivatives must be calculated accurately. Note from appendix B that these derivatives are not independent parameters, but are functions of the wind speed, balloon aerodynamics, buoyancy forces, and tether-cable properties. Thus, since these derivatives are not independent parameters, the absolute values of the derivatives are not shown. A more meaningful interpretation of the sensitivity of these derivatives is obtained by plotting them in terms of a fractional variation from their normal values for the balloon in the reference condition. The normal reference values of the tether-cable derivatives change, of course, as the wind speed changes.

The effects of the aerodynamic terms on the longitudinal stability boundaries are shown in figures 24 to 27. Since the reference values of the first four terms are functions of the wind speed (see table I), the absolute values of these terms are not shown, but incremental changes with respect to their reference values are plotted. The fifth term C_{m_α} is also presented in terms of incremental changes. Figure 24 indicates that positive increments of static aerodynamic drag and pitching moments about the center of mass are stabilizing. A reduction in lift should also be stabilizing. Although a large increase in lift appears to be stabilizing, a large lift coefficient may cause structural problems at high speeds. Reduction in the values of C_{L_α} and C_{m_α} (fig. 25) leads to an increase in the speed of instability. The derivative $C_{m_{\dot{\alpha},R}}$ (fig. 26) should be less negative and $C_{m_{q,R}}$ (fig. 27) should be more negative for increased stability. Note that these latter two pitching-moment derivatives are given about the reference point (fig. 4) instead of about the center of mass.

The preceding aerodynamic data indicate that for better stability the balloon's horizontal tail fin should be located farther aft of the center of mass. This configuration will give a more stable combination of values for C_{L_α}, C_{m_α}, $C_{m_{\dot{\alpha}}}$, and C_{m_q}. The hori-

zontal fin should also have a small negative angle of attack with respect to the body center line in order to decrease lift and give a more positive pitching moment.

Lateral Stability Characteristics

Reference configuration.- The calculated values of the lateral frequencies ω and damping rates η for the balloon in the reference configuration are plotted as a function of wind velocity in figure 28(a), and in root locus form in figure 28(b). The data in these figures indicate that none of the modes for this configuration are unstable, but mode 2 is very lightly damped. This result agrees with the tow-test data shown in figure 28(a). Note that mode 1 splits into two nonoscillatory modes of motion at a velocity of 2 m/sec and that mode 3 has a rather high oscillatory frequency.

Time sequential drawings of the balloon and its center of mass for calculated lateral modes of motion are shown in figure 29. This figure is plotted in a similar fashion to that of figure 7 for the longitudinal analysis, except that the bottom view of the balloon is drawn and the magnitudes of the displacements are proportional to the yaw angle ψ. The plots are drawn by the computer program documented in reference 7 and include the effects of balloon rolling motions and trim pitch angle. Notice in figure 29(a) that mode 1 has split into two nonoscillatory modes of motion for the velocities shown.

Additional configurations.- Results for the configurations corresponding to tests 10, 11, 13, 14, 16, and 17 of table II are presented in figures 30 to 35. These figures show that the measured data correspond to the calculated results for mode 2. No experimental points were measured corresponding to modes 1 or 3 because mode 2 dominated the transient motions of the balloon.

The calculations for mode 2 of test 10 (fig. 30) show a small region where the balloon should have been slightly unstable. Although there were no experimental lateral instabilities observed, the measured data in figure 30 show that the motions were very lightly damped. Furthermore, these motions were observed to become quite large at times and could have been either lightly damped or limit-cycle oscillations.

The effects of changes in the tether-cable length on the lateral modes of motion can be seen by comparing the data from tests 10, 11, and 12 (figs. 30, 31, and 28 and table II). Except for mode 2, the data show that these effects on the lateral modes are similar to, but less pronounced than, those discussed earlier for the longitudinal case. For mode 2, an increase in tether length does not decrease the velocity at which the balloon becomes unstable as in the longitudinal case but causes the damping of the mode to increase at lower velocities and decrease at higher velocities.

Changes in the tether-cable weight and diameter have very little effect on the lateral modes of motion, as shown by the comparison of the data from tests 11, 13, and 14 (figs. 31, 32, and 33 and table II). Note that there are no values of ω and η shown

in figure 33 for test 18 because the balloon went unstable longitudinally for this test and no specific lateral modes of motion were experimentally detected.

The measured damping shown in figure 34 for test 16 is less than analytically predicted. This result is possibly due to coupling between the longitudinal and lateral modes of motion for this configuration.

Lateral trend studies.- Analytical trend studies for the 7.64-m balloon are presented in figures 36 to 44. These figures are presented in a similar format to those for the longitudinal trend studies. A listing of the parameters considered in the lateral trend study is shown in table IV. Except for the term k_{yy}, which is not shown, only those parameters presented in the table have an appreciable effect on the lateral stability boundaries of the balloon in the reference configuration. Nonzero values of k_{yy} have little effect on the lateral stability, but at $k_{yy} = 0$ the balloon is unstable at all velocities. This result indicates that there must be a lateral restraining force provided by the tether cable even though this force can be very small.

The effects of the balloon mass and inertia properties on the lateral stability boundaries are shown in figures 36 to 38. These figures indicate that the stability can be improved if the value of the yaw inertia and apparent mass $m_{y,a}$ are reduced. The center of mass should also be moved farther forward for increased stability.

The effects of buoyancy are shown in figure 39. Figure 39(a) shows that the balloon is only unstable in a very small region at low velocities. Figure 39(b) shows that the present balloon is stable for all values of ℓ_{br} greater than about 0.9.

The analytical results presented in figure 40 indicate that the balloon has a small area of instability for short tether lengths. As mentioned previously, however, no instabilities were found, but large motions were encountered which could indicate the possibility of limit-cycle oscillations or low damping for the short tether-cable conditions.

The effects of the static aerodynamic terms on the lateral-stability boundaries are shown in figure 41. These results are similar to the longitudinal case in that increasing the drag and decreasing the lift cause an increase in the balloon's speed of instability.

The effects of ΔC_{Y_β}, ΔC_{n_β}, and ΔC_{n_r} on the lateral stability boundaries are shown in figures 42 to 44. In general, the terms C_{Y_β}, C_{n_β}, and C_{n_r} must be inherently stable (i.e., C_{Y_β} and C_{n_r} must be negative and C_{n_β} must be positive) if the tethered balloon is to have good lateral stability. Figure 43 shows, however, that C_{n_β} can be slightly negative and the balloon will still be marginally stable because of the restoring moment from the tether cable. The results of figures 42 to 44 indicate that for increased stability the balloon should have a larger vertical tail fin located farther aft of the center of mass.

The results presented in figure 43 show that the roll degree of freedom ϕ has little effect on the stability boundary generated by changes in C_{n_β}. Thus, it appears that the roll degree of freedom has only a moderate effect on the stability characteristics of the present balloon configuration.

CONCLUDING REMARKS

A stability analysis and trend study for a balloon tethered in a steady wind have been presented. Equations of motion are derived which include balloon aerodynamics, aerodynamic apparent mass, structural mass, buoyancy, and static forces resulting from the tether cable. The analysis was applied to a balloon 7.64 m in length and the results were compared with stability data from tow-test experiments. This comparison showed that the analysis gave reasonable predictions for the damping, frequencies, modes of motion, and stability boundaries exhibited by the balloon. Based on these results, it is concluded that the equations and techniques presented in the investigation offer a systematic and useful method for the analysis of the stability of many tethered-balloon systems, particularly those with relatively light tether cables.

The trend studies presented were made by varying individual parameters for the 7.64-m balloon. Significant effects of the magnitude and location of the buoyancy force and the aerodynamic apparent masses were noted. For the longitudinal case, stabilizing effects were also noted as a result of reducing the tether-cable diameter (or drag coefficient), using a more negative C_{m_α} (derivative of pitching moment with respect to angle of attack), increasing the balloon drag coefficient, and decreasing the aerostatic mass. As the tether-cable length was varied, the minimum longitudinal instability speed occurred at an intermediate length, with higher speeds of instability for longer or shorter cable lengths. Fore and aft location of the tether attachment point also had large effects on both trim angle of attack and longitudinal instability. For the lateral case, stable directional stability was necessary for good stability characteristics. For short tether lengths, a small region of lateral instability was calculated for low velocities.

Langley Research Center,
National Aeronautics and Space Administration,
Hampton, Va., May 23, 1973.

APPENDIX A

DERIVATION OF THE EQUATIONS OF MOTION

Rigid-Body Equations of Motion

The kinematic and dynamic equations for rigid-body motion, given in chapter 4 of reference 9, are used in deriving the equations of motion for the tethered-balloon system. The equations of reference 9 are derived about the center of mass in the stability axis system and are as follows:

Summation of forces

$$\Sigma F_X = m\left(\dot{U} + QW - RV\right) \tag{A1a}$$

$$\Sigma F_Y = m\left(\dot{V} + RU - PW\right) \tag{A1b}$$

$$\Sigma F_Z = m\left(\dot{W} + PV - QU\right) \tag{A1c}$$

Summation of moments

$$\Sigma M_X = I_X\dot{P} - I_{XZ}\dot{R} + QR\left(I_Z - I_Y\right) - I_{XZ}PQ \tag{A2a}$$

$$\Sigma M_Y = I_Y\dot{Q} + RP\left(I_X - I_Z\right) + I_{XZ}\left(P^2 - R^2\right) \tag{A2b}$$

$$\Sigma M_Z = -I_{XZ}\dot{P} + I_Z\dot{R} + PQ\left(I_Y - I_X\right) + I_{XZ}QR \tag{A2c}$$

where $I_{XY} = I_{YZ} \equiv 0$ because of symmetry.

Angular velocities

$$P = \dot{\Phi} - \dot{\Psi}\sin\Theta \tag{A3a}$$

$$Q = \dot{\Theta}\cos\Phi + \dot{\Psi}\cos\Theta\sin\Phi \tag{A3b}$$

$$R = \dot{\Psi}\cos\Theta\cos\Phi - \dot{\Theta}\sin\Phi \tag{A3c}$$

Linear velocities

$$\frac{dx'}{dt} = U\cos\Theta\cos\Psi + V(\sin\Phi\sin\Theta\cos\Psi - \cos\Phi\sin\Psi) + W(\cos\Phi\sin\Theta\cos\Psi + \sin\Phi\sin\Psi) \tag{A4a}$$

$$\frac{dy'}{dt} = U \cos \Theta \sin \Psi + V(\sin \Phi \sin \Theta \sin \Psi + \cos \Phi \cos \Psi) + W(\cos \Phi \sin \Theta \sin \Psi - \sin \Phi \cos \Psi) \tag{A4b}$$

$$\frac{dz'}{dt} = -U \sin \Theta + V \sin \Phi \cos \Theta + W \cos \Phi \cos \Theta \tag{A4c}$$

The axis systems, motions, forces, and moments included in the above equations are shown in figures 1, 2, and 3.

The preceding equations of motion can be adapted to describe the motions of a tethered balloon by using the assumptions given in the section entitled "Analysis" of this paper. These assumptions require that the balloon center of mass has no displacements or velocities for equilibrium trim conditions. Thus, the only movements which the balloon exhibits are small perturbations about its initial trimmed position. Hence, for small displacements, the following linearized relationships are obtained (ref. 9):

$$U = u; \quad V = v; \quad W = w \tag{A5a}$$

$$\Theta = \theta; \quad \Psi = \psi; \quad \Phi = \phi \tag{A5b}$$

$$P = p; \quad Q = q; \quad R = r \tag{A5c}$$

where the lower-case letters denote small perturbation velocities and displacements of the center of mass.

In contrast with conventional-airplane analyses (ref. 9), the expression for the x-component of velocity U in equation (A5a) does not include the equilibrium velocity term V_∞. The reason for the difference is that in the conventional analysis the airplane moves through still air at a speed equal to the equilibrium velocity plus the perturbation velocity, whereas in the present analysis the balloon is tethered from an earth-fixed anchor point and the only movements of the balloon are small perturbation motions. The airstream does flow over the balloon at a constant equilibrium velocity in the present analysis, but the airstream velocity only affects the magnitude of the aerodynamic forces and is not an explicit part of the motion of the center of mass.

Using equations (A5) in equations (A3) and (A4) and retaining only first-order perturbation terms gives

$$p = \dot{\phi}; \quad q = \dot{\theta}; \quad r = \dot{\psi} \tag{A6}$$

$$\dot{x}' = u; \quad \dot{y}' = v; \quad \dot{z}' = w \tag{A7}$$

Substituting equations (A5), (A6), and (A7) into equations (A1) and (A2), and retaining only first-order terms, results in the following linear equations of motion:

$$\Sigma F_X = m\ddot{x}' \tag{A8a}$$

$$\Sigma F_Y = m\ddot{y}' \tag{A8b}$$

$$\Sigma F_Z = m\ddot{z}' \tag{A8c}$$

$$\Sigma M_X = I_x\ddot{\phi} - I_{xz}\ddot{\psi} \tag{A9a}$$

$$\Sigma M_Y = I_y\ddot{\theta} \tag{A9b}$$

$$\Sigma M_Z = -I_{xz}\ddot{\phi} + I_z\ddot{\psi} \tag{A9c}$$

Apparent masses and moments of inertia.- The balloon system mass term m used in equations (A8) includes the structural mass of the balloon m_s, the mass of the gas inside the balloon m_g, and the apparent mass m_a of the air associated with the accelerations of the balloon. Since the apparent mass of streamlined bodies and prolate spheroids accelerating in the axial direction is different from that for accelerations in a lateral direction (ref. 14), the following relationships for the present balloon system are introduced:

$$m_{x,o} = m_s + m_g + m_{a_1} \tag{A10a}$$

$$m_{y,o} = m_s + m_g + m_{a_2} \tag{A10b}$$

$$m_{z,o} = m_s + m_g + m_{a_3} \tag{A10c}$$

where $m_{x,o}$, $m_{y,o}$, and $m_{z,o}$ are the total masses and m_{a_1}, m_{a_2}, and m_{a_3} are the apparent masses associated with accelerations in the x-, y-, and z-directions, respectively.

The apparent mass of the balloon moving in the x- and z-directions also depends upon the equilibrium trim angle of attack α_t such that

$$m_{a_1} = m_{x,a}\cos^2\alpha_t + m_{z,a}\sin^2\alpha_t \tag{A11a}$$

$$m_{a_2} = m_{y,a} \tag{A11b}$$

$$m_{a_3} = m_{x,a}\sin^2\alpha_t + m_{z,a}\cos^2\alpha_t \tag{A11c}$$

where $m_{x,a}$, $m_{y,a}$, and $m_{z,a}$ are the apparent masses of the balloon accelerating along the X''-, Y''-, and Z''-axes.

Because the apparent mass depends upon the direction of the acceleration, the expressions given in equations (A8) are written

$$\Sigma F_X = m_{x,o}\ddot{x}' \tag{A12a}$$

$$\Sigma F_Y = m_{y,o}\ddot{y}' \tag{A12b}$$

$$\Sigma F_Z = m_{z,o}\ddot{z}' \tag{A12c}$$

where the expressions for $m_{x,o}$, $m_{y,o}$, and $m_{z,o}$ are given in equations (A10).

The mass moments of inertia given in equations (A9) also include the inertias of the balloon structure, the gas inside the balloon, and the apparent mass of the surrounding air. Furthermore, these moments of inertia depend upon the orientation of the balloon as described by the following equations:

$$I_X = I_{XX}\cos^2\epsilon + I_{ZZ}\sin^2\epsilon \tag{A13a}$$

$$I_{XZ} = \frac{1}{2}(I_{XX} - I_{ZZ})\sin 2\epsilon \tag{A13b}$$

$$I_Y = I_{YY} \tag{A13c}$$

$$I_Z = I_{XX}\sin^2\epsilon + I_{ZZ}\cos^2\epsilon \tag{A13d}$$

where I_{XX}, I_{YY}, and I_{ZZ} are the mass moments of inertia about the principal axes and ϵ is the angle between the principal X-axis and the stability X-axis. In the present analysis, the X''-, Y''-, and Z''-axes are considered to be the principal axes; hence, $\epsilon = \alpha_t$.

Forces and moments acting on the balloon.- There are four different sources of external forces and moments acting on the balloon as shown in figures 1, 2, and 4. These are: (1) aerodynamic forces, (2) tether-cable forces, (3) buoyancy forces, and (4) gravity forces. Therefore, the equations of motion for the balloon as given in equations (A12) and (A9) can be written as

$$F_{X,A} + F_{X,C} + F_{X,B} + F_{X,G} = m_{x,o}\ddot{x}' \tag{A14a}$$

$$F_{Y,A} + F_{Y,C} + F_{Y,B} + F_{Y,G} = m_{y,o}\ddot{y}' \tag{A14b}$$

$$F_{Z,A} + F_{Z,C} + F_{Z,B} + F_{Z,G} = m_{z,o}\ddot{z}' \tag{A14c}$$

$$M_{X,A} + M_{X,C} + M_{X,B} + M_{X,G} = I_x\ddot{\phi} - I_{xz}\ddot{\psi} \tag{A15a}$$

$$M_{Y,A} + M_{Y,C} + M_{Y,B} + M_{Y,G} = I_y\ddot{\theta} \tag{A15b}$$

$$M_{Z,A} + M_{Z,C} + M_{Z,B} + M_{Z,G} = -I_{xz}\ddot{\phi} + I_z\ddot{\psi} \tag{A15c}$$

where the A, C, B, and G subscripts denote aerodynamic, tether-cable, buoyancy, and gravity terms, respectively. The expressions for each of the external forces and moments are derived in the following four sections.

Aerodynamic Forces and Moments

The aerodynamic forces and moments about the balloon center of mass are derived in essentially the same manner as used in reference 9. In deriving these aerodynamic terms, the following assumptions are made:

(1) The aerodynamic forces and moments are functions of the instantaneous values of the perturbation velocities and accelerations of the balloon with respect to the airstream.

(2) The perturbation velocities of the balloon with respect to the airstream are u, v*, and w*.

(3) The longitudinal and lateral forces and moments are independent.

(4) All aerodynamic derivatives with respect to acceleration quantities are neglected, except $F_{Z_{\dot{w}^*}}$, $M_{Y_{\dot{w}^*}}$, $F_{Y_{\dot{v}^*}}$, $L_{\dot{v}^*}$, and $M_{Z_{\dot{v}^*}}$.

(5) The $F_{X_{\dot{\theta}}}$ derivative is very small and may be neglected (ref. 9).

(6) The equilibrium trim values of the longitudinal aerodynamic forces are $F_{X,A_t} = -D_t$ and $F_{Z,A_t} = -L_t$.

(7) The equilibrium trim values of the lateral aerodynamic forces and moments F_{Y,A_t}, M_{X,A_t}, and M_{Z,A_t} are zero.

Using the preceding assumptions and equation (A6), the aerodynamic forces and moments are:

$$F_{X,A} = -D_t + F_{X_u}u + F_{X_{w^*}}w^* \tag{A16a}$$

$$F_{Y,A} = F_{Y_{v^*}}v^* + F_{Y_{\dot{v}^*}}\dot{v}^* + F_{Y_p}\dot{\phi} + F_{Y_r}\dot{\psi} \tag{A16b}$$

$$F_{Z,A} = -L_t + F_{Z_u}u + F_{Z_{w^*}}w^* + F_{Z_{\dot{w}^*}}\dot{w}^* + F_{Z_q}\dot{\theta} \tag{A16c}$$

$$M_{X,A} = M_{X_{v^*}} v^* + M_{X_{\dot{v}^*}} \dot{v}^* + M_{X_p} \dot{\phi} + M_{X_r} \dot{\psi} \tag{A16d}$$

$$M_{Y,A} = M_{Y,A_t} + M_{Y_u} u + M_{Y_{w^*}} w^* + M_{Y_{\dot{w}^*}} \dot{w}^* + M_{Y_q} \dot{\theta} \tag{A16e}$$

$$M_{Z,A} = M_{Z_{v^*}} v^* + M_{Z_{\dot{v}^*}} \dot{v}^* + M_{Z_p} \dot{\phi} + M_{Z_r} \dot{\psi} \tag{A16f}$$

where

$$F_{X_u} = \frac{\partial F_{X,A}}{\partial u}, \quad M_{Y_{\dot{w}^*}} = \frac{\partial M_{Y,A}}{\partial \dot{w}^*}, \quad M_{Y_q} = \frac{\partial M_{Y,A}}{\partial q}, \quad M_{Z_p} = \frac{\partial M_{Z,A}}{\partial p}, \ldots$$

The first-order approximations of the perturbation angle of attack α and sideslip β are (ref. 9):

$$\alpha = \frac{w^*}{V_\infty}$$

$$\beta = \frac{v^*}{V_\infty}$$

Applying this approximation to equations (A16) and expanding α in terms of $\dot{z}'/V_\infty$ and θ, and β in terms of $\dot{y}'/V_\infty$ and ψ, gives the following results:

$$F_{X,A} = -D_t + F_{X_u} \dot{x}' + F_{X_\alpha} \frac{\dot{z}'}{V_\infty} + F_{X_\alpha} \theta \tag{A17a}$$

$$F_{Y,A} = F_{Y_{\dot{\beta}}} \frac{\ddot{y}'}{V_\infty} + F_{Y_\beta} \frac{\dot{y}'}{V_\infty} + F_{Y_p} \dot{\phi} + \left(F_{Y_r} - F_{Y_{\dot{\beta}}}\right) \dot{\psi} - F_{Y_\beta} \psi \tag{A17b}$$

$$F_{Z,A} = -L_t + F_{Z_u} \dot{x}' + F_{Z_{\dot{\alpha}}} \frac{\ddot{z}'}{V_\infty} + F_{Z_\alpha} \frac{\dot{z}'}{V_\infty} + \left(F_{Z_q} + F_{Z_{\dot{\alpha}}}\right) \dot{\theta} + F_{Z_\alpha} \theta \tag{A17c}$$

$$M_{X,A} = M_{X_{\dot{\beta}}} \frac{\ddot{y}'}{V_\infty} + M_{X_\beta} \frac{\dot{y}'}{V_\infty} + M_{X_p} \dot{\phi} + \left(M_{X_r} - M_{X_{\dot{\beta}}}\right) \dot{\psi} - M_{X_\beta} \psi \tag{A17d}$$

$$M_{Y,A} = M_{Y_t} + M_{Y_u} \dot{x}' + M_{Y_{\dot{\alpha}}} \frac{\ddot{z}'}{V_\infty} + M_{Y_\alpha} \frac{\dot{z}'}{V_\infty} + \left(M_{Y_q} + M_{Y_{\dot{\alpha}}}\right) \dot{\theta} + M_{Y_\alpha} \theta \tag{A17e}$$

$$M_{Z,A} = M_{Z_{\dot{\beta}}} \frac{\ddot{y}'}{V_\infty} + M_{Z_\beta} \frac{\dot{y}'}{V_\infty} + M_{Z_p} \dot{\phi} + \left(M_{Z_r} - M_{Z_{\dot{\beta}}}\right) \dot{\psi} - M_{Z_\beta} \psi \tag{A17f}$$

For small perturbation angles of attack α, the longitudinal forces can be expressed in terms of the aerodynamic lift and drag as

$$F_{X,A} = (L\alpha - D) \tag{A18a}$$

$$F_{Z,A} = -(L + D\alpha) \tag{A18b}$$

Taking the u, α, $\dot{\alpha}$, and q derivatives of equations (A18) and substituting these results into equations (A17a) and (A17c) gives the following expressions:

$$F_{X,A} = -D_t - D_u\dot{x}' - \left(D_\alpha - L\right)\frac{\dot{z}'}{V_\infty} - \left(D_\alpha - L\right)\theta \tag{A19a}$$

$$F_{Z,A} = -L_t - L_u\dot{x}' - L_{\dot{\alpha}}\frac{\ddot{z}'}{V_\infty} - \left(L_\alpha + D\right)\frac{\dot{z}'}{V_\infty} - \left(L_q + L_{\dot{\alpha}}\right)\dot{\theta} - \left(L_\alpha + D\right)\theta \tag{A19b}$$

where the higher-order perturbation terms are neglected.

The aerodynamic forces and moments in equations (A19), (A17b), and (A17d) to (A17f) are nondimensionalized by the methods used in reference 9. The resulting aerodynamic coefficients in these equations are then evaluated at trim conditions and the higher-order perturbation terms are neglected. The following relationships are thus obtained:

$$F_{X,A} = -\left[\frac{\rho V_\infty S}{2}\left(2C_D + C_{D_u}\right)\right]\dot{x}' - \left[\frac{\rho V_\infty S}{2}\left(C_{D_\alpha} - C_L\right)\right]\dot{z}' - \left[\frac{\rho V_\infty{}^2 S}{2}\left(C_{D_\alpha} - C_L\right)\right]\theta - \frac{\rho V_\infty{}^2 S}{2}C_D \tag{A20a}$$

$$F_{Y,A} = \left(\frac{\rho S\bar{c}}{4}C_{Y_{\dot{\beta}}}\right)\ddot{y}' + \left(\frac{\rho V_\infty S}{2}C_{Y_\beta}\right)\dot{y}' + \left(\frac{\rho V_\infty S\bar{c}}{4}C_{Y_p}\right)\dot{\phi} - \left[\frac{\rho V_\infty S\bar{c}}{4}\left(C_{Y_{\dot{\beta}}} - C_{Y_p}\right)\right]\dot{\psi} - \left(\frac{\rho V_\infty{}^2 S}{2}C_{Y_\beta}\right)\psi \tag{A20b}$$

$$F_{Z,A} = -\left[\frac{\rho V_\infty S}{2}\left(2C_L + C_{L_u}\right)\right]\dot{x}' - \left(\frac{\rho S\bar{c}}{4}C_{L_{\dot{\alpha}}}\right)\ddot{z}' - \left[\frac{\rho V_\infty S}{2}\left(C_{L_\alpha} + C_D\right)\right]\dot{z}' - \left[\frac{\rho V_\infty S\bar{c}}{4}\left(C_{L_{\dot{\alpha}}} + C_{L_q}\right)\right]\dot{\theta} - \left[\frac{\rho V_\infty{}^2 S}{2}\left(C_{L_\alpha} + C_D\right)\right]\theta - \frac{\rho V_\infty{}^2 S}{2}C_L \tag{A20c}$$

$$M_{X,A} = \left[\frac{\rho S(\bar{c})^2}{4} C_{l_{\dot{\beta}}}\right]\ddot{y}' + \left(\frac{\rho V_\infty S\bar{c}}{2} C_{l_\beta}\right)\dot{y}' + \left[\frac{\rho V_\infty S(\bar{c})^2}{4} C_{l_p}\right]\dot{\phi} - \frac{\rho V_\infty S(\bar{c})^2}{4}\left(C_{l_{\dot{\beta}}} - C_{l_r}\right)\dot{\psi}$$

$$- \left(\frac{\rho V_\infty^2 S\bar{c}}{2} C_{l_\beta}\right)\psi \tag{A20d}$$

$$M_{Y,A} = \left[\frac{\rho V_\infty S\bar{c}}{2}\left(2C_m + C_{m_u}\right)\right]\dot{x}' + \left[\frac{\rho S(\bar{c})^2}{4} C_{m_{\dot{\alpha}}}\right]\ddot{z}' + \left(\frac{\rho V_\infty S\bar{c}}{2} C_{m_\alpha}\right)\dot{z}'$$

$$+ \left[\frac{\rho V_\infty S(\bar{c})^2}{4}\left(C_{m_{\dot{\alpha}}} + C_{m_q}\right)\right]\dot{\theta} + \left[\frac{\rho V_\infty^2 S\bar{c}}{2} C_{m_\alpha}\right]\theta + \frac{\rho V_\infty^2 S\bar{c}}{2} C_m \tag{A20e}$$

$$M_{Z,A} = \left[\frac{\rho S(\bar{c})^2}{4} C_{n_{\dot{\beta}}}\right]\ddot{y}' + \left(\frac{\rho V_\infty S\bar{c}}{2} C_{n_\beta}\right)\dot{y}' + \left[\frac{\rho V_\infty S(\bar{c})^2}{4} C_{n_p}\right]\dot{\phi} - \left[\frac{\rho V_\infty S(\bar{c})^2}{4}\left(C_{n_{\dot{\beta}}} - C_{n_r}\right)\right]\dot{\psi}$$

$$- \left(\frac{\rho V_\infty^2 S\bar{c}}{2} C_{n_\beta}\right)\psi \tag{A20f}$$

Tether-Cable Forces and Moments

The basic expressions for the tether-cable forces, given in reference 2, are derived in appendix B. In terms of the earth-fixed coordinate system, they are

$$F_{X',C} = T_1 \cos\gamma_1 - k_{xx}x'_c - k_{xz}z'_c \tag{A21a}$$

$$F_{Y',C} = -k_{yy}y'_c \tag{A21b}$$

$$F_{Z',C} = T_1 \sin\gamma_1 - k_{zx}x'_c - k_{zz}z'_c \tag{A21c}$$

Assuming small perturbation angles, these forces can be written in the stability axis system (fig. 3) as follows

$$F_{X,C} = F_{X',C} + F_{Y',C}\psi - F_{Z',C}\theta \tag{A22a}$$

$$F_{Y,C} = -F_{X',C}\psi + F_{Y',C} + F_{Z',C}\phi \tag{A22b}$$

$$F_{Z,C} = F_{X',C}\theta - F_{Y',C}\phi + F_{Z',C} \tag{A22c}$$

In order to obtain moments about the balloon center of mass in the stability axis system, the coordinates of the bridle confluence point with respect to the center of mass must be determined. By inspection (fig. 4) these are

$$h_{k_1} = \left(l_{tr} - l_{cg}\right)\cos \alpha_t + \left(t_{tr} - h_{cg}\right)\sin \alpha_t \tag{A23a}$$

$$h_{k_2} = \left(t_{tr} - h_{cg}\right)\cos \alpha_t - \left(l_{tr} - l_{cg}\right)\sin \alpha_t \tag{A23b}$$

Therefore, the tether-cable moments about the balloon center of mass in the stability axis system are

$$M_{X,C} = -h_{k_2} F_{Y,C} \tag{A24a}$$

$$M_{Y,C} = h_{k_2} F_{X,C} - h_{k_1} F_{Z,C} \tag{A24b}$$

$$M_{Z,C} = h_{k_1} F_{Y,C} \tag{A24c}$$

The displacements x'_c, y'_c, and z'_c of the upper end of the cable can be expressed in terms of the displacement of the balloon center of mass plus the rotation of the bridle confluence point about the center of mass. For small perturbations these displacements are

$$x'_c = x' + h_{k_2}\theta \tag{A25a}$$

$$y'_c = y' + h_{k_1}\psi - h_{k_2}\phi \tag{A25b}$$

$$z'_c = z' - h_{k_1}\theta \tag{A25c}$$

Substituting equations (A21) and (A25) into equations (A22) and (A24) and neglecting higher order terms gives

$$F_{X,C} = -k_{xx}x' - k_{xz}z' - \left(k_{x\theta} + T_1 \sin \gamma_1\right)\theta + T_1 \cos \gamma_1 \tag{A26a}$$

$$F_{Y,C} = -k_{yy}y' + \left(T_1 \sin \gamma_1 - k_{y\phi}\right)\phi - \left(T_1 \cos \gamma_1 + k_{y\psi}\right)\psi \tag{A26b}$$

$$F_{Z,C} = -k_{zx}x' - k_{zz}z' + \left(T_1 \cos \gamma_1 - k_{z\theta}\right)\theta + T_1 \sin \gamma_1 \tag{A26c}$$

$$M_{X,C} = -k_{\phi y}y' - \left(h_{k_2}T_1 \sin \gamma_1 + k_{\phi\phi}\right)\phi + \left(h_{k_2}T_1 \cos \gamma_1 - k_{\phi\psi}\right)\psi \tag{A26d}$$

$$M_{Y,C} = -k_{\theta x}x' - k_{\theta z}z' - k_{\theta\theta}\theta - h_{k_1}T_1 \sin \gamma_1 + h_{k_2}T_1 \cos \gamma_1 \tag{A26e}$$

$$M_{Z,C} = -k_{\psi y}y' + \left(h_{k_1}T_1 \sin \gamma_1 - k_{\psi\phi}\right)\phi - \left(h_{k_1}T_1 \cos \gamma_1 + k_{\psi\psi}\right)\psi \tag{A26f}$$

where

$$k_{x\theta} = h_{k_2}k_{xx} - h_{k_1}k_{xz} \tag{A27a}$$

$$k_{z\theta} = h_{k_2}k_{zx} - h_{k_1}k_{zz} \tag{A27b}$$

$$k_{\theta x} = h_{k_2}k_{xx} - h_{k_1}k_{zx} \tag{A27c}$$

$$k_{\theta z} = h_{k_2}k_{xz} - h_{k_1}k_{zz} \tag{A27d}$$

$$k_{\theta\theta} = k_{\theta\theta_D} + k_{\theta\theta_T} \tag{A27e}$$

$$k_{\theta\theta_D} = h_{k_2}^2 k_{xx} - h_{k_2}h_{k_1}\left(k_{xz} + k_{zx}\right) + h_{k_1}^2 k_{zz} \tag{A27f}$$

$$k_{\theta\theta_T} = h_{k_2}\left(T_1 \sin \gamma_1\right) + h_{k_1}\left(T_1 \cos \gamma_1\right) \tag{A27g}$$

$$k_{y\phi} = -h_{k_2}k_{yy} \tag{A27h}$$

$$k_{y\psi} = h_{k_1}k_{yy} \tag{A27i}$$

$$k_{\phi y} = k_{y\phi} \tag{A27j}$$

$$k_{\phi\phi} = h_{k_2}^2 k_{yy} \tag{A27k}$$

$$k_{\phi\psi} = -h_{k_1}h_{k_2}k_{yy} \tag{A27l}$$

$$k_{\psi y} = k_{y\psi} \tag{A27m}$$

$$k_{\psi\phi} = k_{\phi\psi} \tag{A27n}$$

$$k_{\psi\psi} = h_{k_1}^2 k_{yy} \tag{A27o}$$

Buoyancy Forces and Moments

The expressions for the buoyancy forces and moments about the center of mass in the stability axis system can be determined by inspection (figs. 1, 3, and 4). Assuming small perturbation angles, these are

$$F_{X,B} = B\theta \tag{A28a}$$

$$F_{Y,B} = -B\phi \tag{A28b}$$

$$F_{Z,B} = -B \tag{A28c}$$

$$M_{X,B} = -B\left[\left(h_{cg} - h_{br}\right)\cos \alpha_t + \left(l_{br} - l_{cg}\right)\sin \alpha_t\right]\phi \tag{A28d}$$

$$M_{Y,B} = B\left[\left(l_{br} - l_{cg}\right)\cos \alpha_t - \left(h_{cg} - h_{br}\right)\sin \alpha_t\right] - B\left[\left(h_{cg} - h_{br}\right)\cos \alpha_t + \left(l_{br} - l_{cg}\right)\sin \alpha_t\right]\theta \tag{A28e}$$

$$M_{Z,B} = -B\left[\left(l_{br} - l_{cg}\right)\cos \alpha_t - \left(h_{cg} - h_{br}\right)\sin \alpha_t\right]\phi \tag{A28f}$$

Gravity Forces and Moments

In deriving the gravity forces for the equations of motion, only the components due to the structural weight of the balloon need to be considered. The effects of the apparent mass and the lifting gas are already included in the coefficients of the acceleration and buoyancy terms, respectively.

The forces and moments due to gravity are determined by inspection (figs. 1, 3, and 4) and for small perturbation angles are

$$F_{X,G} = -W_s\theta \tag{A29a}$$

$$F_{Y,G} = W_s\phi \tag{A29b}$$

$$F_{Z,G} = W_s \tag{A29c}$$

$$M_{X,G} = -W_s\left[\left(h_{sr} - h_{cg}\right)\cos \alpha_t + \left(l_{sr} + l_{cg}\right)\sin \alpha_t\right]\phi \tag{A29d}$$

$$M_{Y,G} = W_s\left[\left(l_{sr} + l_{cg}\right)\cos\alpha_t - \left(h_{sr} - h_{cg}\right)\sin\alpha_t\right] - W_s\left[\left(h_{sr} - h_{cg}\right)\cos\alpha_t + \left(l_{sr} + l_{cg}\right)\sin\alpha_t\right]\theta \tag{A29e}$$

$$M_{Z,G} = -W_s\left[\left(l_{sr} + l_{cg}\right)\cos\alpha_t - \left(h_{sr} - h_{cg}\right)\sin\alpha_t\right]\phi \tag{A29f}$$

Balloon Equations of Motion

If the expressions for each of the external forces and moments (eqs. (A20), (A26), (A28), and (A29)) are substituted into equations (A14) and (A15), the resulting equations of motion about the balloon center of mass are as follows:

x-force

$$(m_x)\ddot{x}' + \left[\frac{\rho V_\infty S}{2}\left(2C_D + C_{D_u}\right)\right]\dot{x}' + \left(k_{xx}\right)x' + \left[\frac{\rho V_\infty S}{2}\left(C_{D_\alpha} - C_L\right)\right]z' + \left(k_{xz}\right)z' + \left[k_{x\theta} + \frac{\rho V_\infty{}^2 S}{2}\left(C_{D_\alpha} - C_L\right) - \left(B - W_s\right) + T_1\sin\gamma_1\right]\theta + \frac{\rho V_\infty{}^2 S}{2}C_D - T_1\cos\gamma_1 = 0 \tag{A30a}$$

y-force

$$(m_y)\ddot{y}' - \left(\frac{\rho V_\infty S}{2}C_{Y_\beta}\right)\dot{y}' + \left(k_{yy}\right)y' - \left(\frac{\rho V_\infty S\bar{c}}{4}C_{Y_p}\right)\dot{\phi} + \left[k_{y\phi} - T_1\sin\gamma_1 + \left(B - W_s\right)\right]\phi + \left[\frac{\rho V_\infty S\bar{c}}{4}\left(C_{Y_{\dot\beta}} - C_{Y_r}\right)\right]\dot{\psi} + \left(k_{y\psi} + T_1\cos\gamma_1 + \frac{\rho V_\infty{}^2 S}{2}C_{Y_\beta}\right)\psi = 0 \tag{A30b}$$

z-force

$$\left[\frac{\rho V_\infty S}{2}\left(2C_L + C_{L_u}\right)\right]\dot{x}' + \left(k_{zx}\right)x' + (m_z)\ddot{z}' + \left[\frac{\rho V_\infty S}{2}\left(C_{L_\alpha} + C_D\right)\right]\dot{z}' + \left(k_{zz}\right)z' + \left[\frac{\rho V_\infty S\bar{c}}{4}\left(C_{L_{\dot\alpha}} + C_{L_q}\right)\right]\dot{\theta} + \left[\frac{\rho V_\infty{}^2 S}{2}\left(C_{L_\alpha} + C_D\right) - T_1\cos\gamma_1 + k_{z\theta}\right]\theta + \frac{\rho V_\infty{}^2 S}{2}C_L + B - W_s - T_1\sin\gamma_1 = 0 \tag{A30c}$$

Rolling moment

$$-\left[\frac{\rho S(\bar{c})^2}{4} C_{l_{\dot{\beta}}}\right]\ddot{y}' - \left[\frac{\rho V_\infty S\bar{c}}{2} C_{l_\beta}\right]\dot{y}' + \left(k_{\phi y}\right)y' + \left(I_x\right)\ddot{\phi} - \left[\frac{\rho V_\infty S(\bar{c})^2}{4} C_{l_p}\right]\dot{\phi}$$

$$+\left[h_{k_2} T_1 \sin\gamma_1 + k_{\phi\phi} + M_{s_1}\right]\phi - \left(I_{xz}\right)\ddot{\psi} + \left[\frac{\rho V_\infty S(\bar{c})^2}{4}\left(C_{l_{\dot{\beta}}} - C_{l_r}\right)\right]\dot{\psi}$$

$$+\left(\frac{\rho V_\infty{}^2 S\bar{c}}{2} C_{l_\beta} - h_{k_2} T_1 \cos\gamma_1 + k_{\phi\psi}\right)\psi = 0 \qquad \text{(A30d)}$$

Pitching moment

$$-\left[\frac{\rho V_\infty S\bar{c}}{2}\left(2C_m + C_{m_u}\right)\right]\dot{x}' + \left(k_{\theta x}\right)x' - \left[\frac{\rho S(\bar{c})^2}{4} C_{m_{\dot{\alpha}}}\right]\ddot{z}' - \left(\frac{\rho V_\infty S\bar{c}}{2} C_{m_\alpha}\right)\dot{z}' + \left(k_{\theta z}\right)z'$$

$$+\left(I_y\right)\ddot{\theta} - \left[\frac{\rho V_\infty S(\bar{c})^2}{4}\left(C_{m_{\dot{\alpha}}} + C_{m_q}\right)\right]\dot{\theta} + \left(k_{\theta\theta} + M_{s_1} - \frac{\rho V_\infty{}^2 S\bar{c}}{2} C_{m_\alpha}\right)\theta - \frac{\rho V_\infty{}^2 S\bar{c}}{2} C_m$$

$$+ h_{k_1} T_1 \sin\gamma_1 - h_{k_2} T_1 \cos\gamma_1 - M_{s_2} = 0 \qquad \text{(A30e)}$$

Yawing moment

$$-\left[\frac{\rho S(\bar{c})^2}{4} C_{n_{\dot{\beta}}}\right]\ddot{y}' - \left(\frac{\rho V_\infty S\bar{c}}{2} C_{n_\beta}\right)\dot{y}' + \left(k_{\psi y}\right)y' - \left(I_{xz}\right)\ddot{\phi} - \left[\frac{\rho V_\infty S(\bar{c})^2}{4} C_{n_p}\right]\dot{\phi}$$

$$+\left(M_{s_2} + k_{\psi\phi} - h_{k_1} T_1 \sin\gamma_1\right)\phi + \left(I_z\right)\ddot{\psi} + \left[\frac{\rho V_\infty S(\bar{c})^2}{4}\left(C_{n_{\dot{\beta}}} - C_{n_r}\right)\right]\dot{\psi}$$

$$+\left(\frac{\rho V_\infty{}^2 S\bar{c}}{2} C_{n_\beta} + h_{k_1} T_1 \cos\gamma_1 + k_{\psi\psi}\right)\psi = 0 \qquad \text{(A30f)}$$

where

$$M_{s_1} = \left[\left(l_{br} - l_{cg}\right)B + \left(l_{sr} + l_{cg}\right)W_s\right]\sin\alpha_t + \left[\left(h_{cg} - h_{br}\right)B + \left(h_{sr} - h_{cg}\right)W_s\right]\cos\alpha_t \qquad \text{(A31a)}$$

$$M_{s_2} = \left[\left(l_{br} - l_{cg}\right)B + \left(l_{sr} + l_{cg}\right)W_s\right]\cos\alpha_t - \left[\left(h_{cg} - h_{br}\right)B + \left(h_{sr} - h_{cg}\right)W_s\right]\sin\alpha_t \qquad \text{(A31b)}$$

and

$$m_X = m_{X,o} \tag{A32a}$$

$$m_y = m_{y,o} - \frac{\rho S \bar{c}}{4} C_{Y_{\dot{\beta}}} \tag{A32b}$$

$$m_Z = m_{Z,o} + \frac{\rho S \bar{c}}{4} C_{L_{\dot{\alpha}}} \tag{A32c}$$

APPENDIX B

TETHER-CABLE CONFIGURATION AND FORCES

The analysis of the cable shape and the forces exerted by the cable on the balloon bridle given in appendix B is adapted from the analysis of S. Neumark (ref. 2). The coordinate system and the forces acting on the cable are shown in the following sketch:

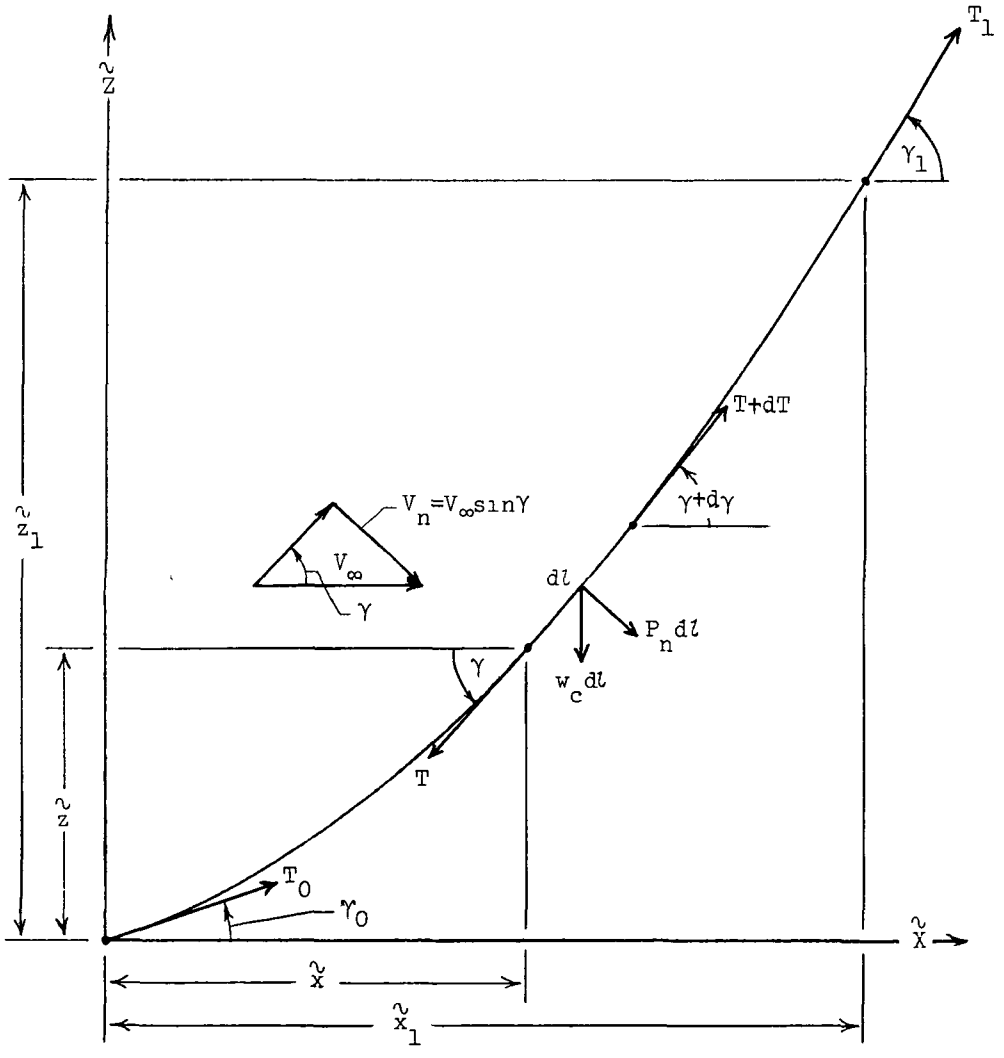

Note that this coordinate system of appendix B is different from those employed elsewhere in the paper.

Close examination of the expressions given in appendix B will show that many of the equations are invalid if either the cable weight per unit length w_c or cable drag per unit

length n is zero. The proper expressions in these limiting cases are given in reference 2.

Equilibrium Cable Shape

The forces acting on an element of the cable of length $d\ell$ (see sketch) are the tension T, cable weight $w_c\, d\ell$, and cable drag $P_n\, d\ell$ normal to the cable. Drag along the cable is neglected in this analysis. The normal drag force per unit length P_n depends on the component of wind velocity normal to the cable V_n, the cable drag coefficient C_{D_c}, and cable diameter d_c as follows:

$$P_n = C_{D_c} d_c \frac{1}{2} \rho V_n^2 \tag{B1}$$

Retaining only first-order terms in the infinitesimals, the drag on the element is

$$P_n\, d\ell = n\, d\ell \sin^2\gamma \tag{B2}$$

where

$$n = C_{D_c} d_c \frac{1}{2} \rho V_\infty^2 \tag{B3}$$

is the cable drag per unit length for a cable normal to the wind. Summing the x- and z-forces and retaining only first-order terms yields

$$P_n\, d\ell \sin\gamma - T\, d\gamma \sin\gamma + dT \cos\gamma = 0 \tag{B4a}$$

$$-w_c\, d\ell - P_n\, d\ell \cos\gamma + T\, d\gamma \cos\gamma + dT \sin\gamma = 0 \tag{B4b}$$

These equations may be combined to give

$$dT = w_c\, d\ell \sin\gamma \tag{B5}$$

$$T\, d\gamma = \left(n \sin^2\gamma + w_c \cos\gamma\right) d\ell \tag{B6}$$

Dividing these equations gives

$$\frac{dT}{T} = \frac{2\bar{p} \sin\gamma}{\sin^2\gamma + 2\bar{p} \cos\gamma}\, d\gamma \tag{B7}$$

where $\bar{p} = \frac{w_c}{2n}$. Using the substitution $f = \cos\gamma$ and partial-fraction decomposition in equation (B7) to obtain

$$\frac{dT}{T} = -\frac{\bar{p}}{\bar{q}}\left(\frac{df}{\bar{q} + \bar{p} - f} + \frac{df}{\bar{q} - \bar{p} + f}\right) \tag{B8}$$

where $\bar{q} = \sqrt{1 + (\bar{p})^2}$, and integrating from the upper end of the cable yields

$$T = \frac{T_1 \tau}{\tau_1} \tag{B9a}$$

where

$$\tau(\gamma) = \left(\frac{\bar{q} + \bar{p} - \cos\gamma}{\bar{q} - \bar{p} + \cos\gamma}\right)^{\bar{p}/\bar{q}} \tag{B9b}$$

For present purposes it is assumed that the cable length l, drag per unit length n, weight per unit length w_c, tension at the upper end T_1, and angle of the upper end γ_1 are known. The procedure required to determine the coordinates of the upper end of the cable $\tilde{x}_1$ and $\tilde{z}_1$, the tension at the lower end T_0, and the angle of the lower end γ_0 is outlined as follows: Substituting equations (B9) in equation (B6) gives

$$dl = \frac{T_1}{n\tau_1} \frac{\tau}{\sin^2\gamma + 2\bar{p}\cos\gamma} d\gamma \tag{B10}$$

Integration of this equation from the lower end to upper end yields

$$l = \frac{T_1}{n\tau_1}\left(\bar{\lambda}_1 - \bar{\lambda}_0\right) \tag{B11}$$

where

$$\bar{\lambda}(\gamma) = \int_0^{\gamma} \frac{\tau(\gamma)}{\sin^2\gamma + 2\bar{p}\cos\gamma} d\gamma \tag{B12}$$

$\bar{\lambda}_0 = \bar{\lambda}(\gamma_0)$, and $\bar{\lambda}_1 = \bar{\lambda}(\gamma_1)$. The angle γ_0 is unknown, but may be obtained by solving equation (B11) for

$$\bar{\lambda}_0 = \bar{\lambda}_1 - \frac{n\tau_1 l}{T_1} \tag{B13}$$

and using this value with equation (B12) to obtain

$$\bar{\lambda}_0 = \int_0^{\gamma_0} \frac{\tau(\gamma)}{\sin^2\gamma + 2\bar{p}\cos\gamma}\, d\gamma \tag{B14}$$

This equation is solved for the unknown limit of integration γ_0 by Newton iteration. With γ_0 known, equation (B9) is used to find

$$T_0 = T_1 \frac{\tau_0}{\tau_1} \tag{B15}$$

where $\tau_0 = \tau(\gamma_0)$. From the sketch of appendix B, $d\tilde{x} = d\ell \cos\gamma$. Using equation (B10) in this expression yields

$$d\tilde{x} = \frac{T_1}{n\tau_1}\, d\sigma \tag{B16}$$

where $d\sigma = \dfrac{\tau\cos\gamma}{\sin^2\gamma + 2\bar{p}\cos\gamma}\, d\gamma$. Equation (B16) may be integrated numerically to give

$$\tilde{x}_1 = \frac{T_1}{n\tau_1} \int_{\gamma_0}^{\gamma_1} d\sigma \tag{B17}$$

Finally, from the sketch and equation (B5)

$$d\tilde{z} = d\ell \sin\gamma = \frac{dT}{w_c} \tag{B18}$$

which is integrated to give

$$\tilde{z}_1 = \frac{T_1 - T_0}{w_c} \tag{B19}$$

Cable Force Derivatives

Consider the cable in its equilibrium position. If the upper end is slowly displaced in the $\tilde{X}\tilde{Z}$-plane from its original position $(\tilde{x}_1, \tilde{z}_1)$ to a new position $(\tilde{x}_1 + d\tilde{x},\ \tilde{z}_1 + d\tilde{z})$, the resultant x- and z-force increments are

$$dF_X = k_{xx} d\tilde{x} + k_{xz} d\tilde{z} \tag{B20a}$$

$$dF_Z = k_{zx} d\tilde{x} + k_{zz} d\tilde{z} \tag{B20b}$$

where k_{xx}, k_{xz}, k_{zx}, and k_{zz} are the cable derivatives (spring constants) for the longitudinal case. The derivation of the expressions for these derivatives is given in reference 2. The results for the derivatives are

$$k_{xx} = \frac{1}{\delta}\left[T_1 \cos\gamma_1\left(\sin\gamma_1 - \sin\gamma_0\right) + n\left(z_1 - l\sin\gamma_0\right)\sin^3\gamma_1\right] \tag{B21a}$$

$$k_{xz} = \frac{1}{\delta}\left[T_1 \cos\gamma_1\left(\cos\gamma_0 - \cos\gamma_1\right) + n\left(l\cos\gamma_0 - \tilde{x}_1\right)\sin^3\gamma_1\right] \tag{B21b}$$

$$k_{zx} = \frac{1}{\delta}\left[T_1 \sin\gamma_1\left(\sin\gamma_1 - \sin\gamma_0\right) - \left(w_c + n\sin^2\gamma_1\cos\gamma_1\right)\left(\tilde{z}_1 - l\sin\gamma_0\right)\right] \tag{B21c}$$

$$k_{zz} = \frac{1}{\delta}\left[T_1 \sin\gamma_1\left(\cos\gamma_0 - \cos\gamma_1\right) - \left(w_c + n\sin^2\gamma_1\cos\gamma_1\right)\left(l\cos\gamma_0 - \tilde{x}_1\right)\right] \tag{B21d}$$

where

$$\delta = x_1\left(\sin\gamma_1 - \sin\gamma_0\right) + z_1\left(\cos\gamma_0 - \cos\gamma_1\right) - l\sin\left(\gamma_1 - \gamma_0\right) \tag{B22}$$

These derivatives depend only on quantities which were determined in the first section of this appendix.

The single lateral cable derivative is determined by considering a small force dF_Y to act in the $\tilde{y}$-direction on the upper end of the cable. This will result in a small $\tilde{y}$-deflection according to

$$dF_Y = k_{yy}d\tilde{y} \tag{B23}$$

where k_{yy} is the cable derivative (spring constant) for the lateral case. The expression for this derivative is derived in reference 2 and is

$$k_{yy} = \frac{n\sqrt{\tau_1\left(\sin^2\gamma_1 + 2\bar{p}\cos\gamma_1\right)}}{\int_{\gamma_0}^{\gamma_1}\sqrt{\frac{\tau(\gamma)}{\sin^2\gamma + 2\bar{p}\cos\gamma}}\,d\gamma} \tag{B24}$$

The value of k_{yy} is determined from equation (B24) by numerical integration.

APPENDIX C

TRANSFER OF AERODYNAMIC COEFFICIENTS WITH DISPLACEMENT OF AXIS-SYSTEM ORIGIN

The equations of motion (eqs. (A30)) are written about the balloon center of mass which requires that the aerodynamic coefficients be referenced to this point. As the center of mass may change for various conditions, the aerodynamic coefficients are more conveniently specified about a fixed reference point and transferred to the mass center for each specific case. The following relations are developed for transferring the aerodynamic coefficients from the arbitrary reference point to the center of mass. From figure 4 the geometrical relationships are

$$x_t = l_{cg} \cos \alpha_t + h_{cg} \sin \alpha_t$$

$$z_t = h_{cg} \cos \alpha_t - l_{cg} \sin \alpha_t$$

where x_t and z_t are the distances from the reference point to the center of mass.

This development is given for completeness and to delineate some of the assumptions involved. The quantities pertaining to the reference point are indicated by the subscript R, and quantities pertaining to the center of mass are without subscripts. Only stability derivatives involving rates and displacements are considered. The apparent masses and inertias which involve accelerations are considered with the structural mass and inertias (e.g., eqs. (A10)).

Longitudinal Coefficients

The force and moment coefficients about the center of mass are determined by considering the motion at the reference point resulting from motion about the center of mass and then calculating the resulting forces and moments at the center of mass due to the forces and moments acting at the reference point.

Motion transfer.- The perturbations at the reference point generated by perturbations about the center of mass are

$$\theta_R = \theta \tag{C1a}$$

$$\dot{\theta}_R = \dot{\theta} \tag{C1b}$$

$$\ddot{\theta}_R = \ddot{\theta} \tag{C1c}$$

$$\dot{z}'_R = \dot{z}' + x_t\dot{\theta} \tag{C1d}$$

$$\ddot{z}'_R = \ddot{z}' + x_t\ddot{\theta} \tag{C1e}$$

$$\dot{x}'_R = \dot{x}' - z_t\dot{\theta} \tag{C1f}$$

$$\alpha_R = \theta + \frac{\dot{z}' + x_t\dot{\theta}}{V_\infty} \tag{C1g}$$

$$\dot{\alpha}_R = \dot{\theta} + \frac{\ddot{z}' + x_t\ddot{\theta}}{V_\infty} \tag{C1h}$$

Force and moment transfer.- The forces and moments at the center of mass in terms of those at the reference point are

$$F_Z = F_{Z,R} \tag{C2a}$$

$$F_X = F_{X,R} \tag{C2b}$$

$$M_Y = M_{Y,R} - z_t M_{Z,R} + x_t M_{Z,R} \tag{C2c}$$

Coefficients of lift.- For use in the z-equation the coefficients for

$$\left(F_{Z,A}\right)_R = -\left(L + D\alpha_R\right) \tag{C3}$$

are needed. The procedure followed is: first, write equation (A17c) about the reference point; then, substitute equations (C1) into the results; and finally, use the results of the substitution in equations (C2a) and (C3). Neglecting higher order terms, the resulting equation is equivalent to equation (A17c) but contains only independent variables pertaining to the center of mass and coefficients pertaining to the reference point. By equating coefficients of the independent variables of the resulting expression to the corresponding ones of equation (A17c) and by evaluating the results at the trim condition, the following transfer relations result:

$$C_{L_\alpha} = C_{L_{\alpha,R}} \tag{C4a}$$

$$C_{L_{\dot{\alpha}}} = C_{L_{\dot{\alpha},R}} \tag{C4b}$$

$$C_{L_u} = C_{L_{u,R}} \tag{C4c}$$

$$C_{L_q} = C_{L_{q,R}} + \frac{2x_t}{\bar{c}} C_{L_\alpha} - \frac{2z_t}{\bar{c}}\left(2C_L + C_{L_u}\right) \tag{C4d}$$

Thus, the only term affected by the transfer is C_{L_q}.

Coefficients of drag.- For use in the x-equation the coefficients for

$$\left(F_{X,A}\right)_R = L\alpha_R - D \tag{C5}$$

are needed. Using equations (C1), (C2b), (C5), and (A17a) gives

$$C_D = C_{D,R} \tag{C6a}$$

$$C_{D_\alpha} = C_{D_{\alpha,R}} \tag{C6b}$$

$$C_{D_u} = C_{D_{u,R}} \tag{C6c}$$

Thus, the aerodynamic drag coefficients are unaffected by equations (C6).

Coefficients of pitching moment.- Using equations (C1), (C2c), and (A17e) gives

$$C_m = C_{m,R} + \frac{z_t}{\bar{c}} C_D - \frac{x_t}{\bar{c}} C_L \tag{C7a}$$

$$C_{m_u} = C_{m_{u,R}} + \frac{z_t}{\bar{c}} C_{D_u} - \frac{x_t}{\bar{c}} C_{L_u} \tag{C7b}$$

$$C_{m_\alpha} = C_{m_{\alpha,R}} - \frac{z_t}{\bar{c}}\left(C_L - C_{D_\alpha}\right) - \frac{x_t}{\bar{c}}\left(C_{L_\alpha} + C_D\right) \tag{C7c}$$

$$C_{m_{\dot{\alpha}}} = C_{m_{\dot{\alpha},R}} - \frac{x_t}{\bar{c}} C_{L_{\dot{\alpha}}} \tag{C7d}$$

$$C_{m_q} = C_{m_{q,R}} - \frac{x_t}{\bar{c}}\left(C_{L_{q,R}} - 2C_{m_\alpha}\right) - \frac{2z_t}{\bar{c}}\left(2C_m + C_{m_u}\right) \tag{C7e}$$

where terms such as C_{X_q} are neglected.

Lateral Coefficients

Motion transfer.- For lateral perturbations about the center of mass, the corresponding perturbations at the reference point are

$$\dot{y}'_R = \dot{y}' + z_t\dot{\phi} - x_t\dot{\psi} \tag{C8a}$$

$$\phi_R = \phi \tag{C8b}$$

$$\dot{\phi}_R = \dot{\phi} \tag{C8c}$$

$$\psi_R = \psi \tag{C8d}$$

$$\dot{\psi}_R = \dot{\psi} \tag{C8e}$$

$$\beta_R = -\psi + \frac{\dot{y}'}{V_\infty} + \frac{z_t\dot{\phi}}{V_\infty} - \frac{x_t\dot{\psi}}{V_\infty} \tag{C8f}$$

$$\dot{\beta}_R = -\dot{\psi} + \frac{\ddot{y}'}{V_\infty} + \frac{z_t\ddot{\phi}}{V_\infty} - \frac{x_t\ddot{\psi}}{V_\infty} \tag{C8g}$$

Force and moment transfer.- The forces and moments at the center of mass in terms of those at the reference point are

$$F_Y = F_{Y,R} \tag{C9a}$$

$$M_Z = M_{Z,R} - x_t F_{Y,R} \tag{C9b}$$

$$M_X = M_{X,R} + z_t F_{Y,R} \tag{C9c}$$

Coefficients of y-force.- Using equations (C8), (C9a), and (A17b) gives

$$C_{Y_\beta} = C_{Y_{\beta,R}} \tag{C10a}$$

$$C_{Y_{\dot{\beta}}} = C_{Y_{\dot{\beta},R}} \tag{C10b}$$

$$C_{Y_r} = C_{Y_{r,R}} - \frac{2x_t}{\bar{c}} C_{Y_\beta} \tag{C10c}$$

$$C_{Y_p} = C_{Y_{p,R}} + \frac{2z_t}{\bar{c}} C_{Y_\beta} \tag{C10d}$$

Thus, only C_{Y_p} and C_{Y_r} are affected by the transfer equations (C10).

Coefficients of yawing moment.- Using equations (C8), (C9b), and (A17f) gives

$$C_{n_\beta} = C_{n_{\beta,R}} - \frac{x_t}{\bar{c}} C_{Y_\beta} \tag{C11a}$$

$$C_{n_{\dot\beta}} = C_{n_{\dot\beta,R}} - \frac{x_t}{\bar{c}} C_{Y_{\dot\beta}} \tag{C11b}$$

$$C_{n_r} = C_{n_{r,R}} - \frac{x_t}{\bar{c}}\left(C_{Y_{r,R}} + 2C_{n_\beta}\right) \tag{C11c}$$

$$C_{n_p} = C_{n_{p,R}} - \frac{x_t}{\bar{c}} C_{Y_{p,R}} + \frac{2z_t}{\bar{c}} C_{n_\beta} \tag{C11d}$$

In the development of equations (C11) the transfers involving $C_{n_{\dot\beta}}$ are neglected except for $C_{n_{\dot\beta}}$ itself.

Coefficients of rolling moment.- Using equations (C8), (C9c), and (A17d) gives

$$C_{l_\beta} = C_{l_{\beta,R}} + \frac{z_t}{\bar{c}} C_{Y_\beta} \tag{C12a}$$

$$C_{l_{\dot\beta}} = C_{l_{\dot\beta,R}} + \frac{z_t}{\bar{c}} C_{Y_{\dot\beta}} \tag{C12b}$$

$$C_{l_p} = C_{l_{p,R}} + \frac{z_t}{\bar{c}}\left(C_{Y_{p,R}} + 2C_{l_\beta}\right) \tag{C12c}$$

$$C_{l_r} = C_{l_{r,R}} + \frac{z_t}{\bar{c}} C_{Y_{r,R}} - \frac{2x_t}{\bar{c}} C_{l_\beta} \tag{C12d}$$

In the development of equations (C12) the transfers involving $C_{l_{\dot\beta}}$ are neglected except for $C_{l_{\dot\beta}}$ itself.

REFERENCES

1. Bairstow, L.; Relf, E. F.; and Jones, R.: The Stability of Kite Balloons: Mathematical Investigation. R. & M. No. 208, Brit. A.R.C., 1915.

2. Neumark, S.: Equilibrium Configurations of Flying Cables of Captive Balloons, and Cable Derivatives for Stability Calculations. R. & M. No. 3333, Brit. A.R.C., 1963.

3. DeLaurier, James D.: A Stability Analysis of Cable-Body Systems Totally Immersed in a Fluid Stream. NASA CR-2021, 1972.

4. DeLaurier, James D.: A First Order Theory for Predicting the Stability of Cable Towed and Tethered Bodies Where the Cable Has a General Curvature and Tension Variation. VKI-TN-68, Von Karman Inst. Fluid Dyn., Dec. 1970.

5. Redd, L. Tracy: A Towing Technique for Determining the Aerodynamic Forces on Tethered Balloons. Paper presented at the Sixth Air Force Cambridge Research Laboratories Scientific Balloon Symposium (Portsmouth, N.H.), June 1970.

6. Redd, L. Tracy; Bennett, Robert M.; and Bland, Samuel R.: Experimental and Analytical Determination of Stability Parameters for a Balloon Tethered in a Wind. NASA TN D-7222, 1973.

7. Bennett, Robert M.; Bland, Samuel R.; and Redd, L. Tracy: Computer Programs for Calculating and Plotting the Stability Characteristics of a Balloon Tethered in a Wind. NASA TM X-2740, 1973.

8. Redd, L. Tracy; Bennett, Robert M.; and Bland, Samuel R.: Analytical and Experimental Investigation of the Stability of a Balloon Tethered in a Wind. Paper presented at the Seventh Air Force Cambridge Research Laboratories Scientific Balloon Symposium (Portsmouth, N.H.), Sept. 1972.

9. Etkin, Bernard: Dynamics of Flight. John Wiley & Sons, Inc., c.1959.

10. Etkin, Bernard; and Mackworth, Jean C.: Aerodynamic Instability of Non-Lifting Bodies Towed Beneath an Aircraft. UTIA Tech. Note No. 65, Inst. Aerophys., Univ. of Toronto, Jan. 1963.

11. DeLaurier, James D.: A Stability Analysis for Tethered Aerodynamically Shaped Balloons. J. Aircraft, vol. 9, no. 9, Sept. 1972, pp. 646-651.

12. Vorachek, Jerome J.; Burbick, James W.; and Doyle, George R., Jr.: Investigation of Dynamic Behavior of Tethered Balloon Systems. AFCRL-72-0113, U.S. Air Force, 1972.

13. Zahm, A. F.; Smith, R. H.; and Louden, F. A.: Drag of C-Class Airship Hulls of Various Fineness Ratios. NACA Rep. 291, 1928.

14. Landweber, L.; and Winzer, A.: A Comparison of the Added Masses of Streamlined Bodies and Prolate Spheroids. Rep. No. 572 (Contract No. N6onr-24705), Stevens Inst. Technol., June 1955.

TABLE I - PROPERTIES OF 7 64-METER BALLOON IN REFERENCE CONFIGURATION

[See fig 4]

Aerostatic properties	
Distance from balloon nose to reference point, a, m	4 72
Atmospheric density, ρ, kg/m^3	1 225
Component of distance from reference point to bridle confluence point, l_{tr}, m	3 44
Component of distance from reference point to bridle confluence point, t_{tr}, m	3 82
Buoyancy force, B, N	190
Component of distance from reference point to center of buoyancy, l_{br}, m	2 15
Component of distance from reference point to center of buoyancy, h_{br}, m	0
Reference area, S, m^2	7 04
Reference length, $\bar{c}$, m	7 64
Component of distance from reference point to center of mass of balloon structure, l_{sr}, m	-0 66
Component of distance from reference point to center of mass of balloon structure, h_{sr}, m	0 38
Structural weight, W_s, N	108
Volume, V_b, m^3	19 0
Dynamic masses and moments of inertia	
Apparent air mass at $(\alpha_t = 0)$, $m_{x,a}$, kg	5 11
Apparent air mass at $(\alpha_t = 0)$, $m_{y,a}$, kg	23 9
Apparent air mass at $(\alpha_t = 0)$, $m_{z,a}$, kg	23 9
Component of distance from reference point to center of mass (includes apparent mass), l_{cg}, m	1 10
Component of distance from reference point to center of mass (includes apparent mass), h_{cg}, m	0 11
Mass of balloon structure and inflation gas m_T kg	14 2
Rolling moment of inertia (at $\alpha_t = 0$), I_{xx}, kg-m^2	16 1
Pitching moment of inertia, I_{yy}, kg-m^2	171
Yawing moment of inertia (at $\alpha_t = 0$), I_{zz}, kg-m^2	164
Tether-cable parameters	
Diameter, d_c, m	0 0141
Length, l, m	61 0
Weight per unit length, w_c, N/m	0 343
Normal drag coefficient, C_{D_c}	1 17

Aerodynamic derivatives (specified about force reference point)

$C_L = 0\ 82(\alpha_t - 0\ 023) - 5\ 02(\alpha_t - 0\ 023)^3 + 111\ 4(\alpha_t - 0\ 023)^5$

$C_{L_\alpha} = 0\ 82 - 15\ 06(\alpha_t - 0\ 023)^2 + 557\ 0(\alpha_t - 0\ 023)^4$

$C_{L_{\dot{\alpha}}} = 0\ 089$

$C_{L_{q,R}} = 0\ 685$

$C_{L_u} = 0$

$C_D = 0\ 0487 + 186\ 2(\alpha_t - 0\ 023)^6$

$C_{D_\alpha} = 1117\ 2(\alpha_t - 0\ 023)^5$

$C_{D_u} = 0$

$C_{m,R} = -0\ 0106 + 0\ 1435\ \alpha_t$

$C_{m_{\alpha,R}} = 0\ 1435$

$C_{m_{\dot{\alpha},R}} = -0\ 026$

$C_{m_{q,R}} = -0\ 189$

$C_{m_{u,R}} = 0$

$C_{Y_\beta} = -0\ 82$

$C_{Y_{\dot{\beta}}} = -0\ 089$

$C_{Y_{p,R}} = 0\ 494 \sin \alpha_t$

$C_{Y_{r,R}} = 0\ 685$

$C_{l_{\beta,R}} = -0\ 1435 \sin \alpha_t$

$C_{l_{\dot{\beta},R}} = 0$

$C_{l_{p,R}} = -0\ 0237$

$C_{l_{r,R}} = -0\ 178 \sin \alpha_t$

$C_{n_{\beta,R}} = -0\ 1435$

$C_{n_{\dot{\beta},R}} = 0\ 026$

$C_{n_{p,R}} = -0\ 0641 \sin 2\alpha_t$

$C_{n_{r,R}} = -0\ 189$

TABLE II.- TOW TESTS AND TEST VARIABLES

Test	Average tow velocity, V_∞, m/sec	Average trim angle, α_t, deg	l_{tr}, m	Cable length, l, m	Cable weight, w_c, N/m	Cable diameter, d_c, m	Purpose of test
10	11.6	5.2	3.44	4.7	0.343	0.0141	Determine frequency and damping of balloon modes of motion
11	12.0	2.5	3.44	30.5	.343	.0141	
[a] 12	12.4	1.5	3.44	61.0	.343	.0141	
13	11.8	2.2	3.44	30.5	1.292	0.0189	Determine effect of cable weight and diameter on balloon stability
14	14.0	2.7	3.44	30.5	1.948	.0205	
[a] 15	26.6	4.7	3.44	61.0	0.343	0.0141	Determine stability boundaries
16	4.0	19.5	1.27	61.0	.343	.0141	
17	25.1	1.2	4.64	61.0	.343	.0141	
18	28.1	5.3	3.44	30.5	1.948	.0205	

[a] Tests 12 and 15 are for balloon reference configuration.

TABLE III.- PARAMETERS CONSIDERED IN LONGITUDINAL-STABILITY TREND STUDY (FIGS. 14 TO 27)

	Figure
m_T	14
I_{yy}	15
l_{cg}	16(a)
h_{cg}	16(b)
$m_{x,a}$	17(a)
$m_{z,a}$	17(b)
B	18(a)
l_{br}	18(b)
l	19(a)
l, x_1, and z_1	19(b)
l_{tr}	20(a)
l_{tr} and α_t	20(b)
d_c	21(a)
d_c and x_1	21(b)
d_c and z_1	21(c)
w_c	22
k_{xx}	23(a)
k_{xz}	23(b)
k_{zx}	23(c)
k_{zz}	23(d)
ΔC_D	24(a)
ΔC_L	24(b)
ΔC_m	24(c)
ΔC_{L_α}	25(a)
ΔC_{m_α}	25(b)
$C_{m_{\dot{\alpha},R}}$	26
$C_{m_{q,R}}$	27

TABLE IV.- LIST OF PARAMETERS CONSIDERED IN LATERAL-STABILITY TREND STUDY (FIGS. 36 TO 44)

	Figure
I_{zz}	36
l_{cg}	37
$m_{y,a}$	38
B	39(a)
l_{br}	39(b)
l	40
ΔC_D	41(a)
ΔC_L	41(b)
ΔC_{Y_β}	42
ΔC_{n_β}	43
ΔC_{n_r}	44

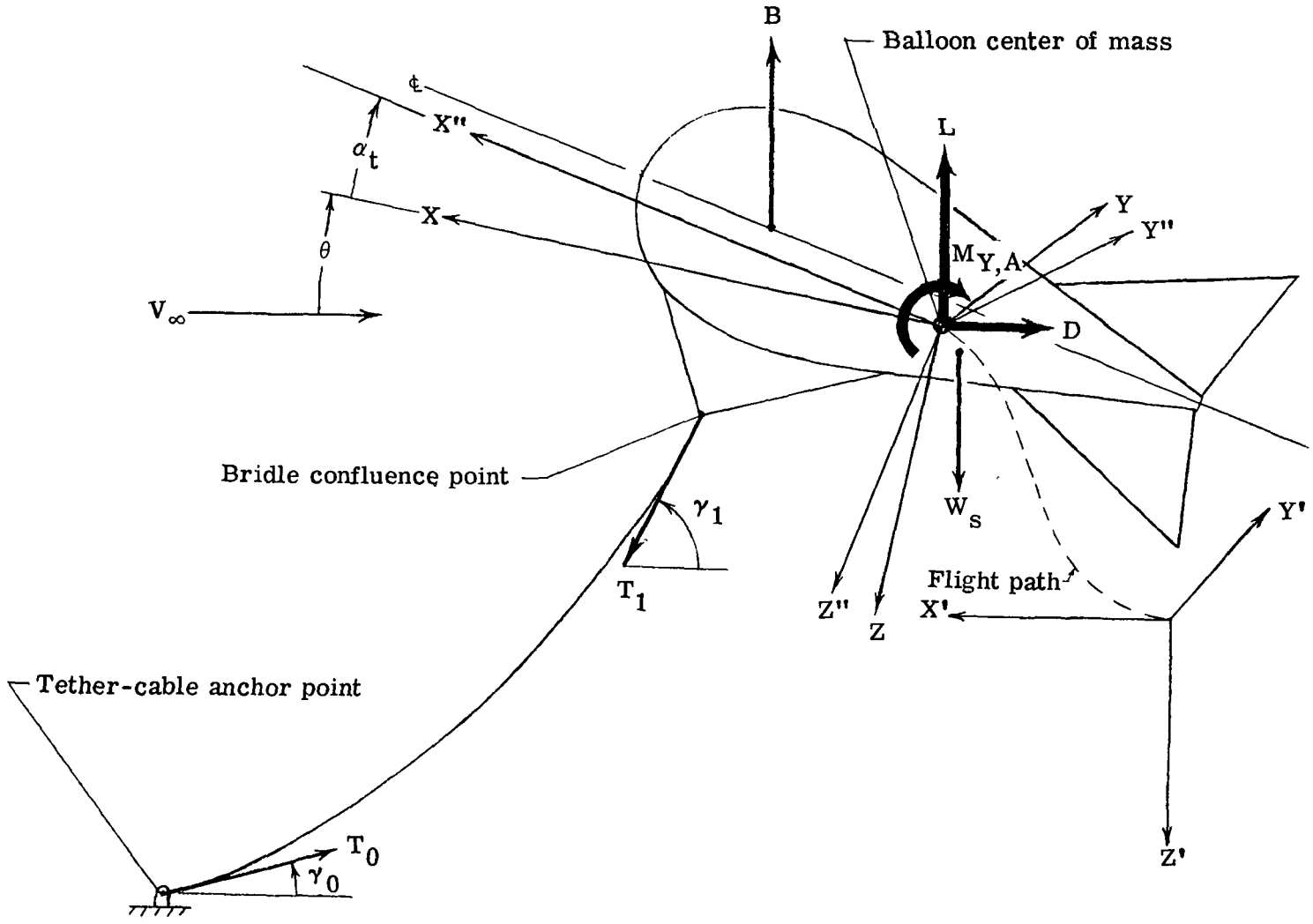

Figure 1.- Tethered-balloon coordinate systems and forces considered in stability analysis.

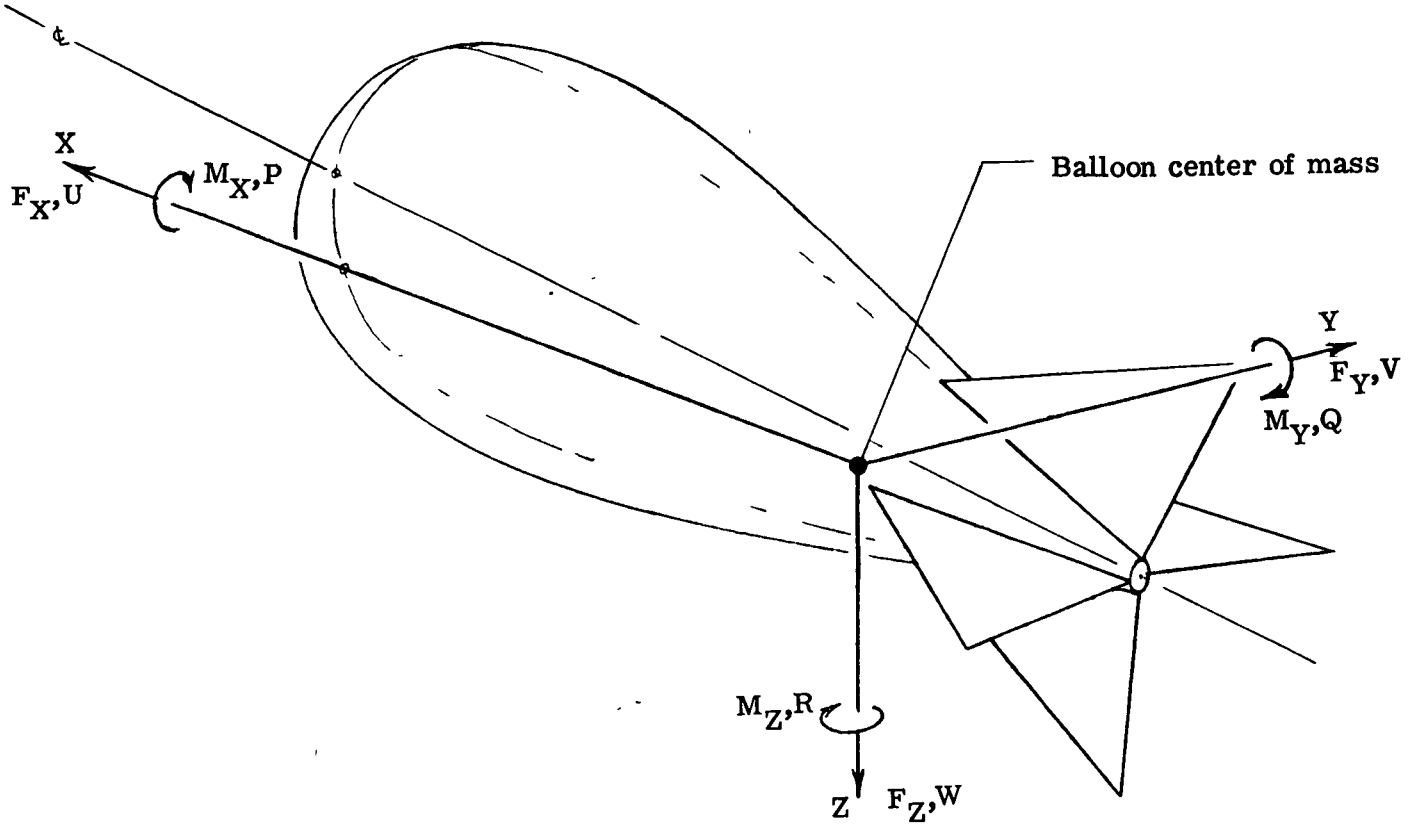

Figure 2.- Stability axis system.

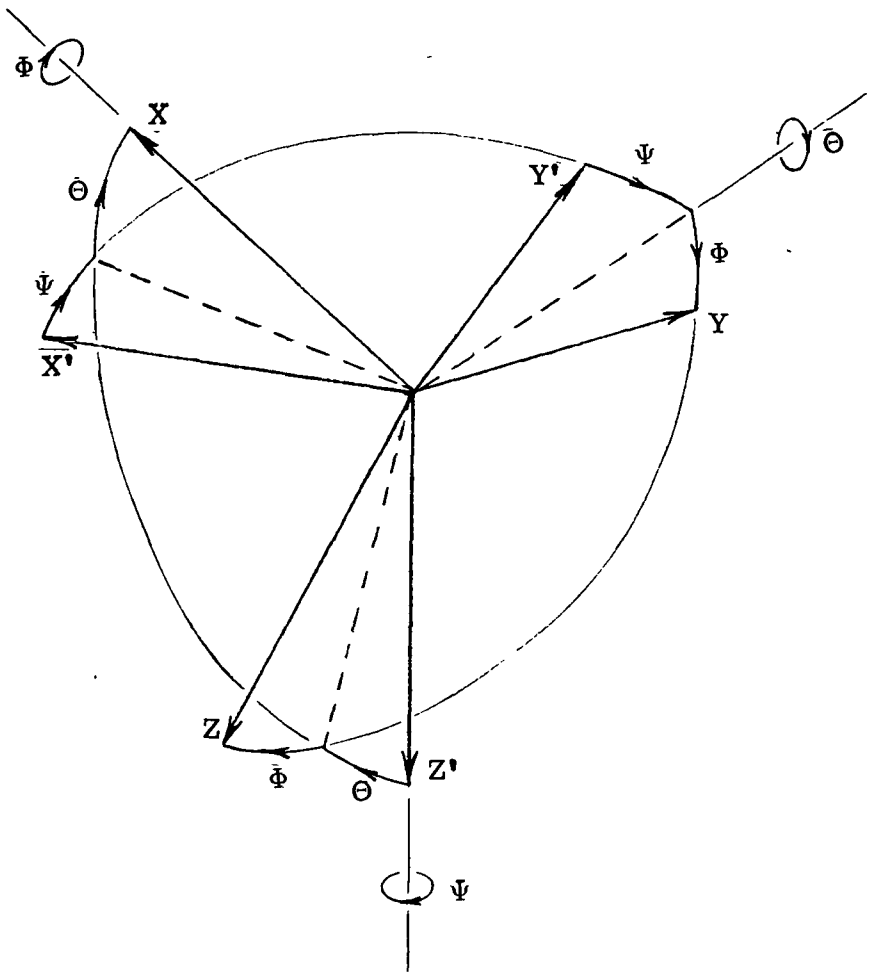

Figure 3.- Orientation of stability axis system.

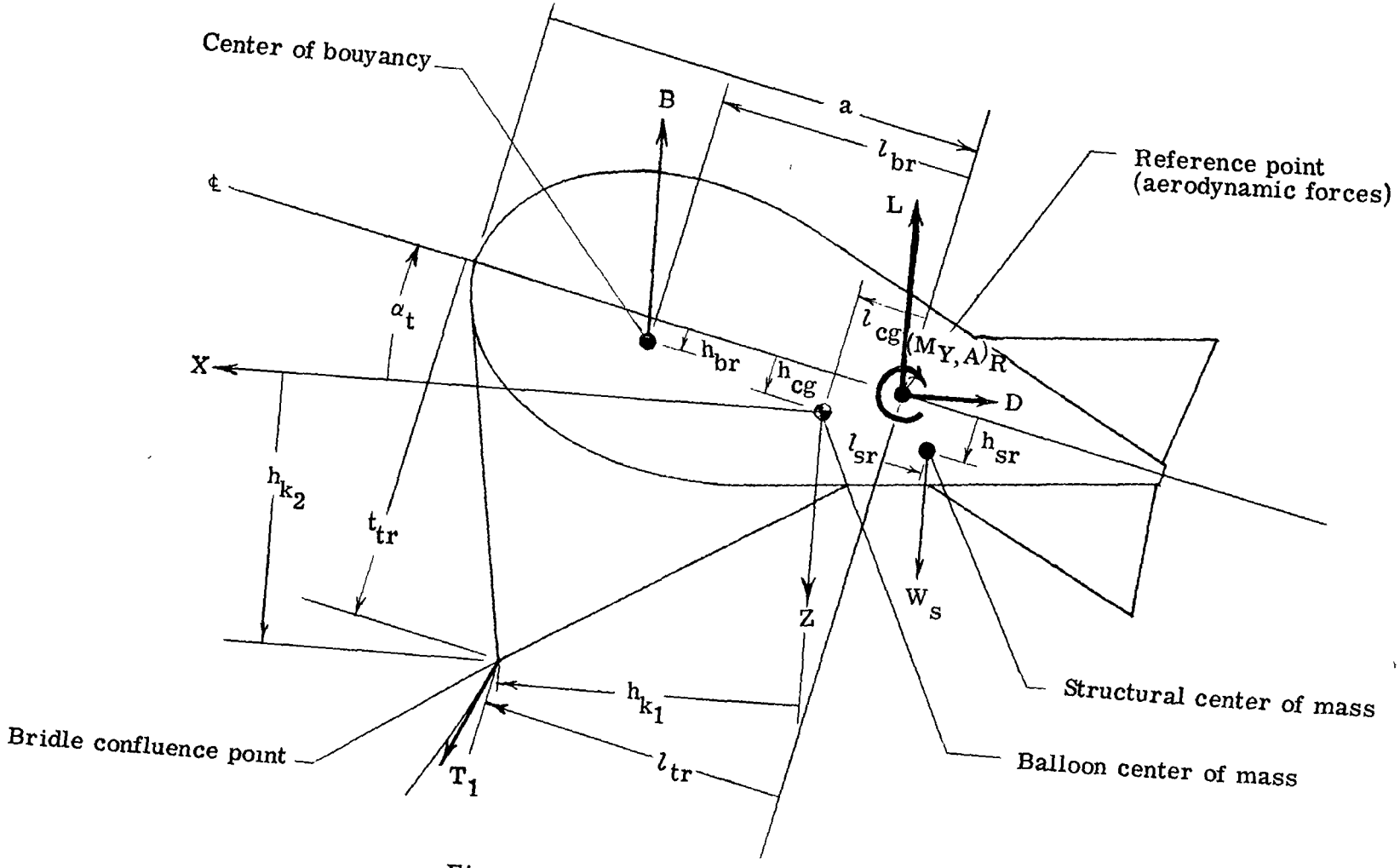

Figure 4.- Geometry of balloon system.

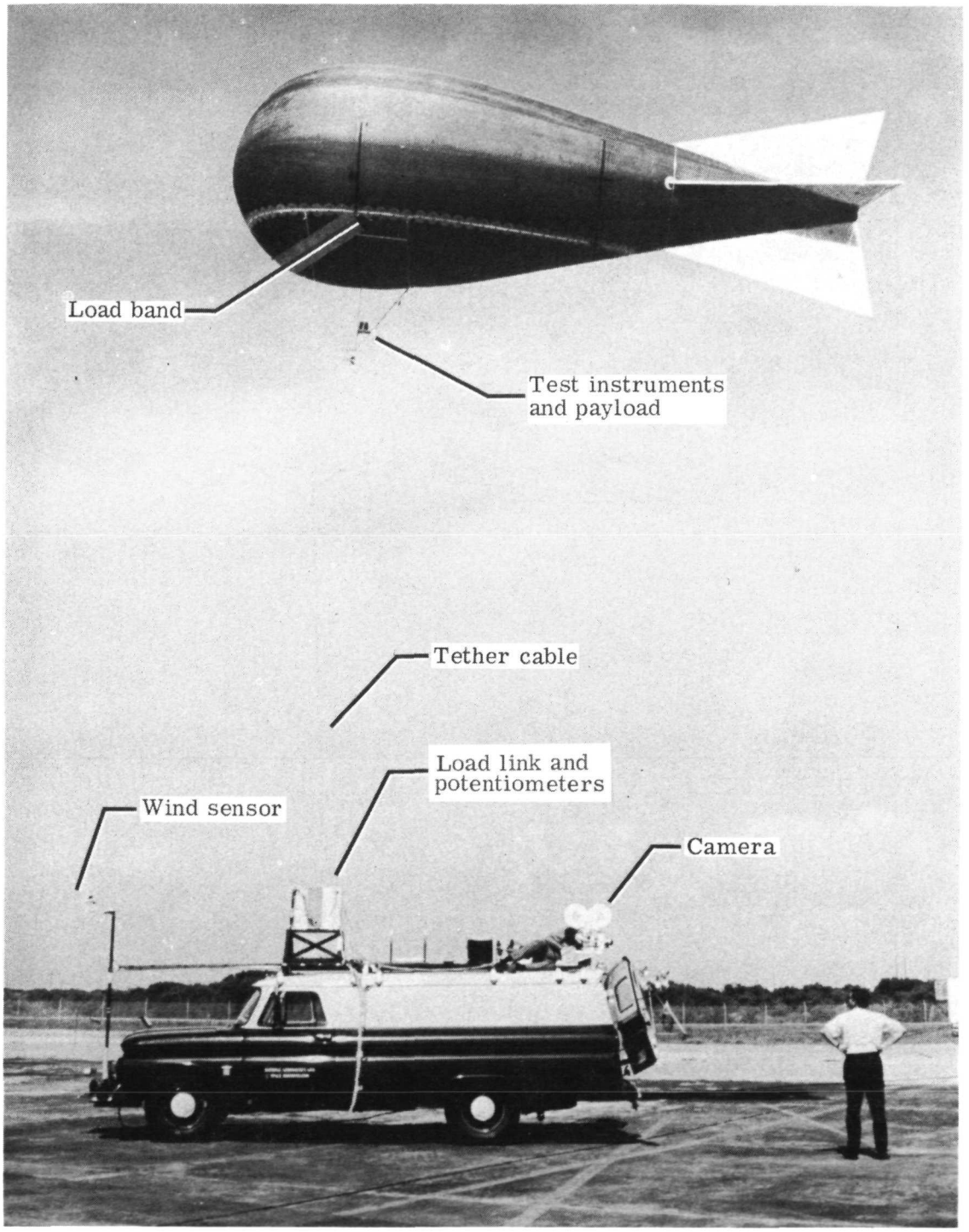

L-73-3074

Figure 5.- Test balloon and tow truck.

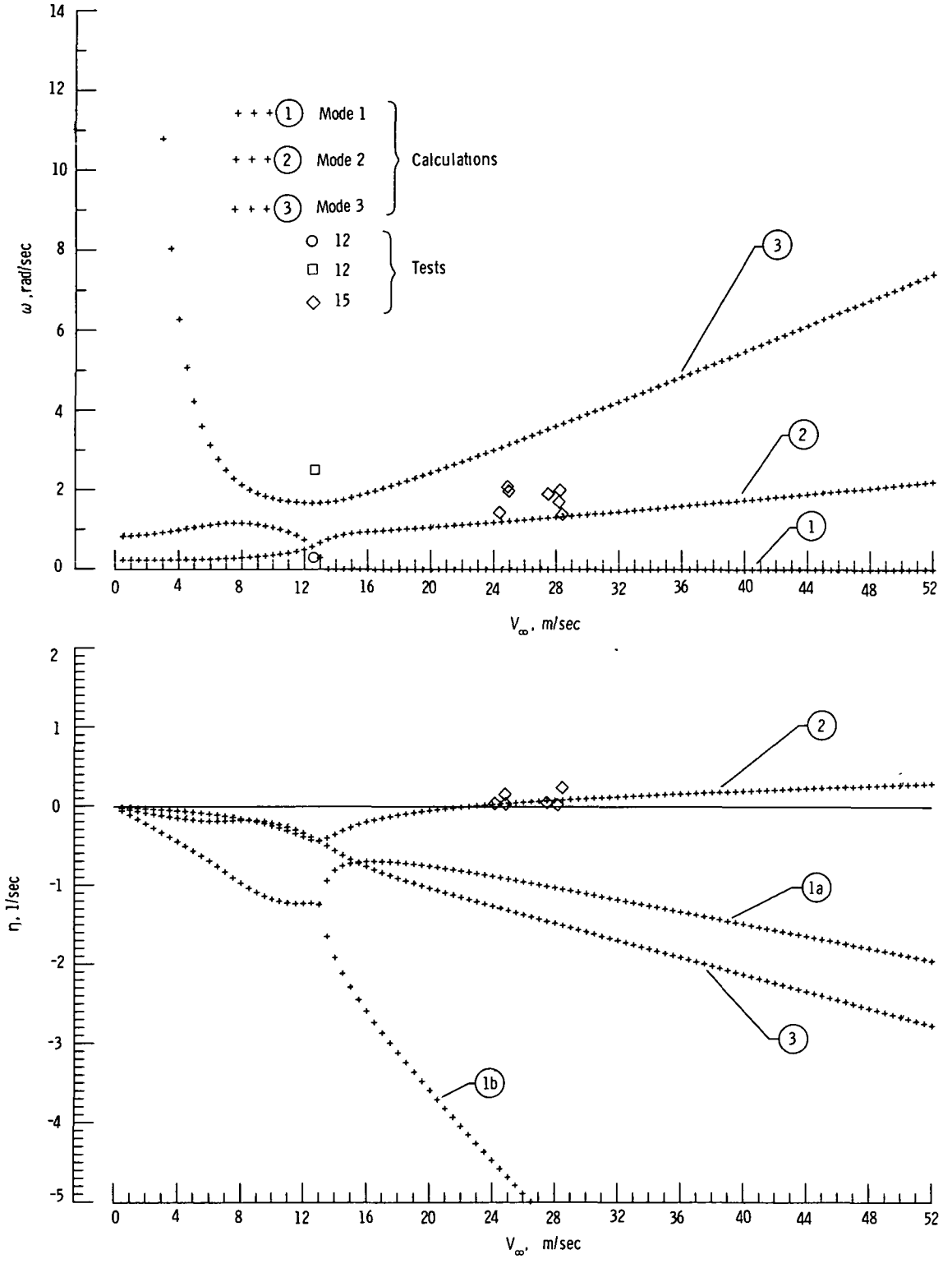

(a) ω and η versus V_∞.

Figure 6.- Variation of longitudinal stability characteristics with velocity for reference configuration (tests 12 and 15).

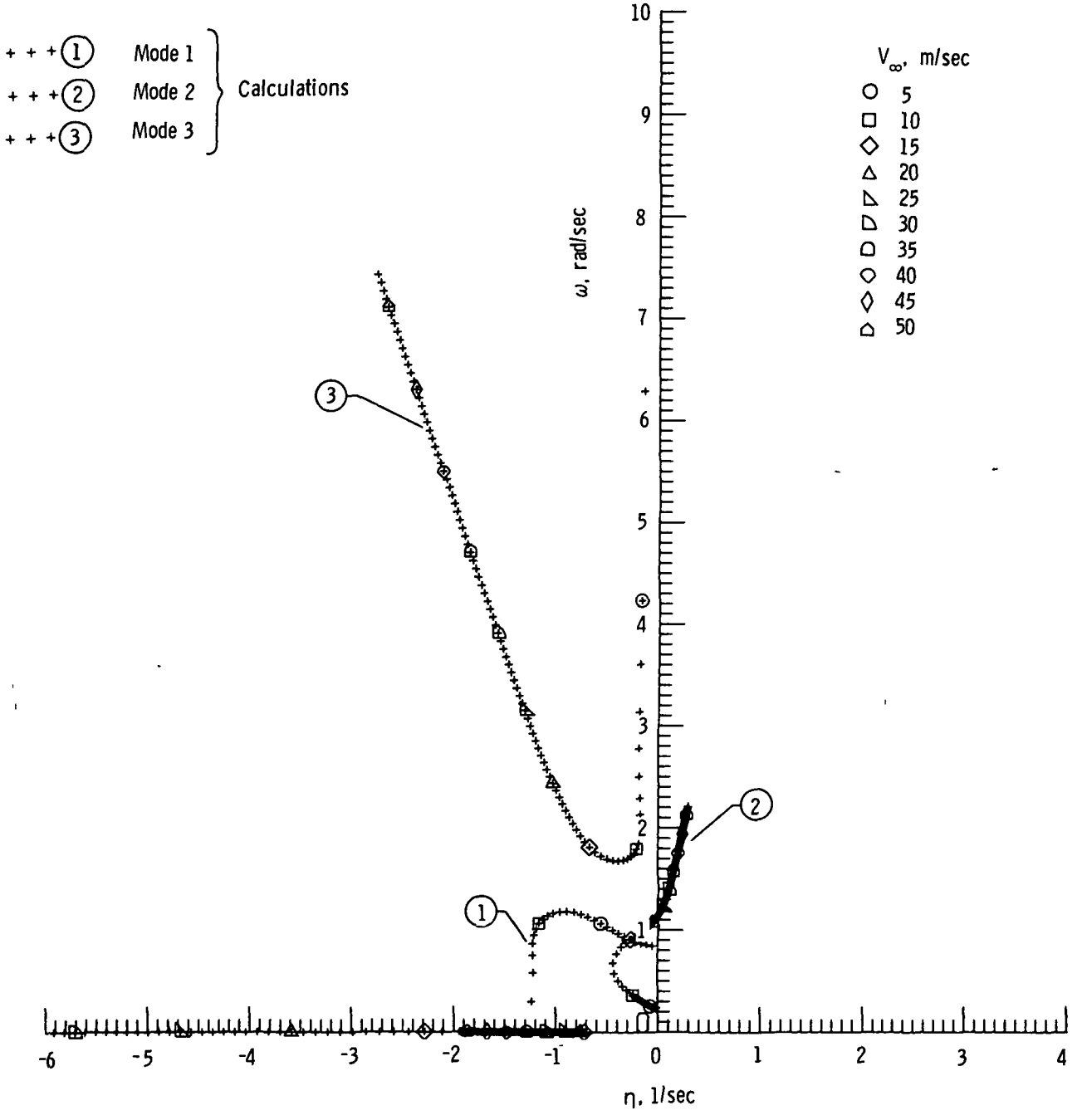

(b) Root locus plot with velocity as a parameter.

Figure 6.- Concluded.

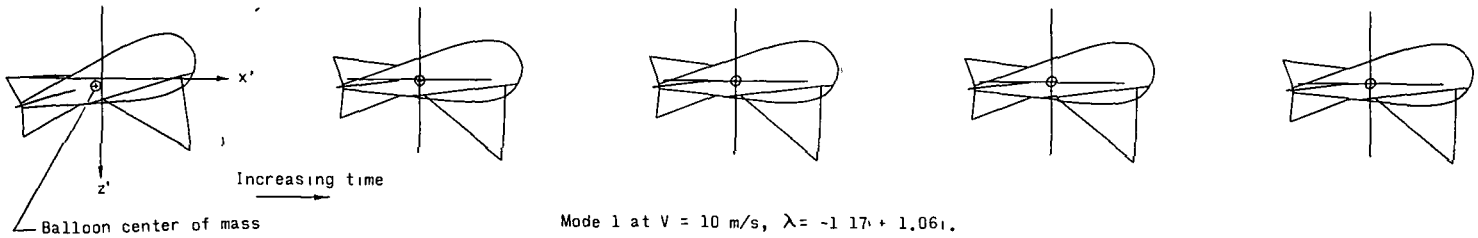

Mode 1 at V = 10 m/s, λ= -1 17 + 1.06i.

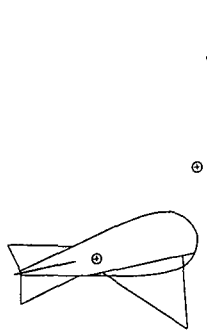

Mode 1a at V = 20 m/s, λ= -.763

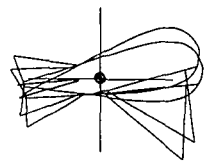

Mode 1b at V = 20 m/s, λ= -3.59.

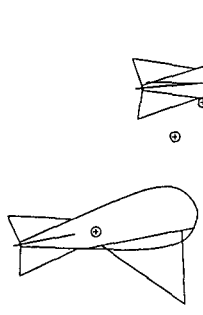

Mode 1a at V = 30 m/s, λ= -1 10.

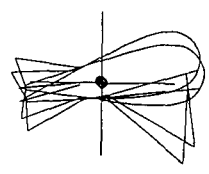

Mode 1b at V = 30 m/s, λ= -5.71.

(a) Mode 1.

Figure 7.- Longitudinal modes of motion for reference configuration. (One cycle of motion is shown for each velocity indicated.)

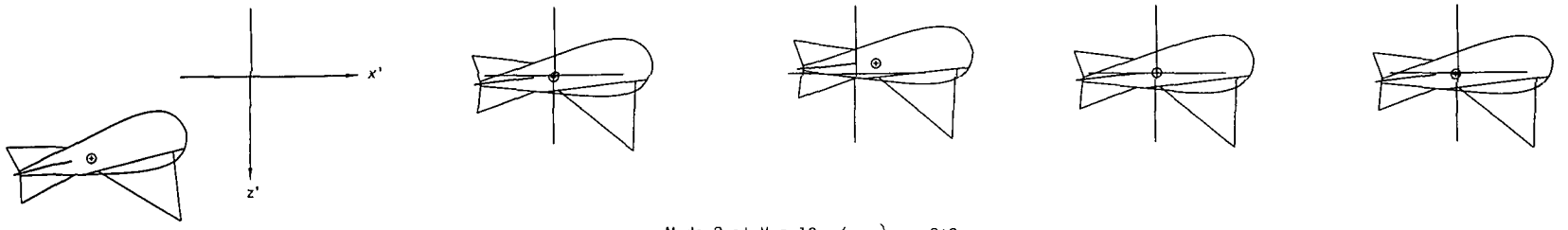

Mode 2 at V = 10 m/s, $\lambda = -.242 + .366i$.

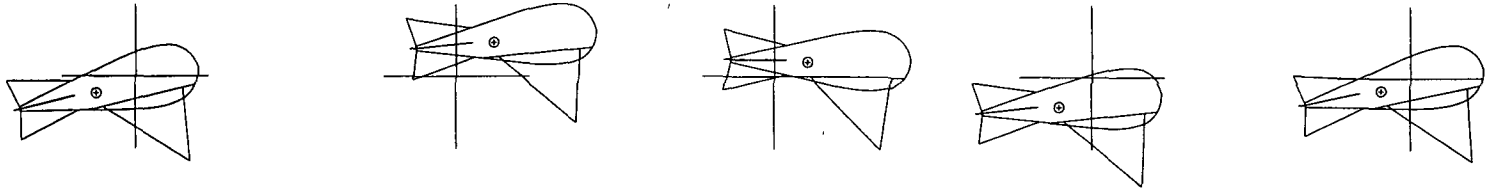

Mode 2 at V = 20 m/s, $\lambda = -.050 + 1.071i$.

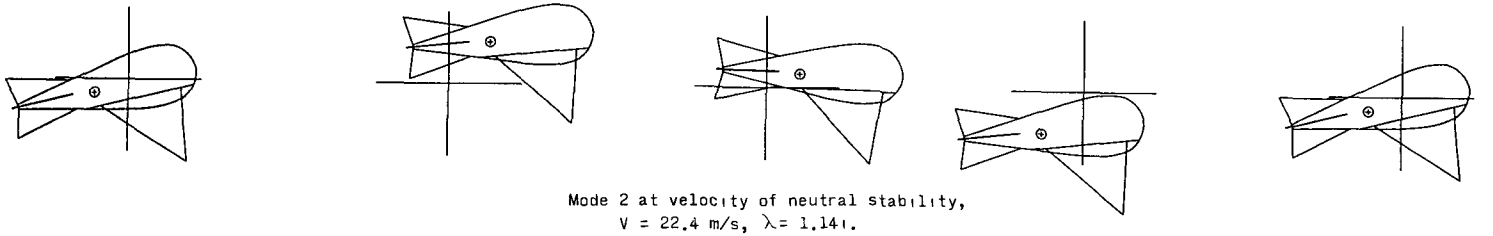

Mode 2 at velocity of neutral stability,
V = 22.4 m/s, $\lambda = 1.141i$.

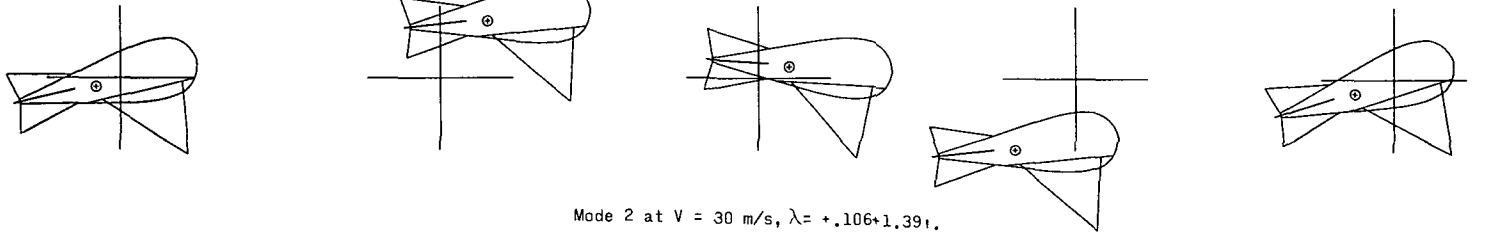

Mode 2 at V = 30 m/s, $\lambda = +.106+1.391i$.

(b) Mode 2.

Figure 7.- Continued.

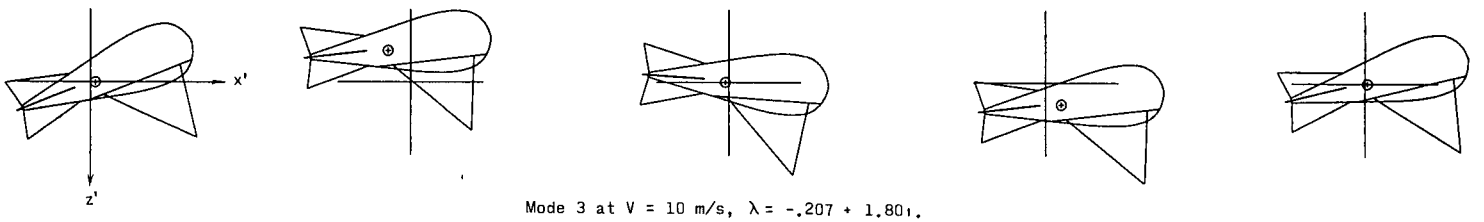

Mode 3 at V = 10 m/s, $\lambda = -.207 + 1.80i$.

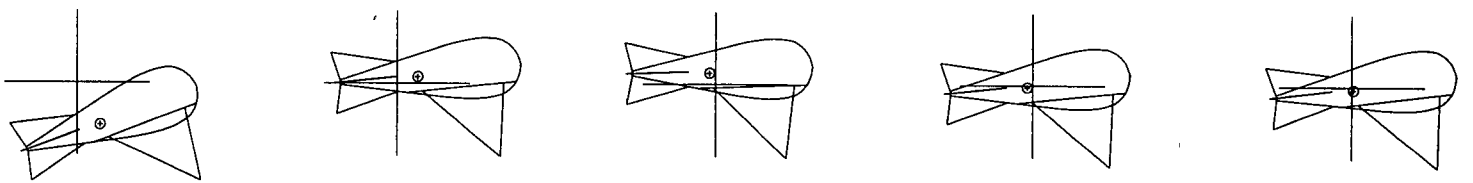

Mode 3 at V = 20 m/s, $\lambda = -1.03 + 2.44i$.

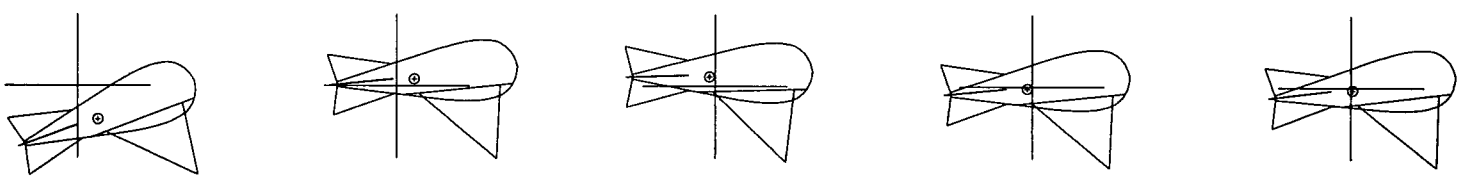

Mode 3 at V = 30 m/s, $\lambda = -1.58 + 3.91i$.

(c) Mode 3.

Figure 7.- Concluded.

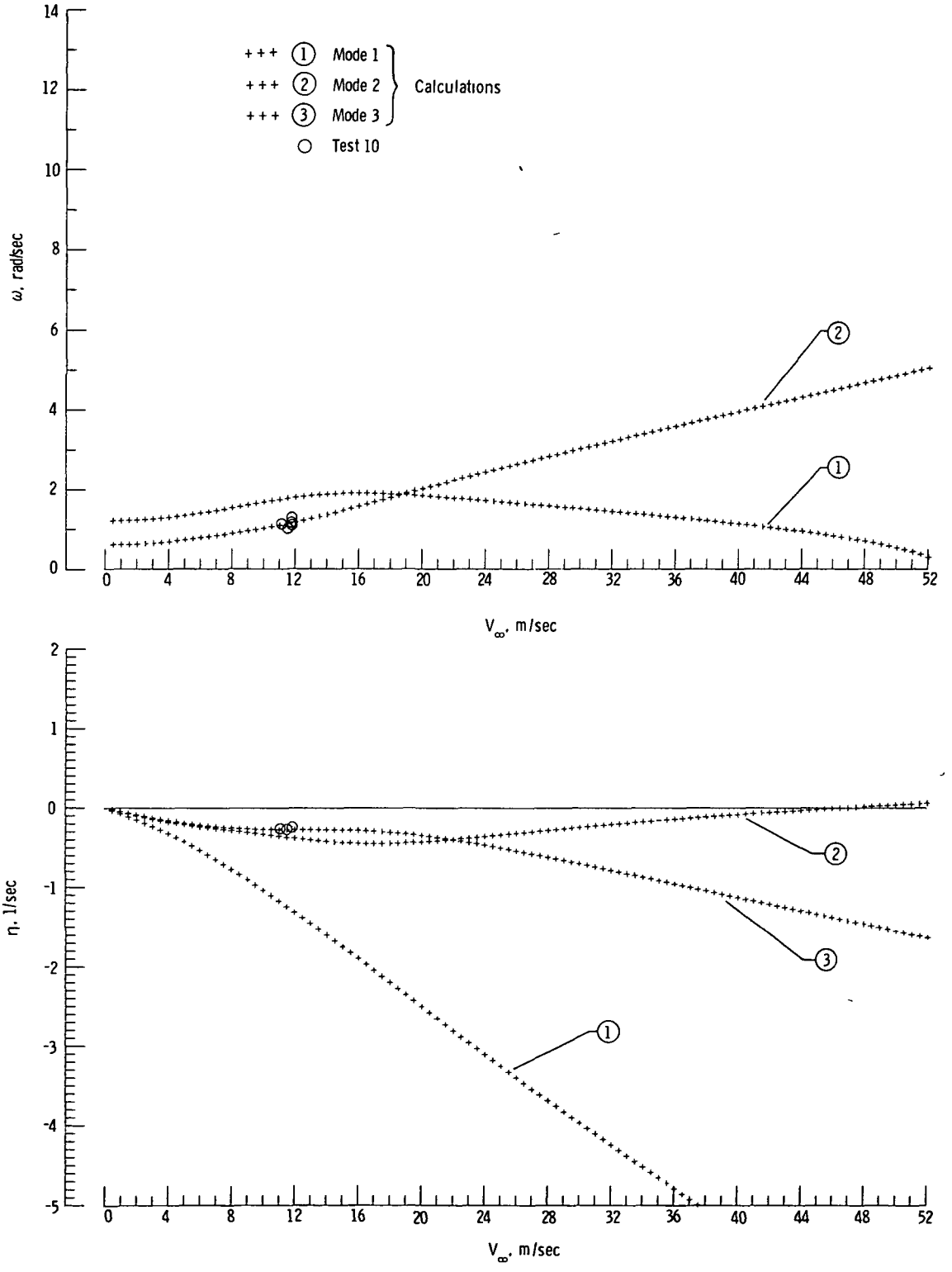

Figure 8.- Variation of longitudinal stability characteristics ω and η with V_∞ for configuration of test 10.

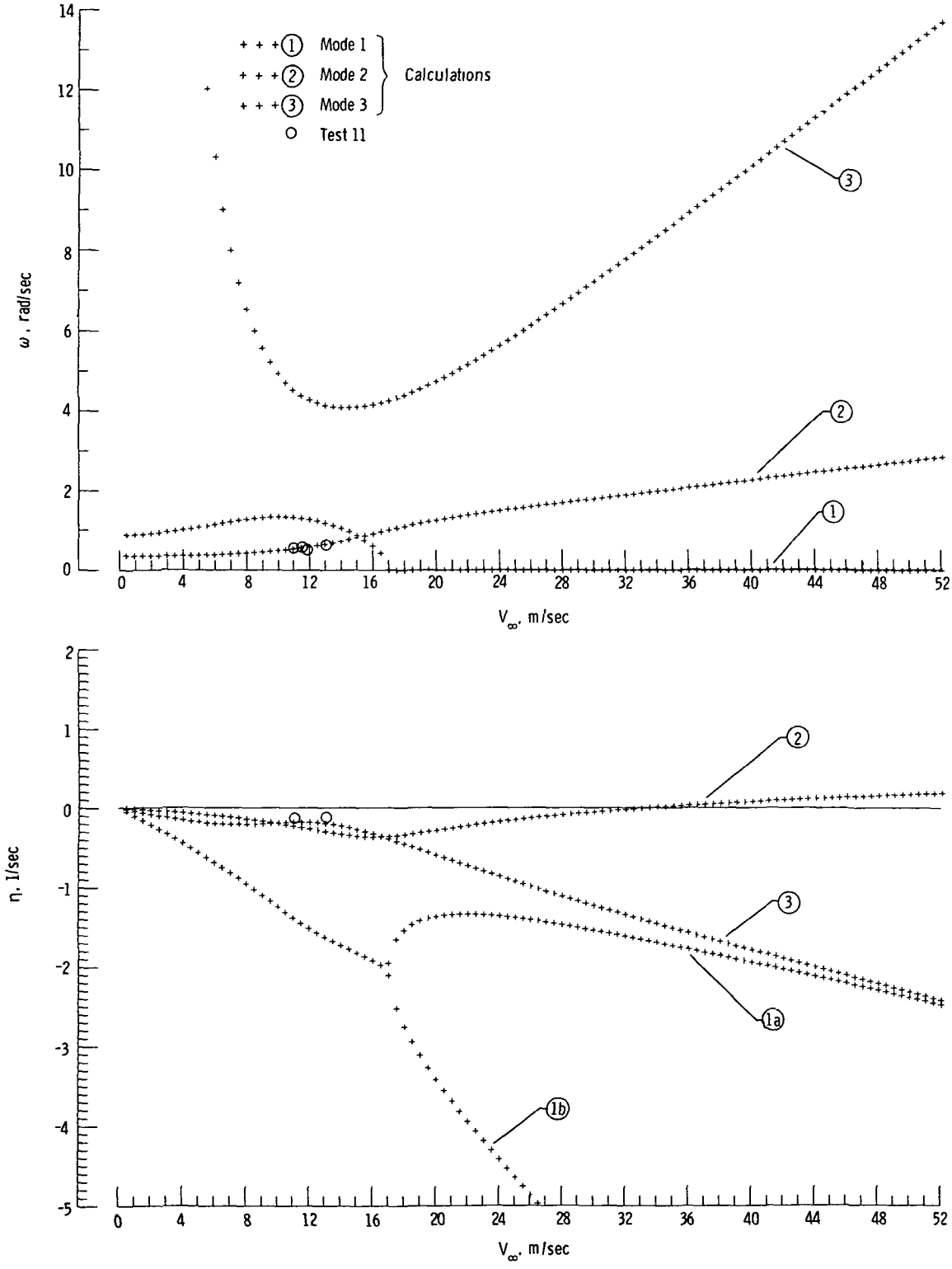

Figure 9.- Variation of longitudinal stability characteristics ω and η with V_∞ for configuration of test 11.

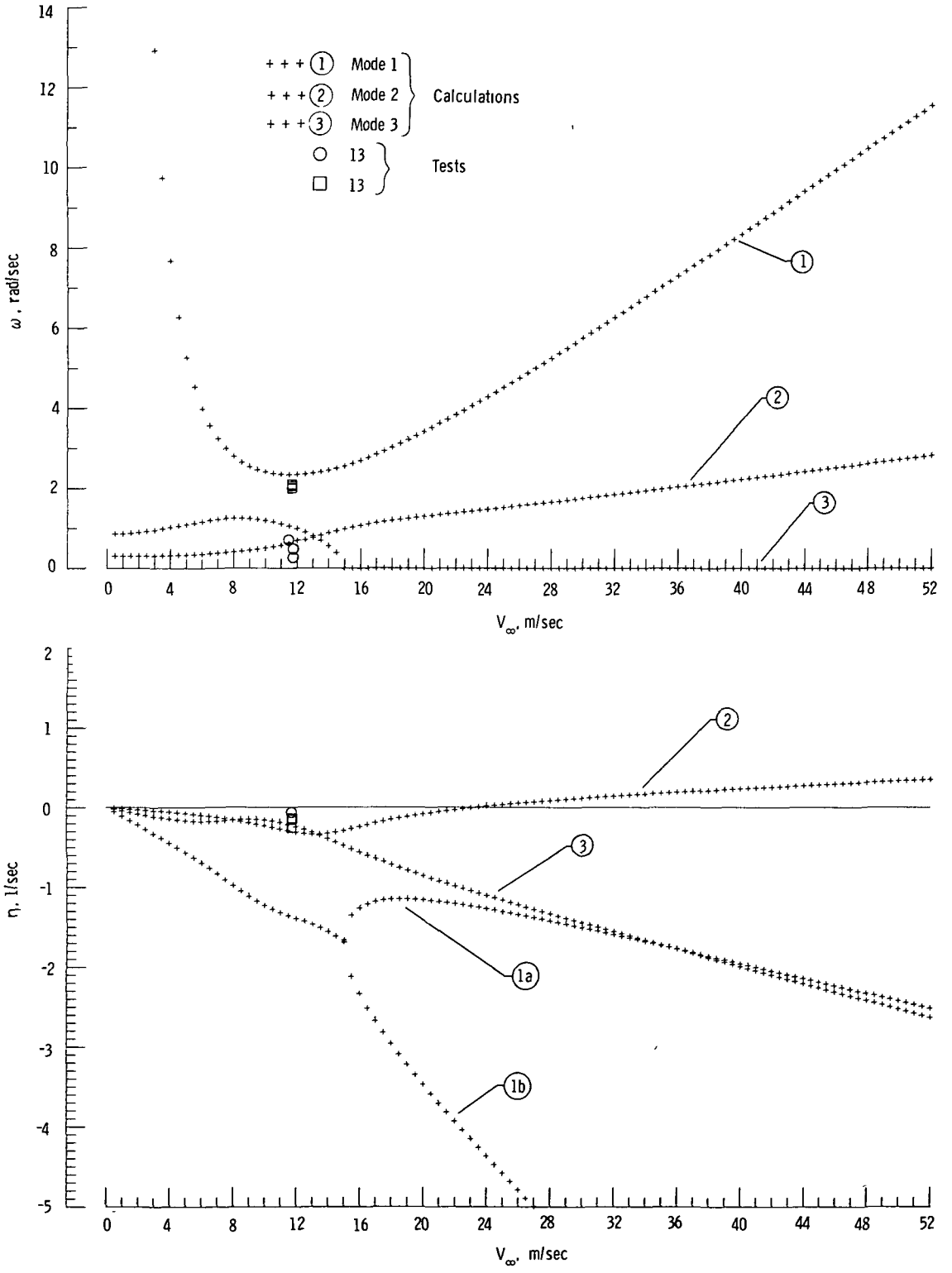

Figure 10.- Variation of longitudinal stability characteristics ω and η with V_∞ for configuration of test 13.

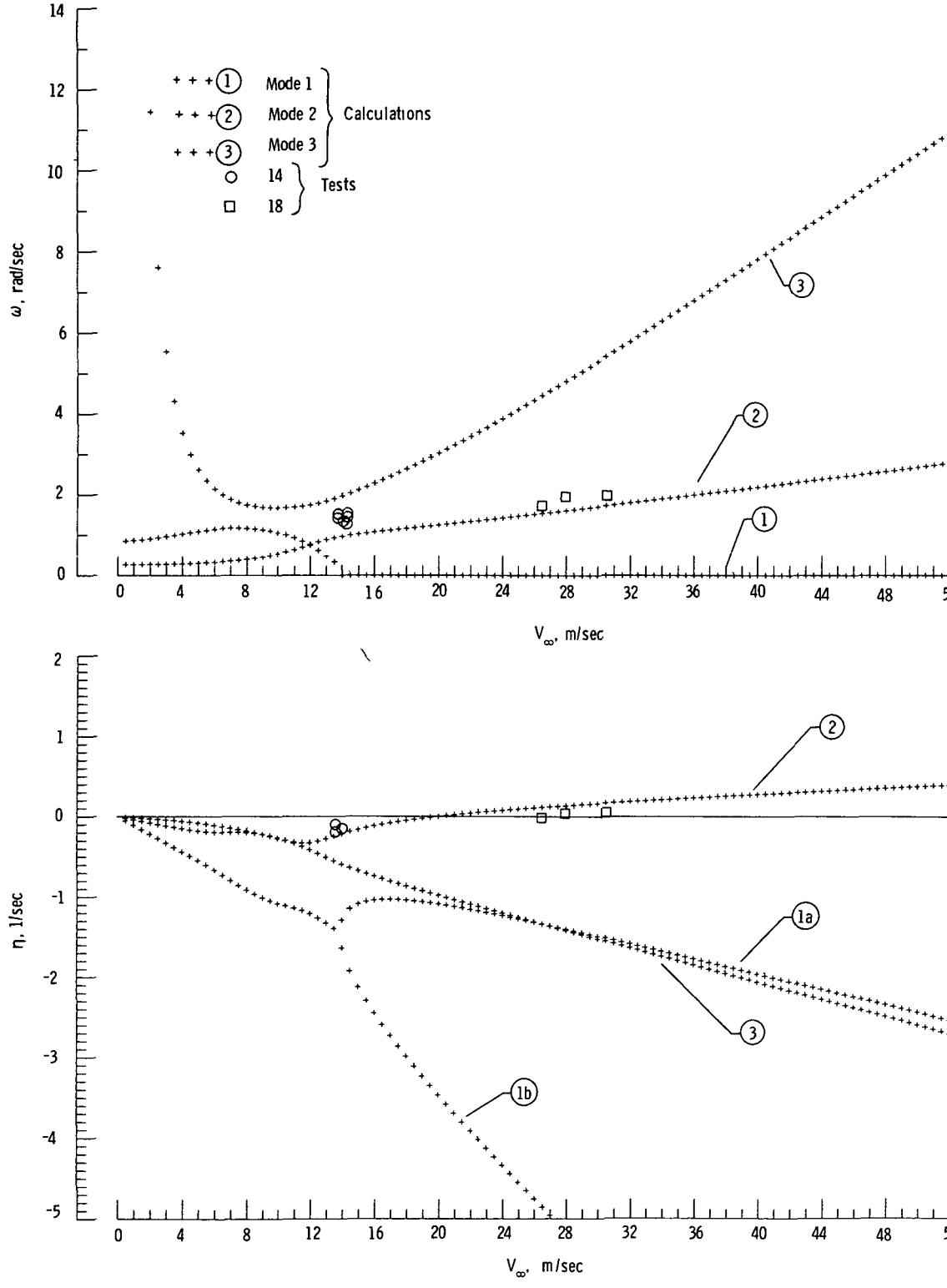

Figure 11.- Variation of longitudinal stability characteristics ω and η with V_∞ for configuration of tests 14 and 18.

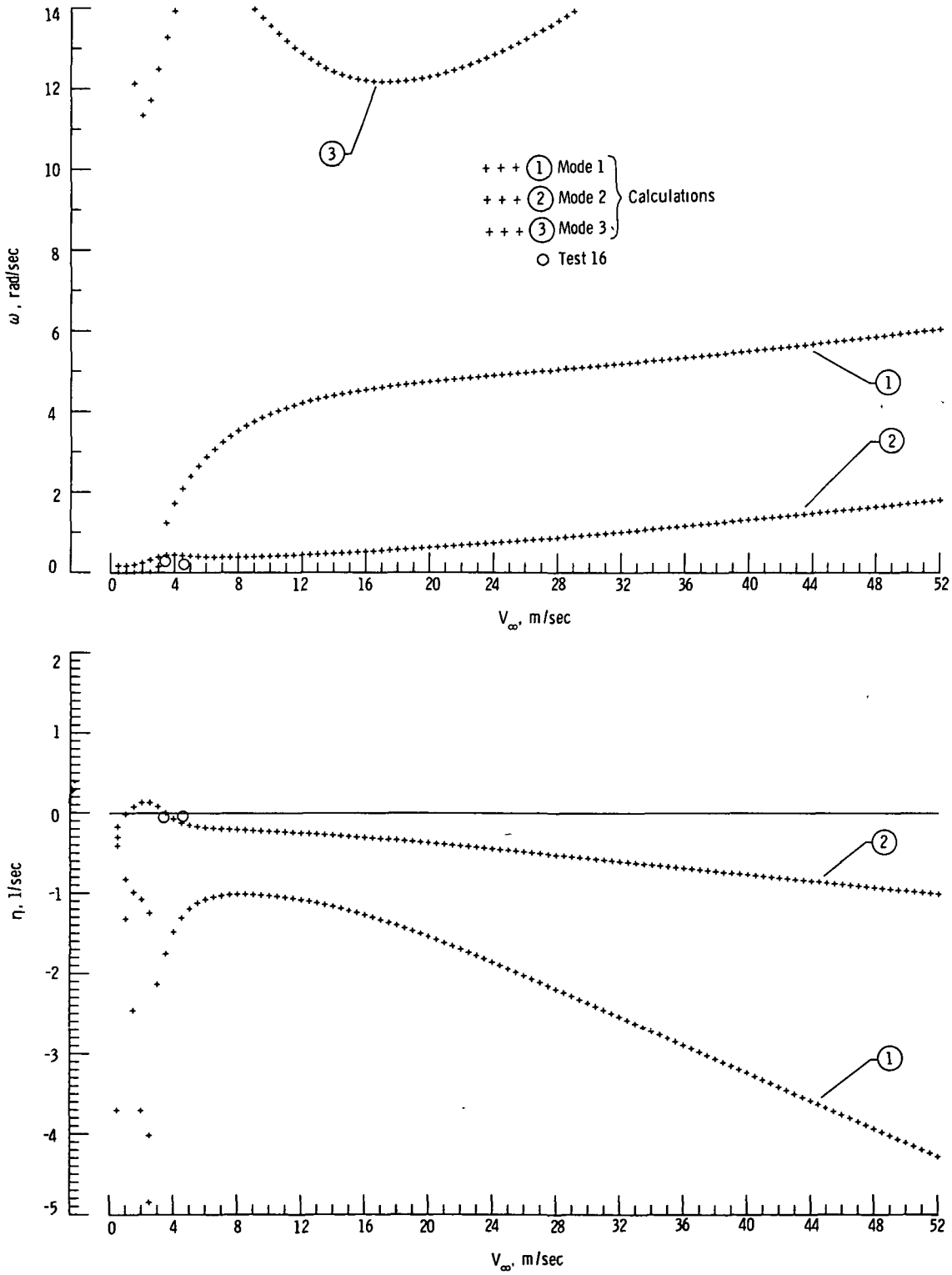

Figure 12.- Variation of longitudinal stability characteristics ω and η with V_∞ for configuration of test 16.

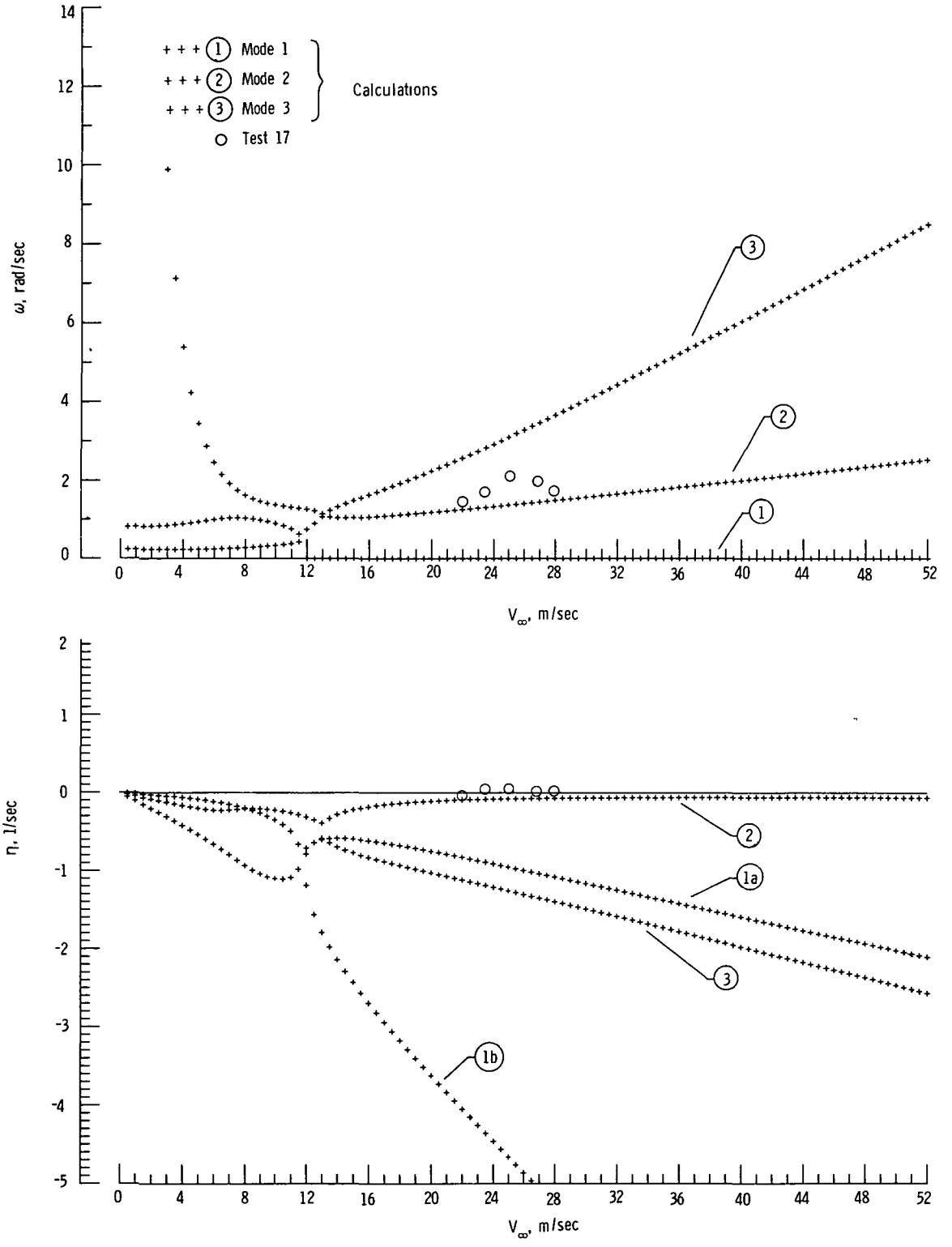

Figure 13.- Variation of longitudinal stability characteristics ω and η with V_∞ for configuration of test 17.

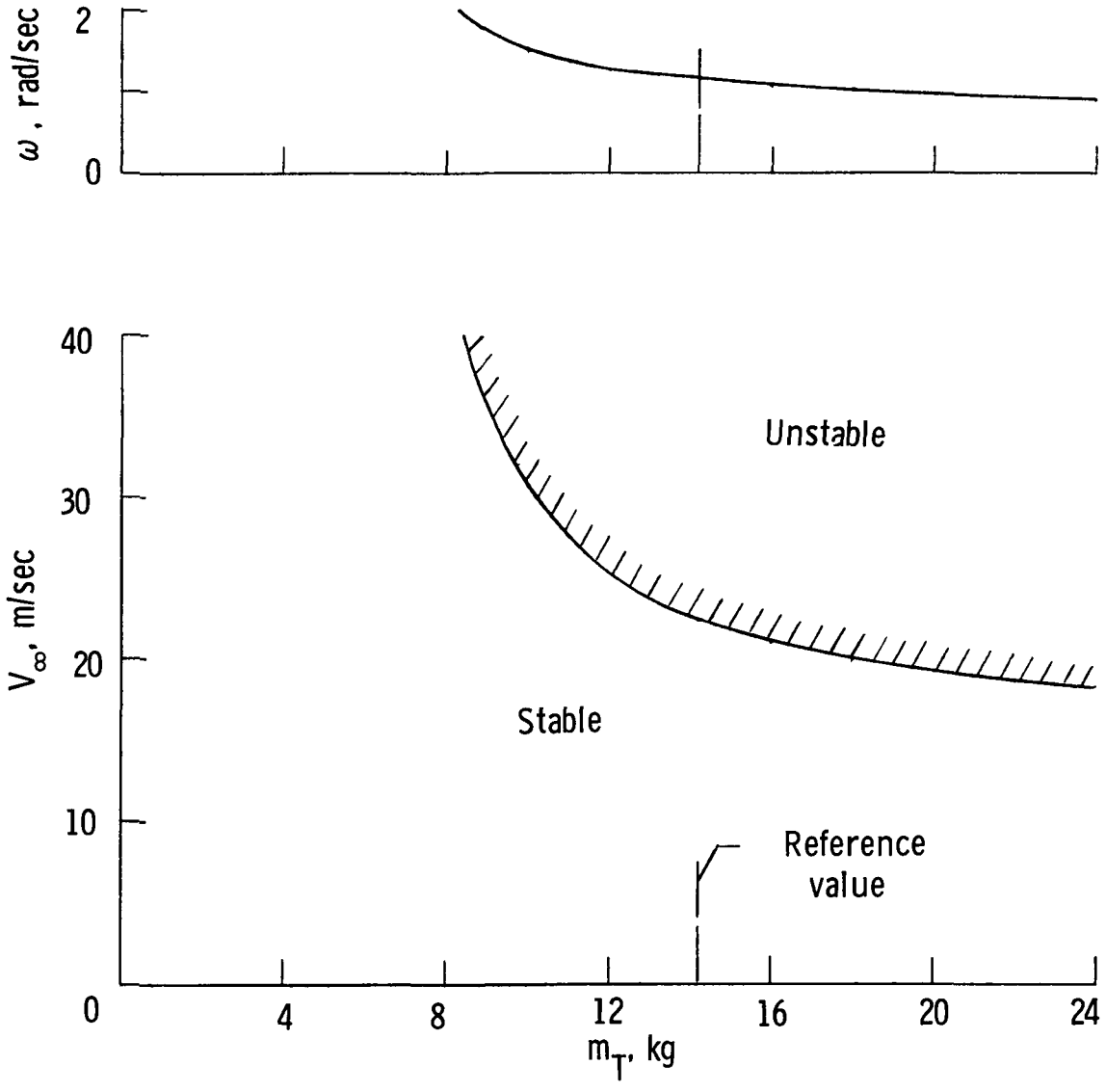

Figure 14.- Effect of m_T on calculated longitudinal-stability boundary.

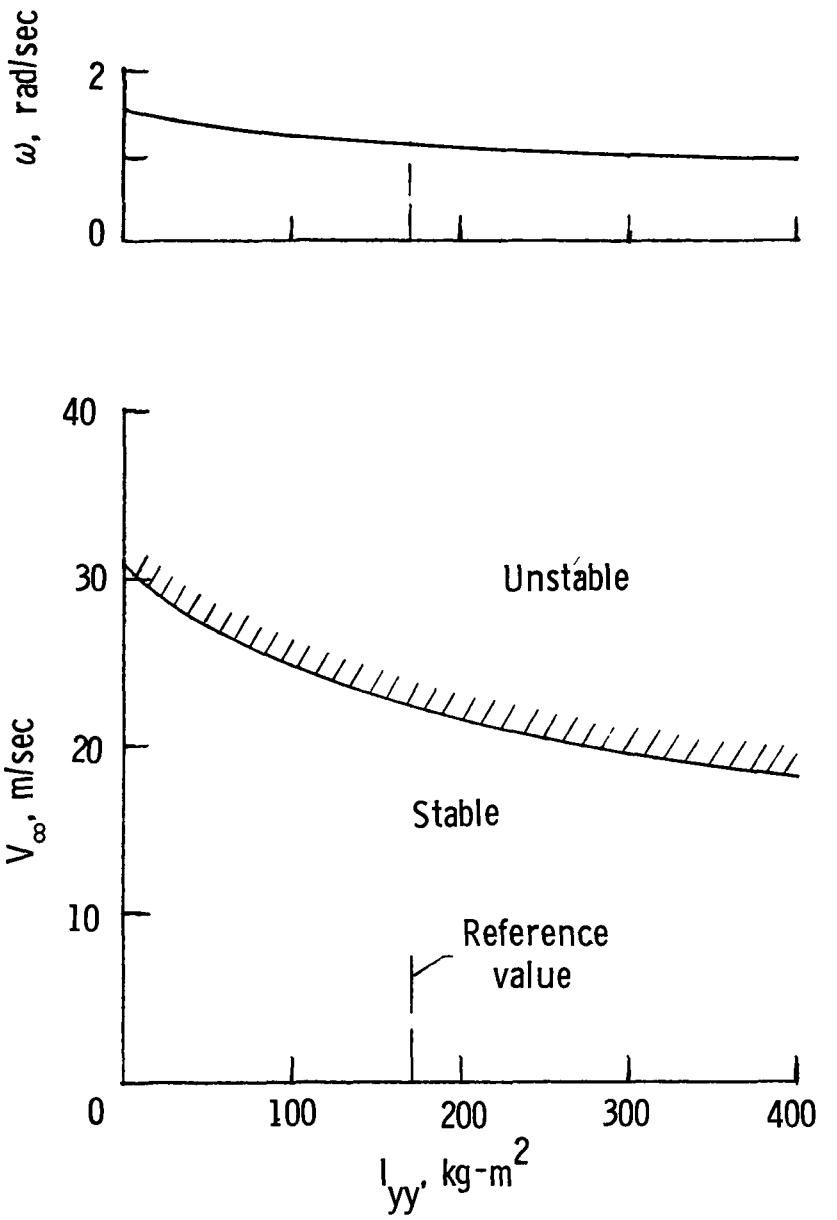

Figure 15.- Effect of I_{yy} on calculated longitudinal stability boundary.

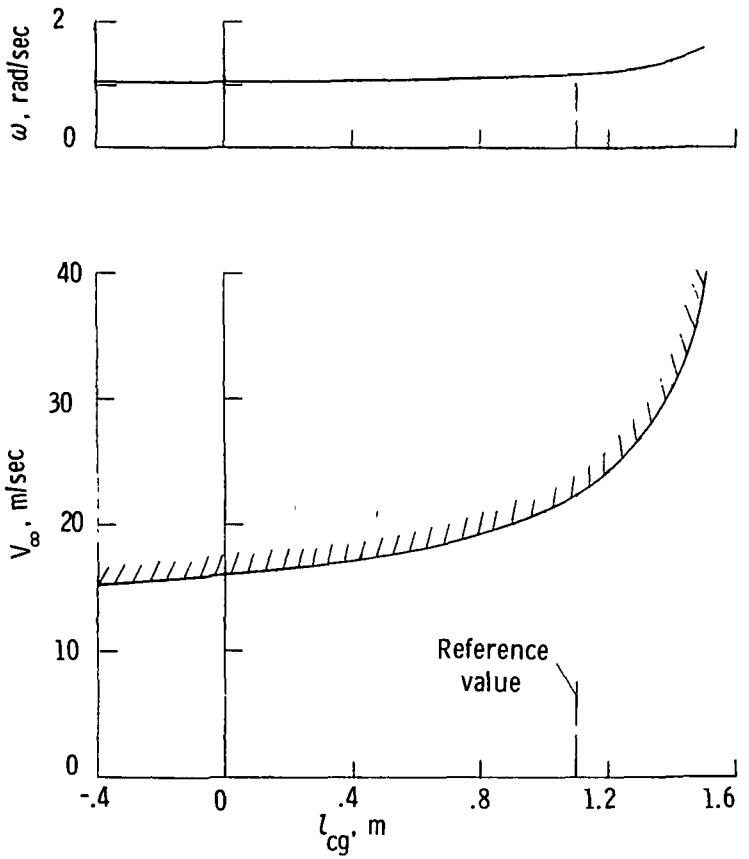

(a) Fore and aft location.

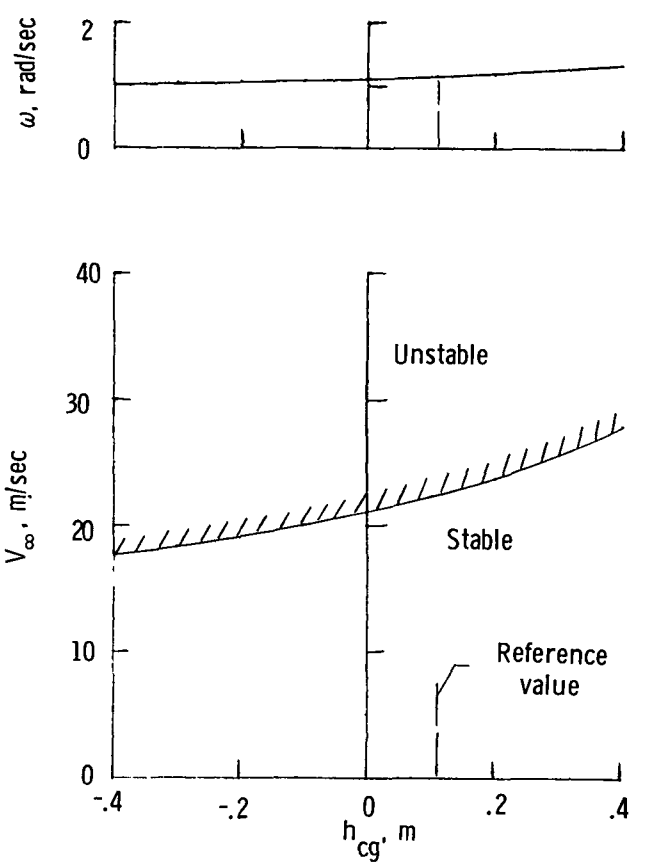

(b) Vertical location.

Figure 16.- Effect of center-of-mass location on calculated longitudinal stability boundaries.

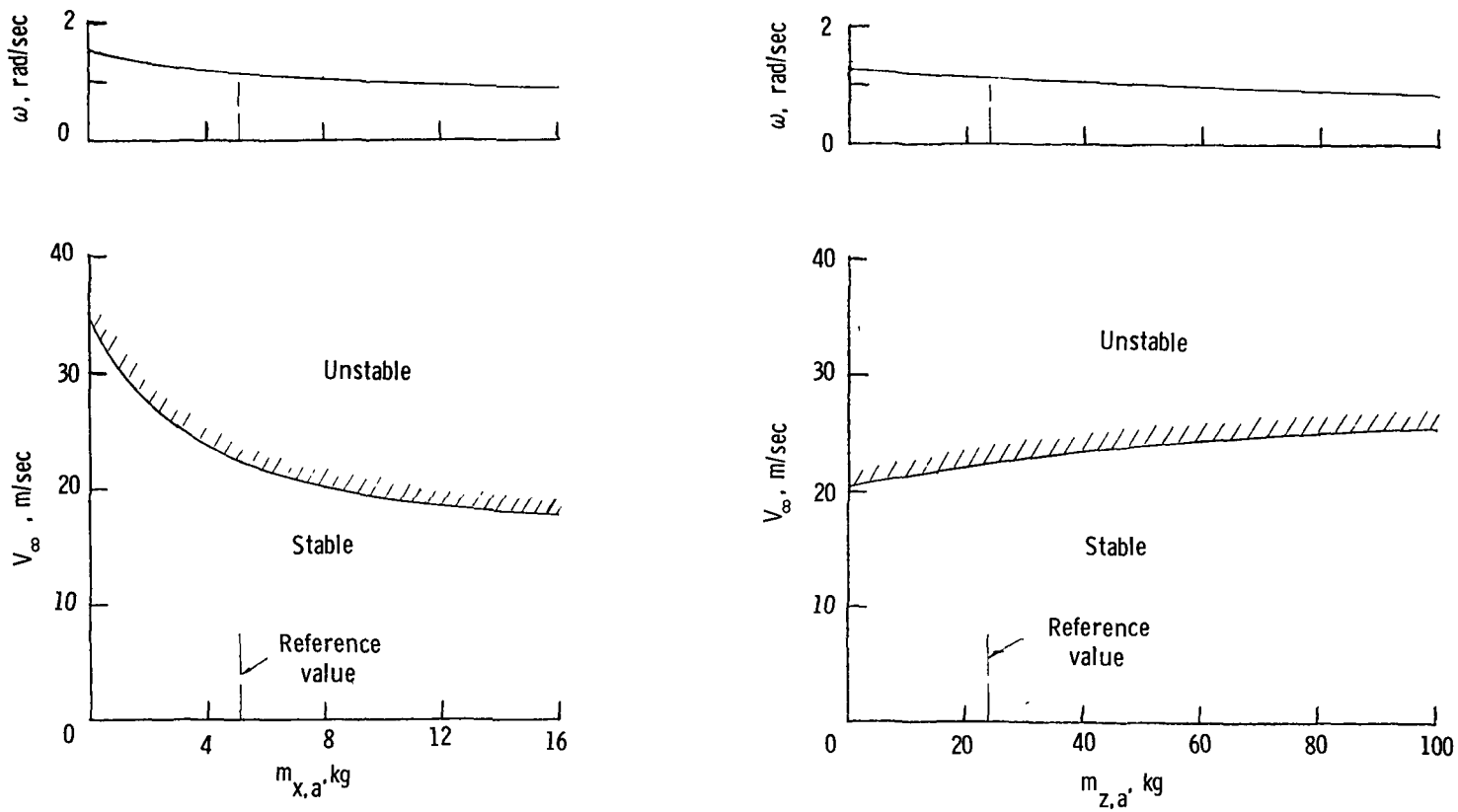

(a) Apparent mass $m_{x,a}$.

(b) Apparent mass $m_{z,a}$.

Figure 17.- Effect of apparent mass on calculated longitudinal stability boundaries.

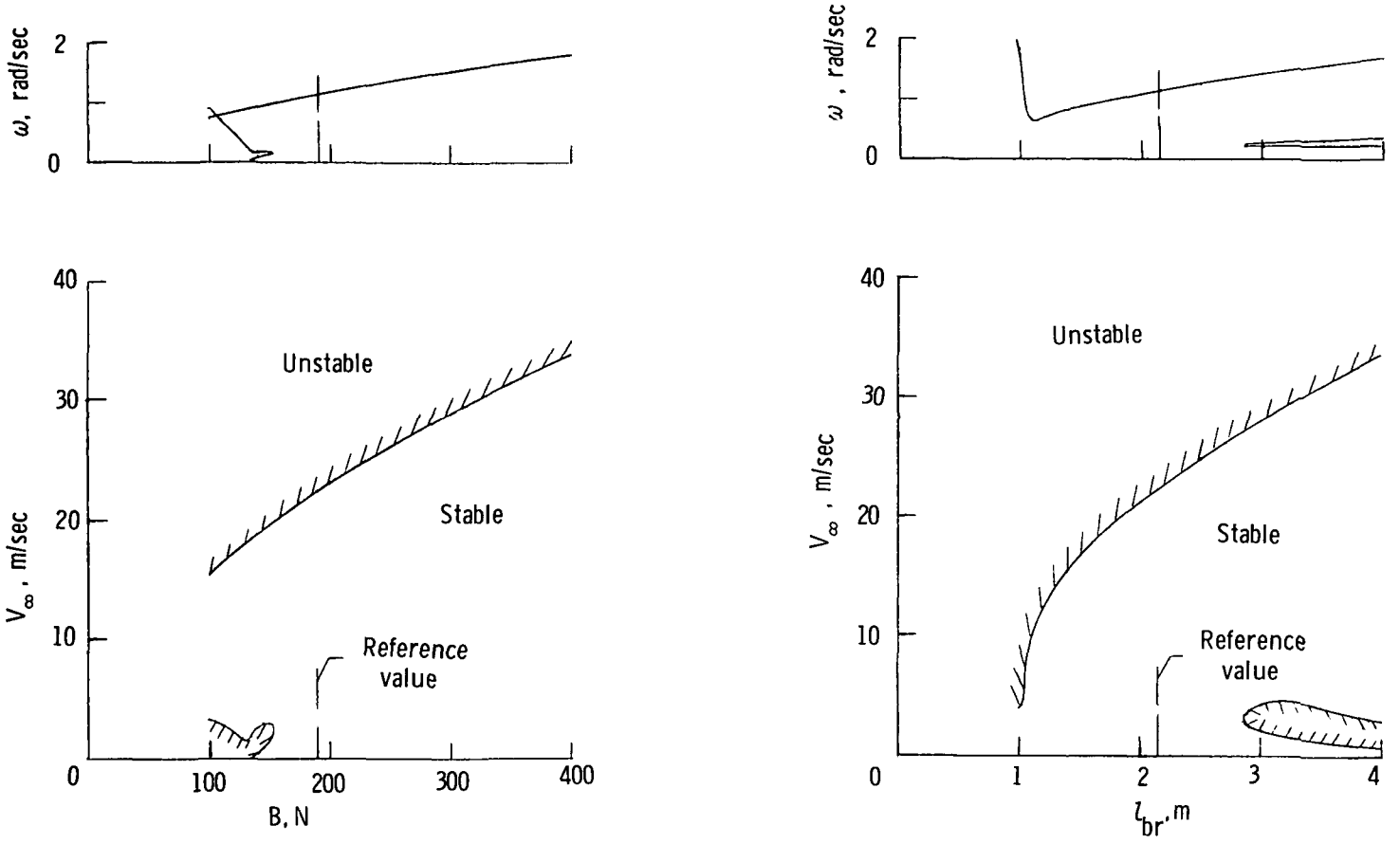

(a) Buoyancy force.

(b) Location of buoyancy force.

Figure 18.- Effect of buoyancy force on calculated longitudinal stability boundaries.

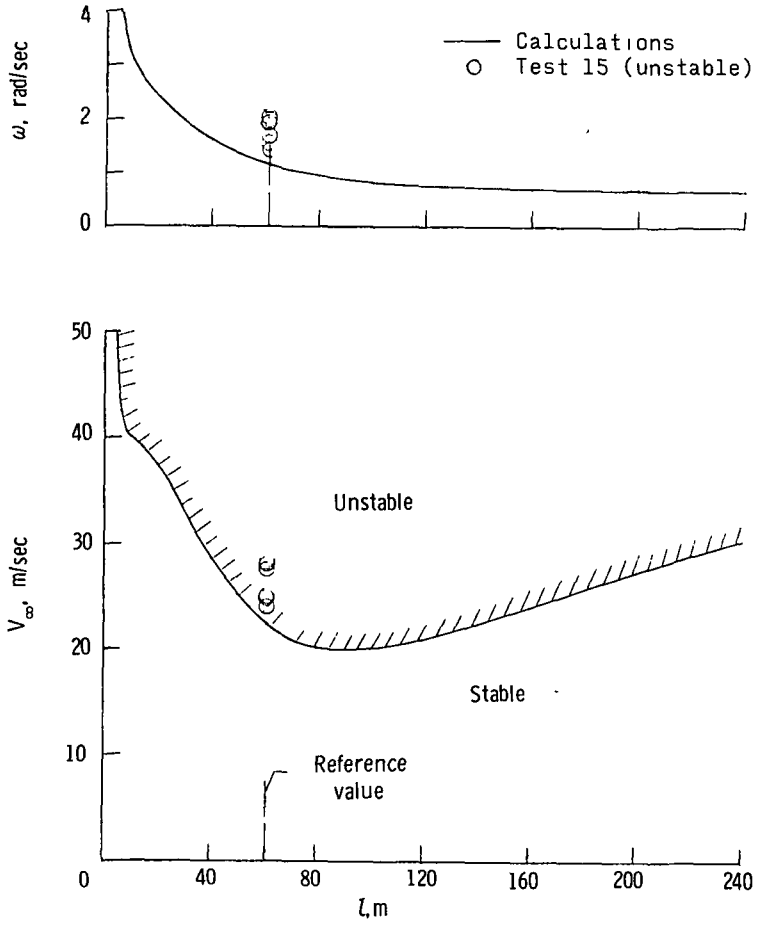

(a) Stability boundary.

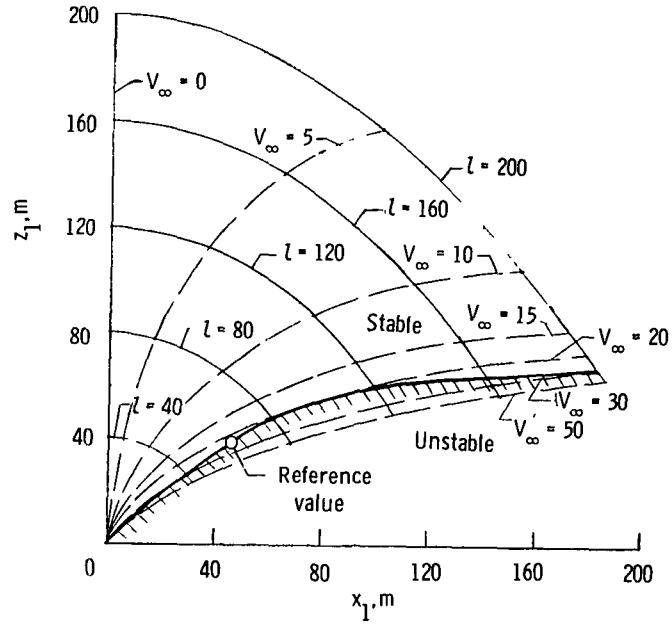

(b) Balloon position.

Figure 19.- Effect of tether-cable length on calculated balloon position and on calculated longitudinal stability boundary.

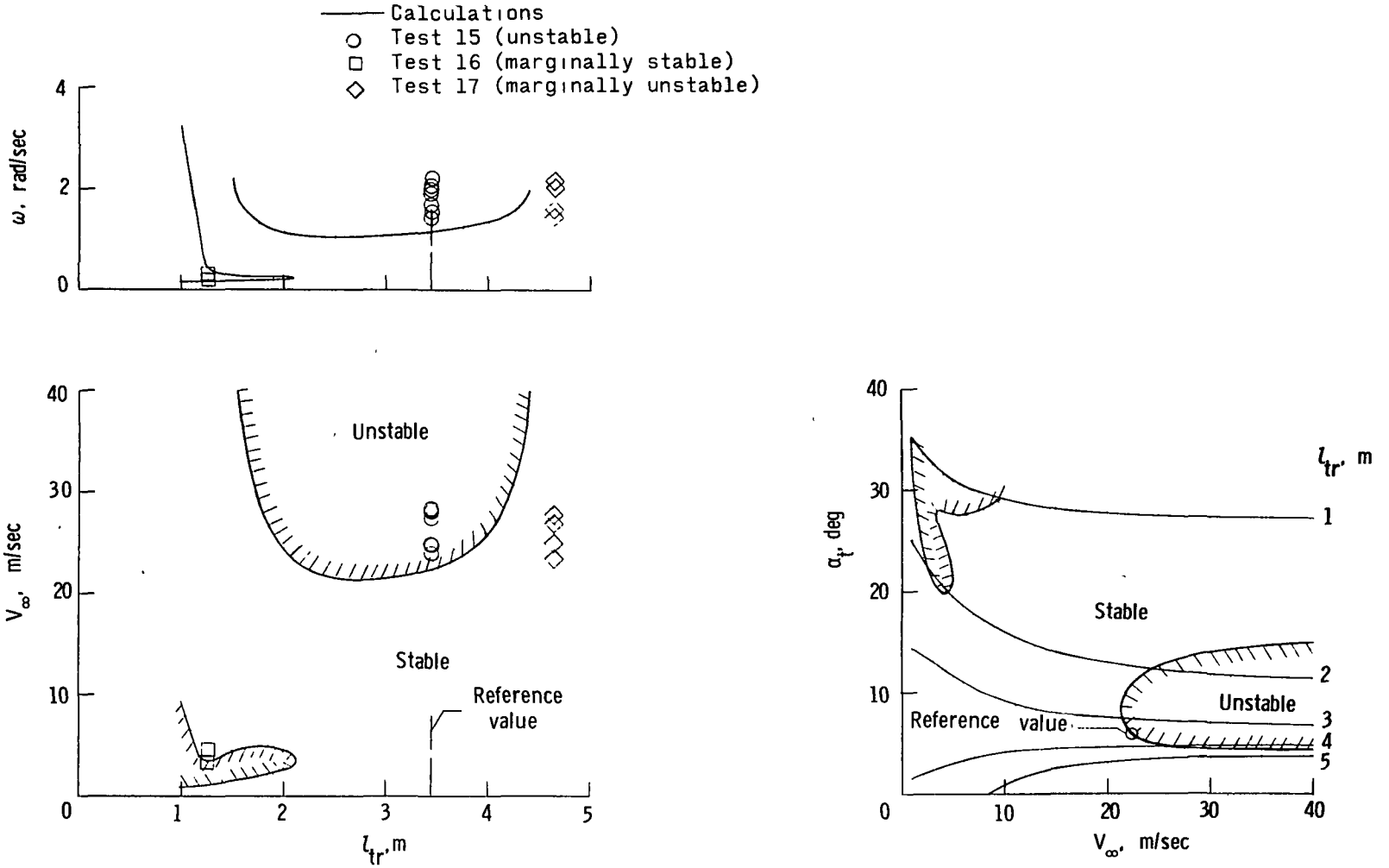

(a) Stability boundaries.

(b) Trim angle of attack.

Figure 20.- Effect of forward location of l_{tr} on calculated longitudinal stability boundaries and on calculated trim angle of attack.

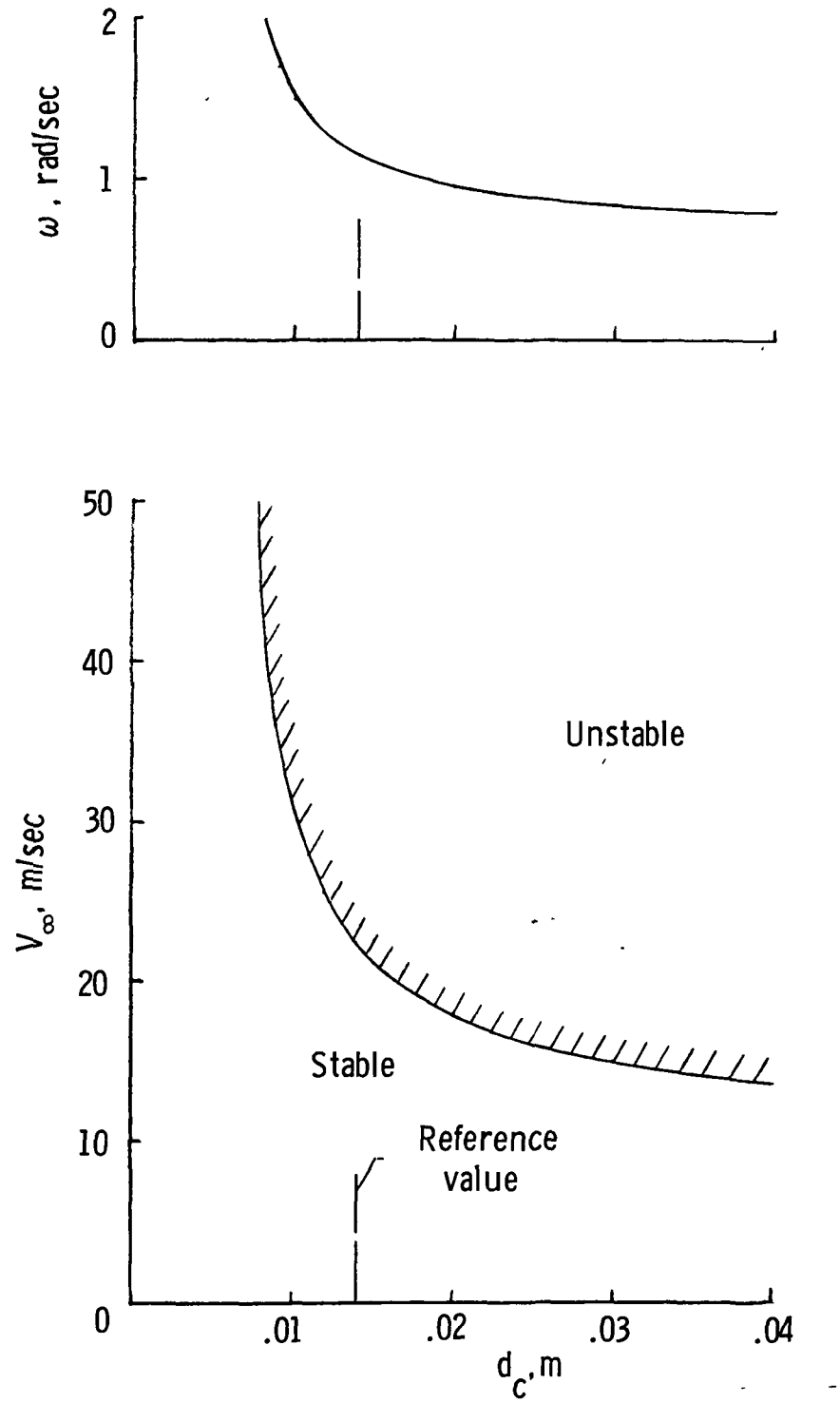

(a) Stability boundary.

Figure 21.- Effect of cable diameter on calculated longitudinal stability boundary and balloon location for constant w_c.

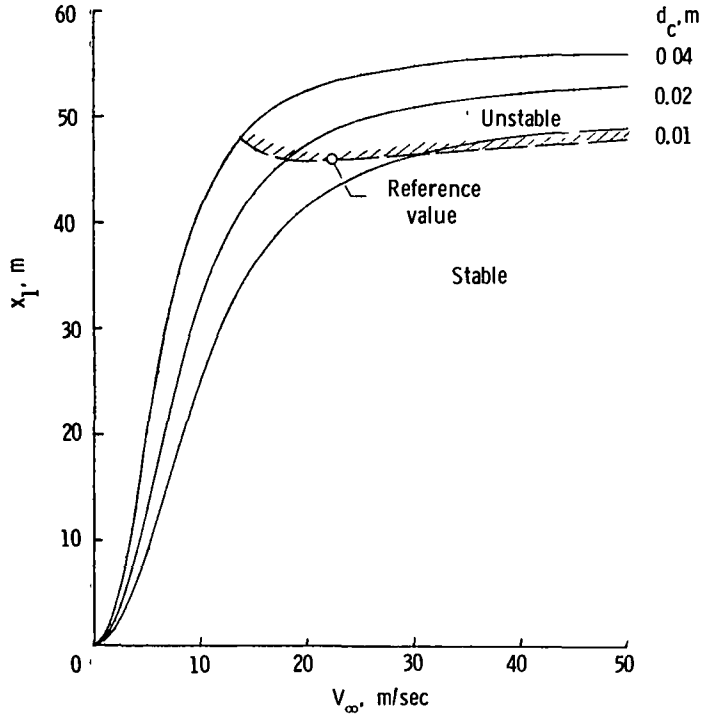

(b) Downstream distance x_1.

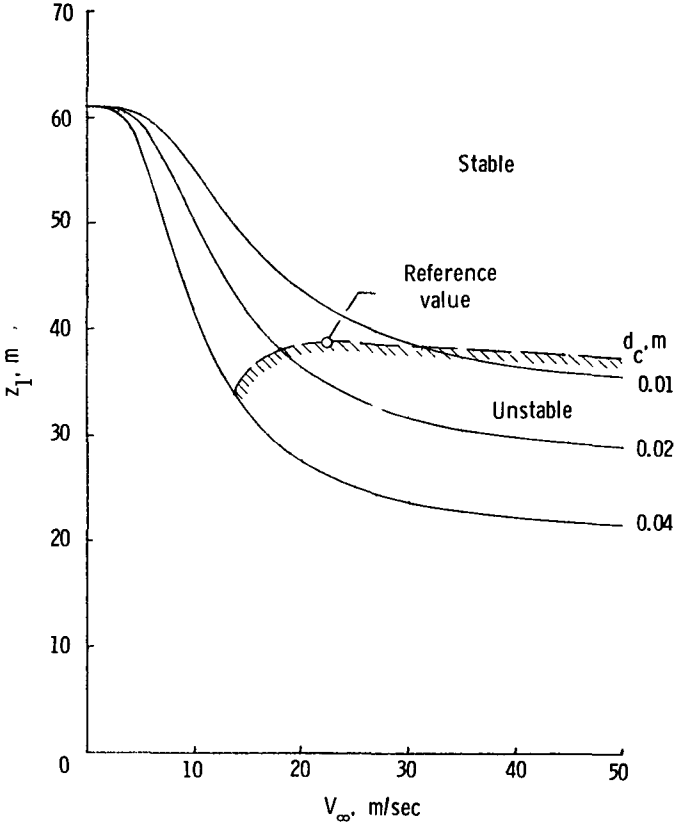

(c) Height z_1.

Figure 21.- Concluded.

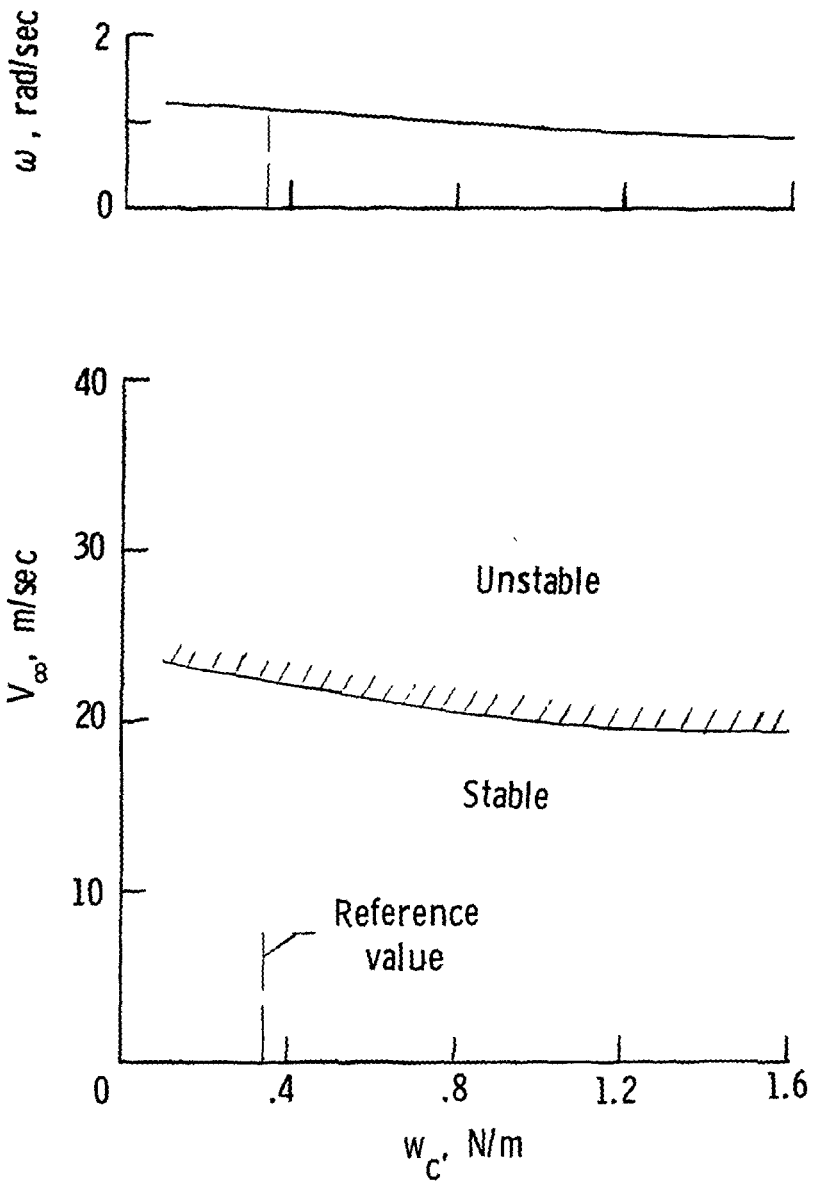

Figure 22.- Effect of cable weight per unit length on calculated longitudinal stability boundary.

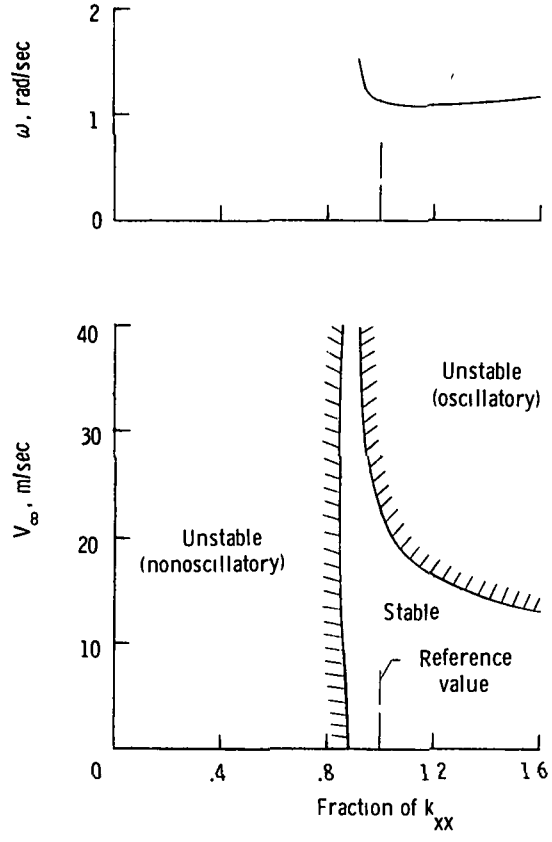

(a) Fraction of calculated derivative k_{xx}.

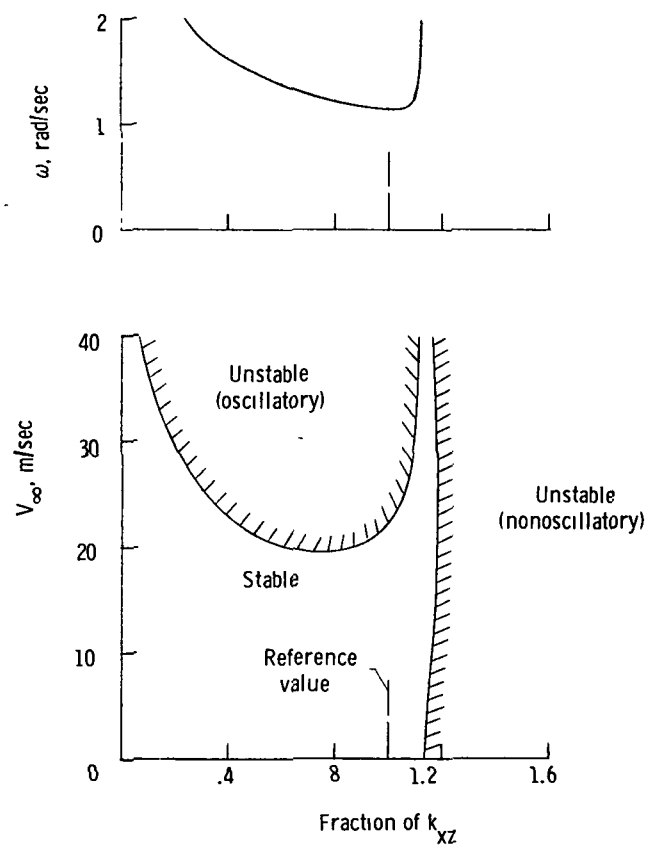

(b) Fraction of calculated derivative k_{xz}.

Figure 23.- Effect of change in each tether-cable derivative on calculated longitudinal stability boundaries.

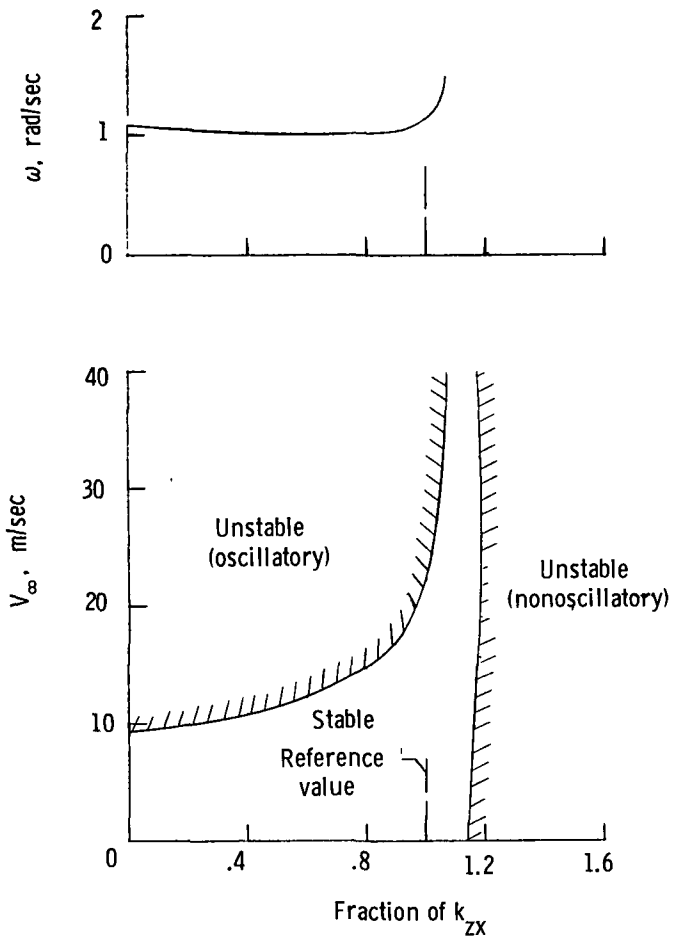

(c) Fraction of calculated derivative k_{zx}.

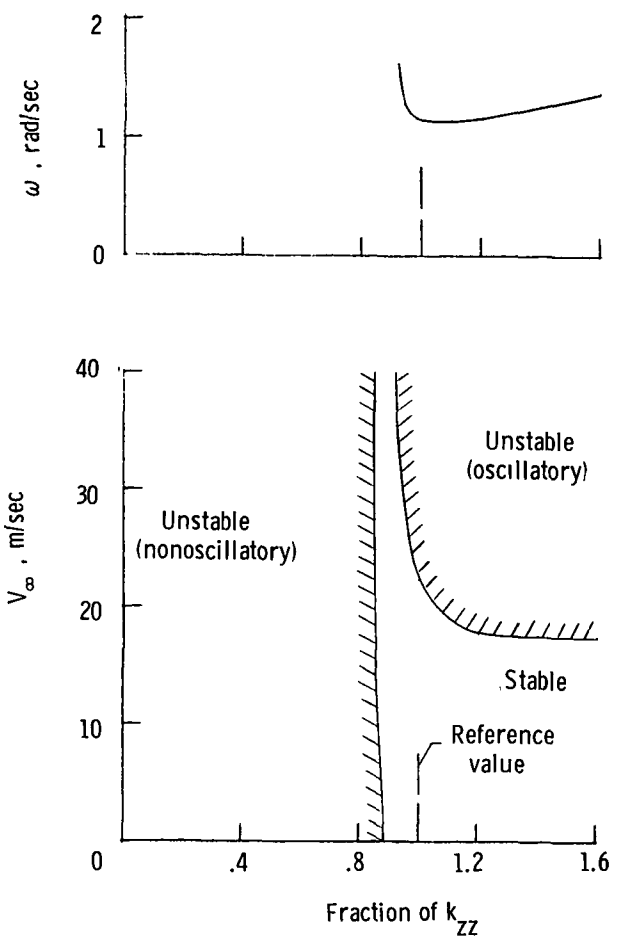

(d) Fraction of calculated derivative k_{zz}.

Figure 23.- Concluded.

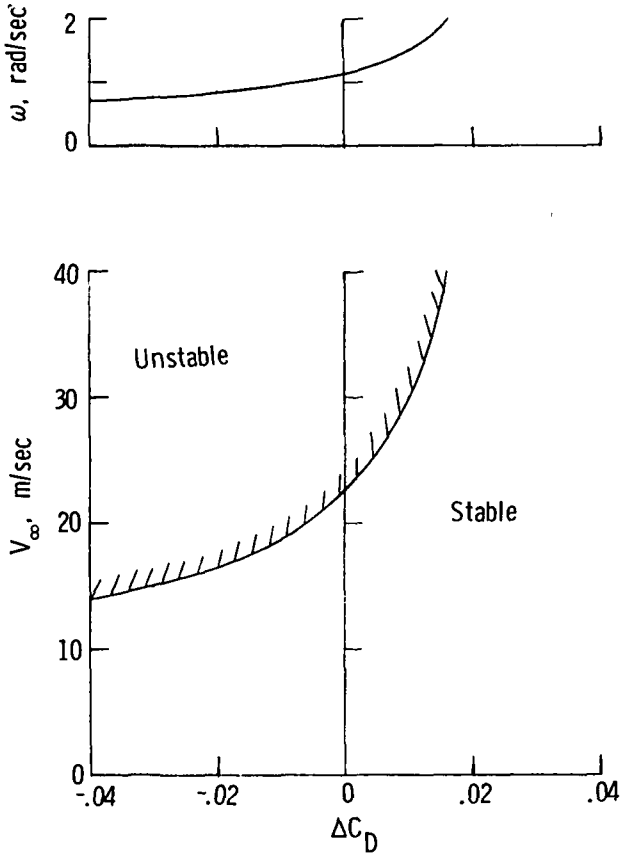

(a) Change in drag coefficient.

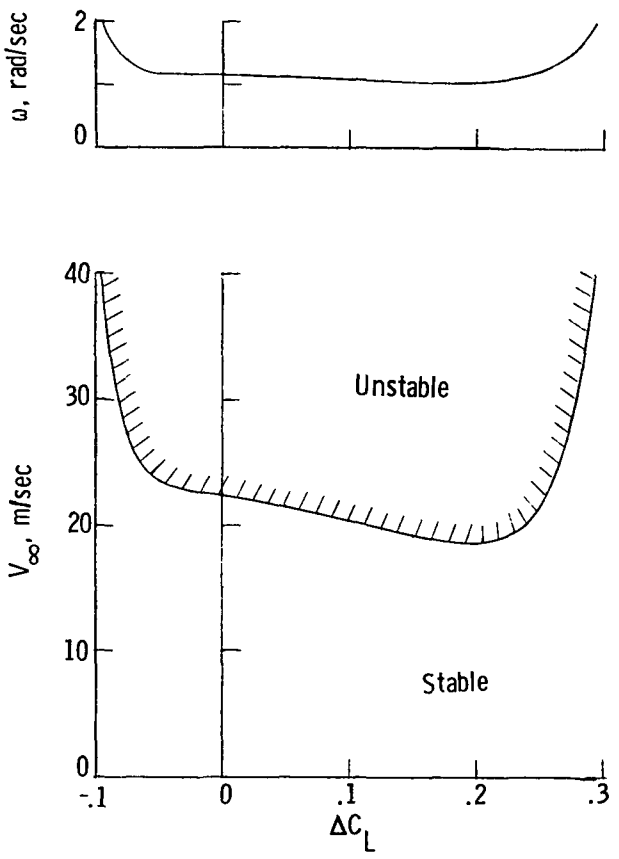

(b) Change in lift coefficient.

Figure 24.- Effect of static aerodynamic coefficients on calculated longitudinal stability boundaries.

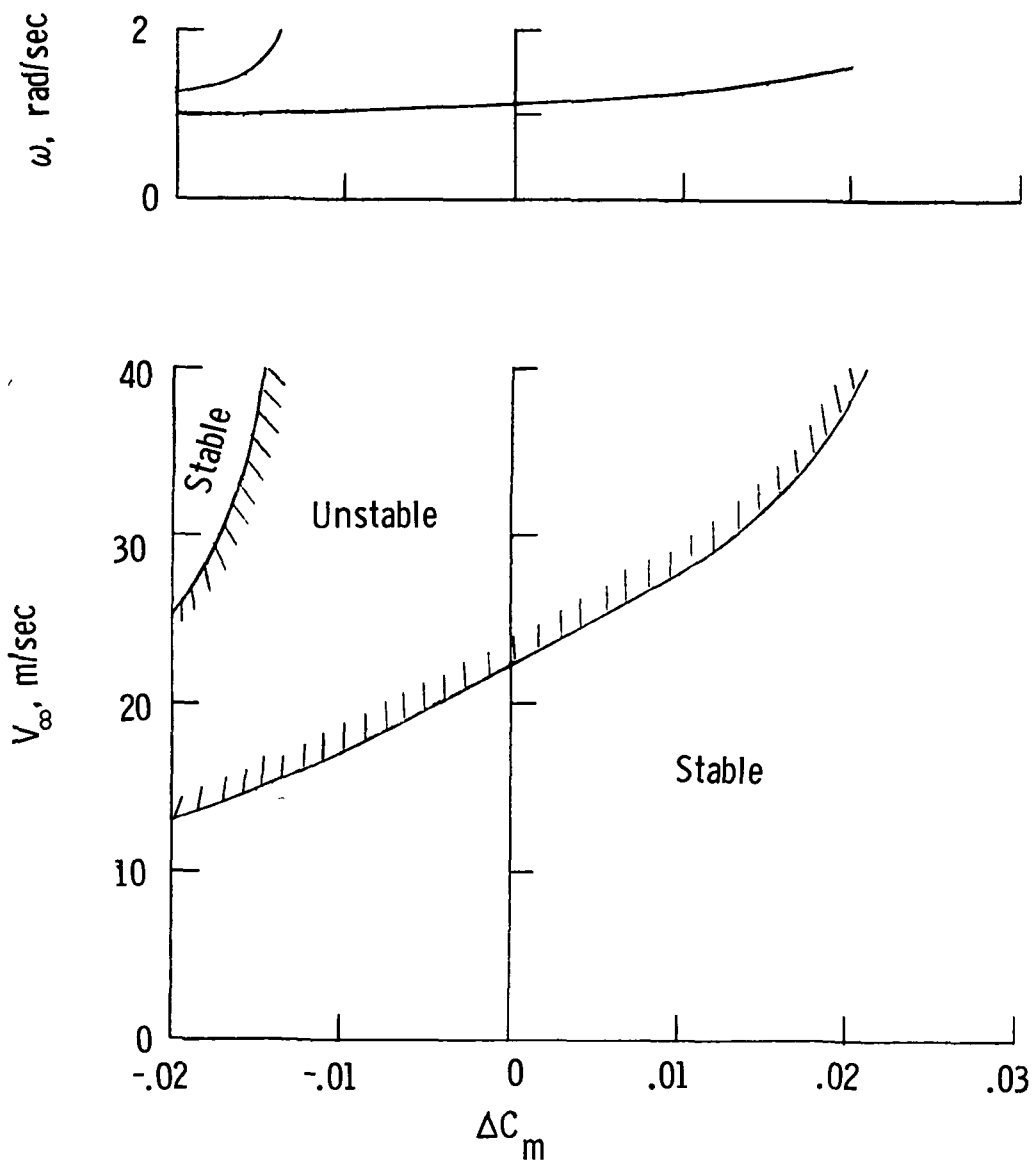

(c) Change in pitching-moment coefficient.

Figure 24.- Concluded.

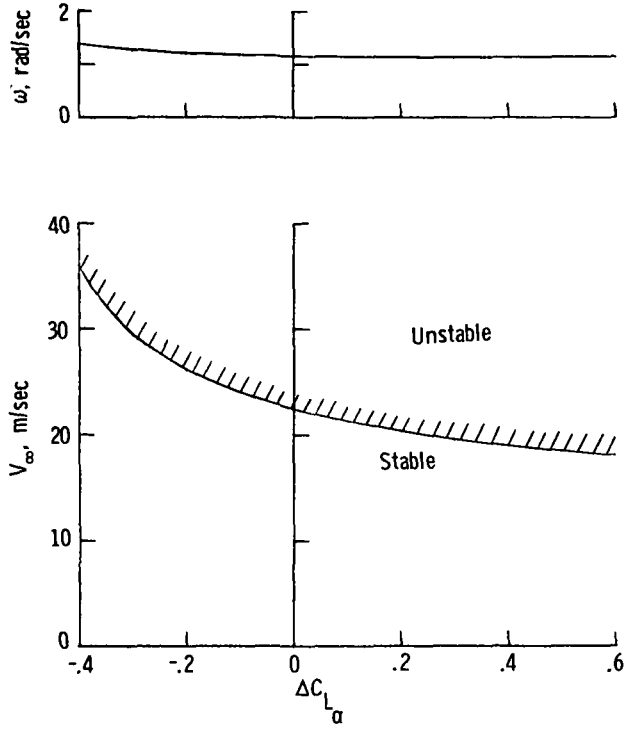

(a) Change in C_{L_α}.

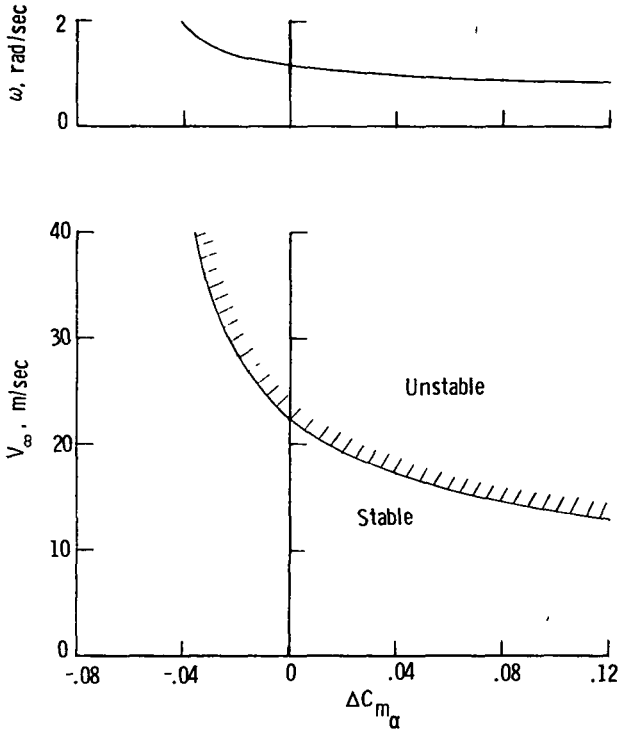

(b) Change in C_{m_α}.

Figure 25.- Effect of change in angle-of-attack derivatives on calculated longitudinal stability boundaries.

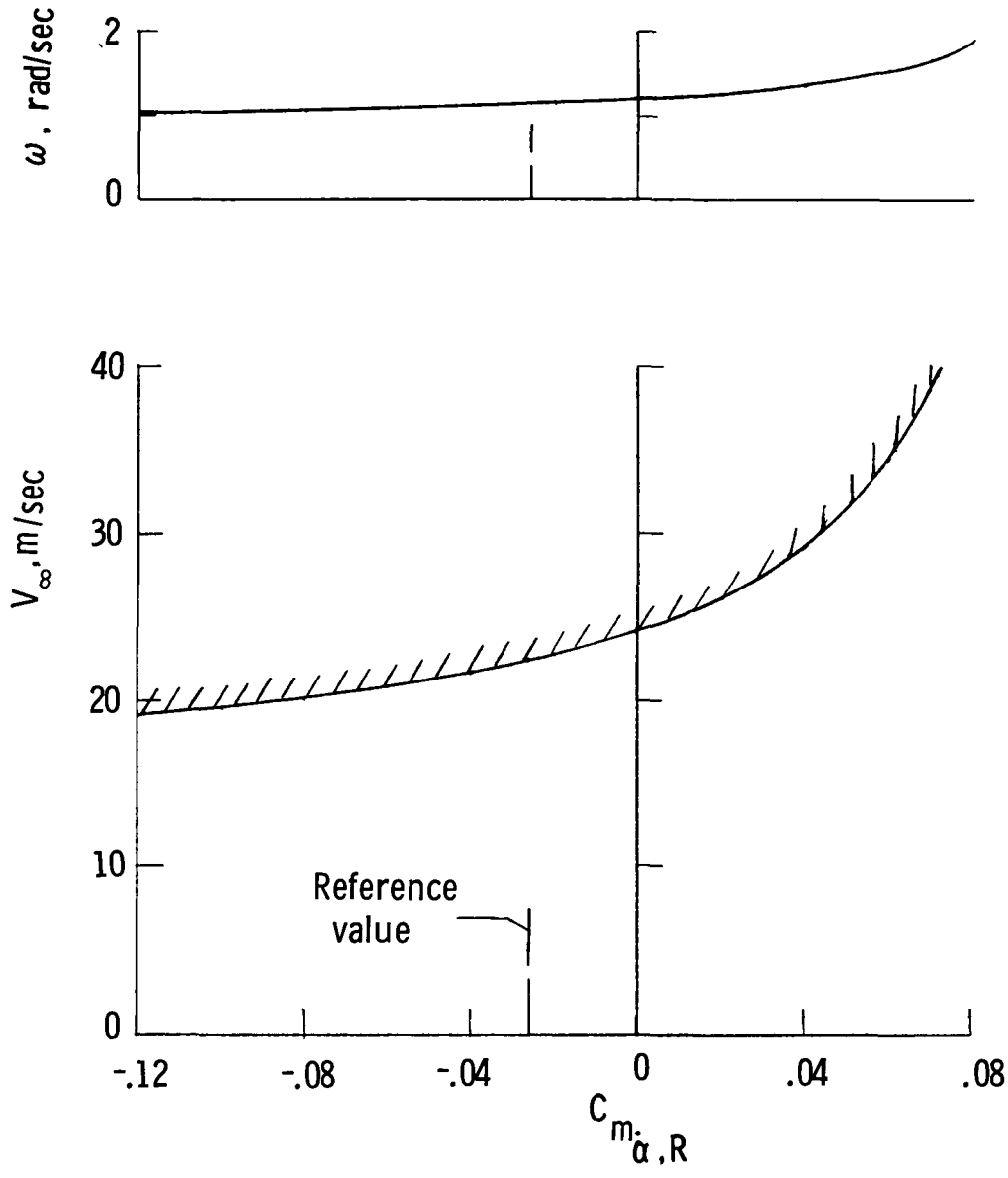

Figure 26.- Effect of $C_{m_{\dot{\alpha},R}}$ on calculated longitudinal stability boundary.

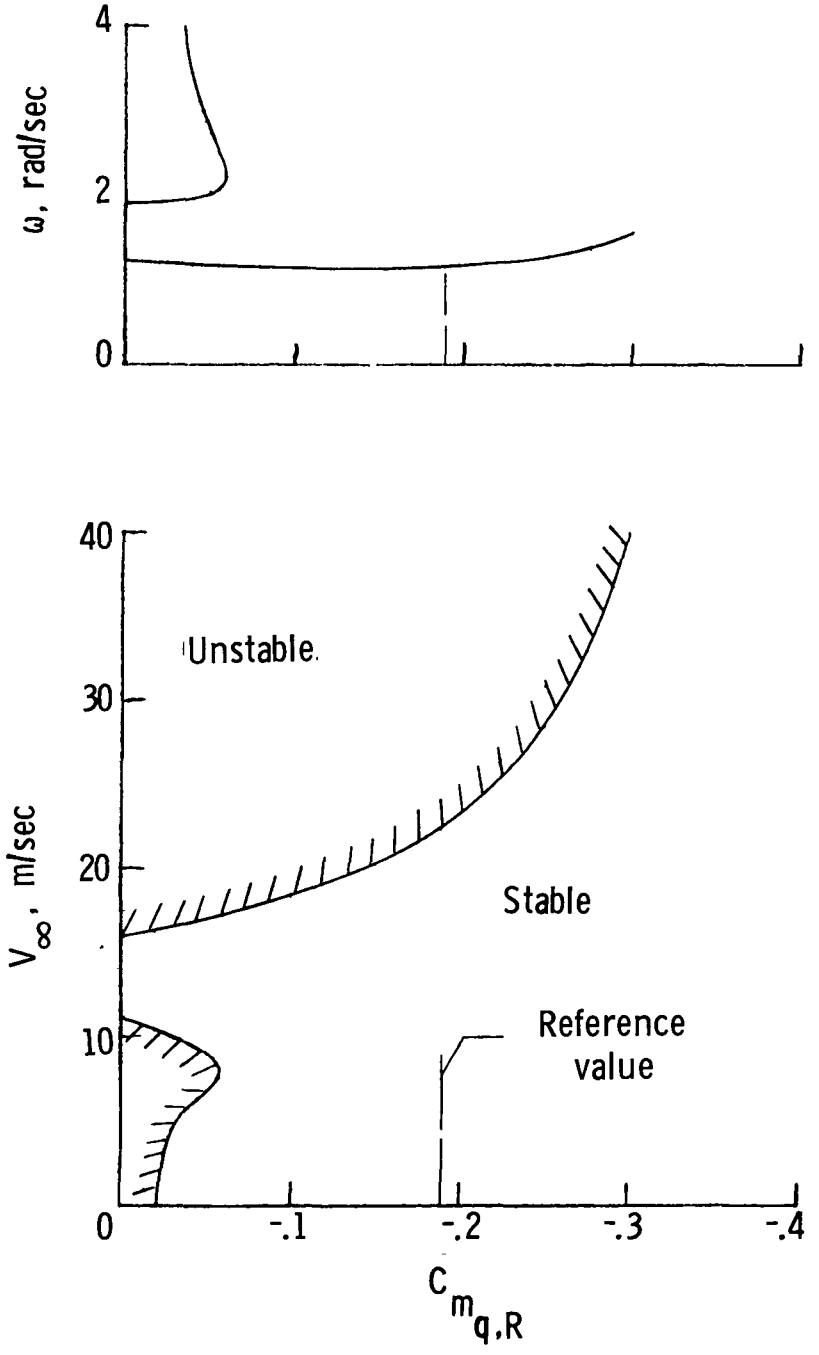

Figure 27.- Effect of $C_{m_{q,R}}$ on calculated longitudinal stability boundary.

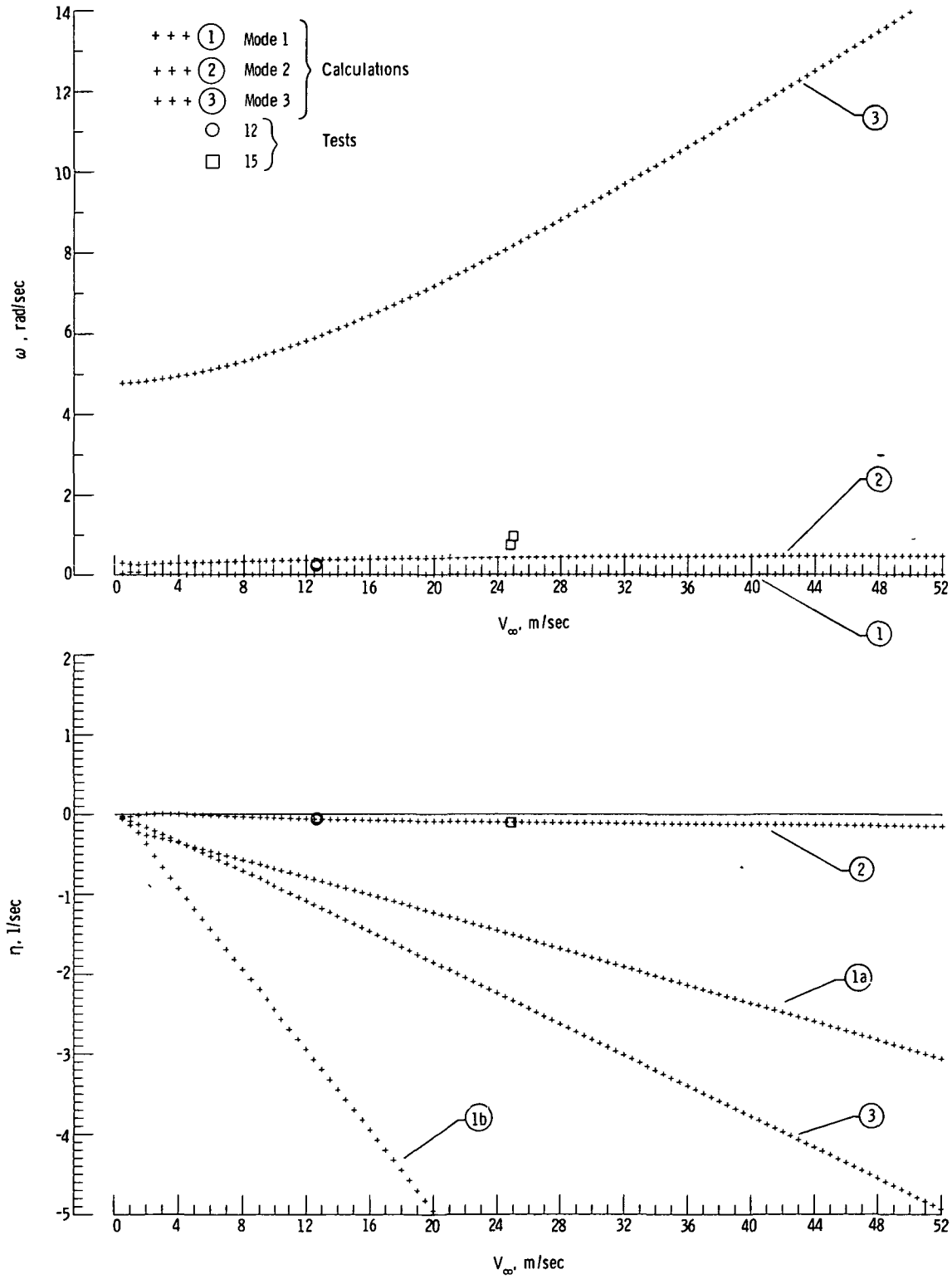

(a) ω and η versus V_∞.

Figure 28.- Variation of lateral stability characteristics with velocity for reference configuration (tests 12 and 15).

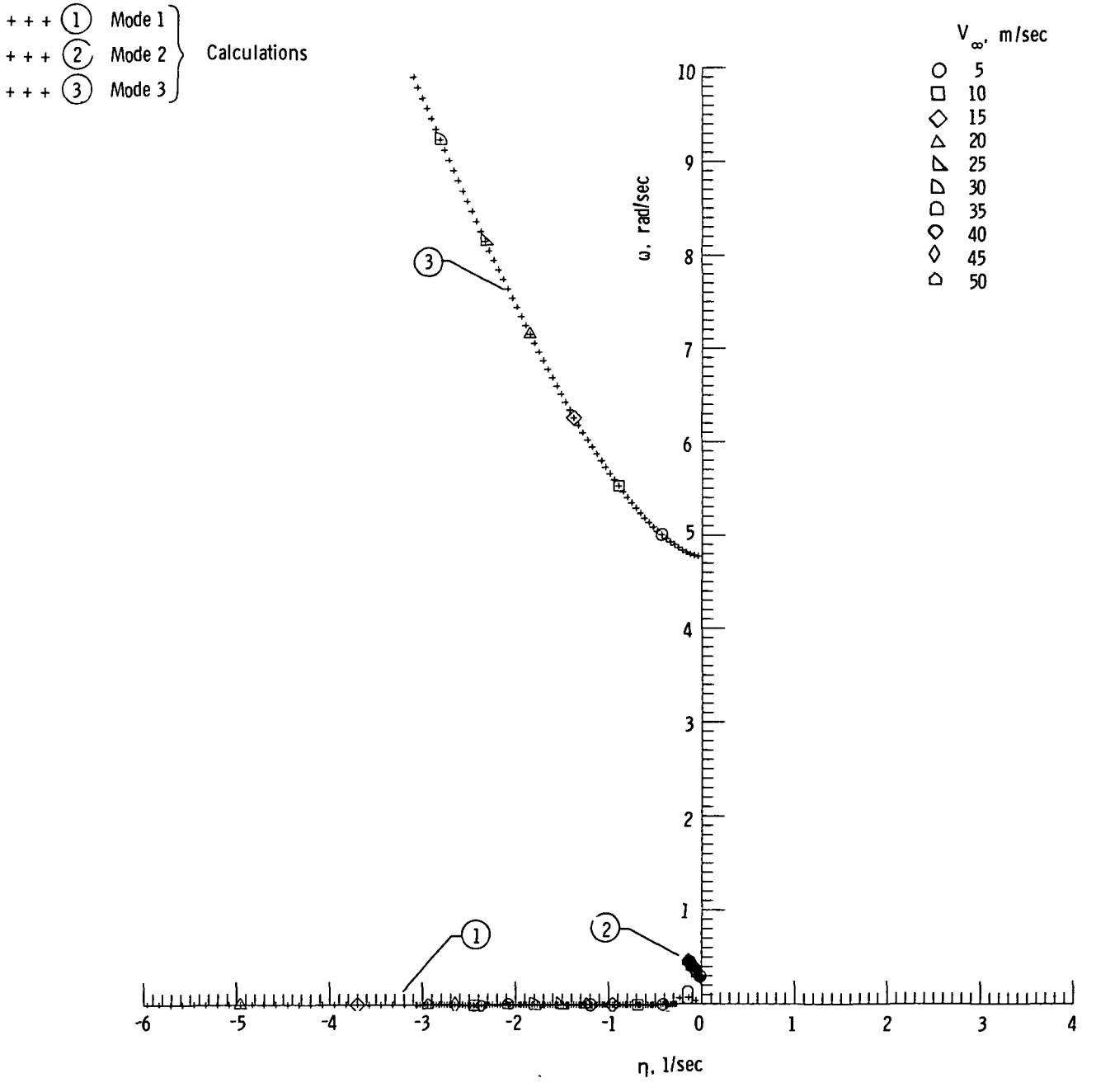

(b) Root locus plot with velocity as a parameter.

Figure 28.- Concluded.

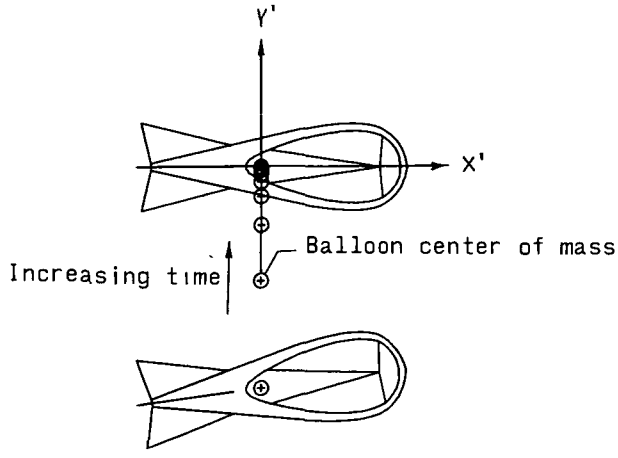

Mode 1a at V = 10 m/s; λ = -.681.

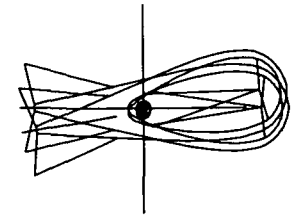

Mode 1b at V = 10 m/s; λ = -2.44.

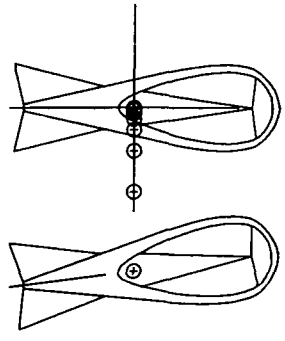

Mode 1a at V = 20 m/s; λ = -1.23.

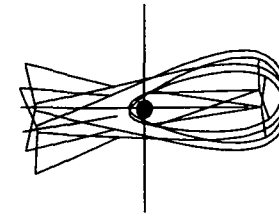

Mode 1b at V = 20 m/s; λ = -4.95.

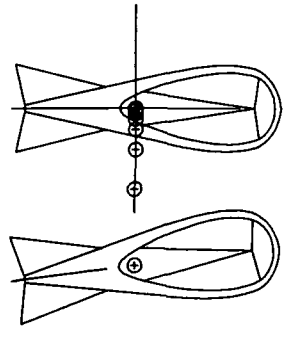

Mode 1a at V = 30 m/s; λ = -1.80.

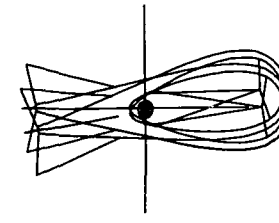

Mode 1b at V = 30 m/s; λ = -7.47.

(a) Modes 1a and 1b.

Figure 29.- Lateral modes of motion for reference configuration.

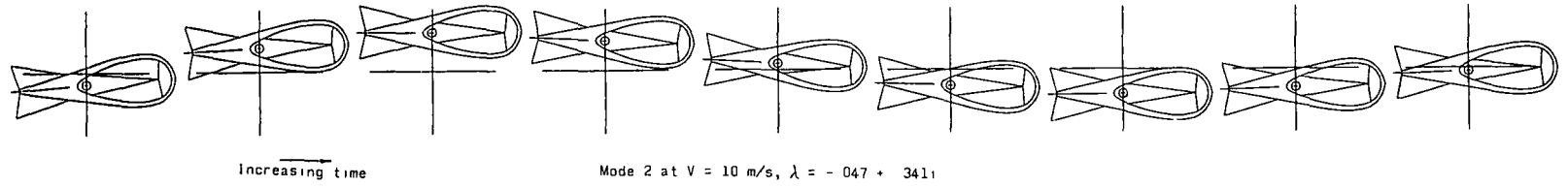

Mode 2 at V = 10 m/s, λ = - 047 + 341i

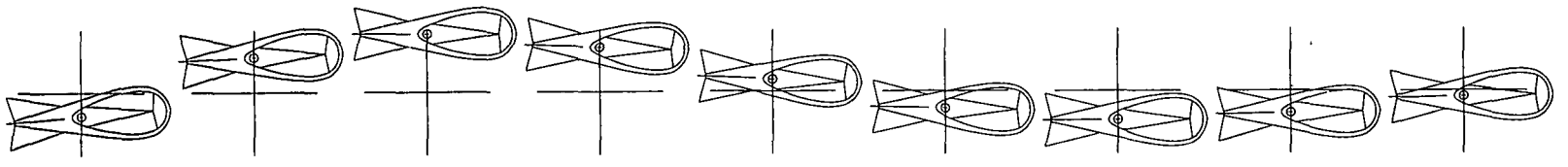

Mode 2 at V = 20 m/s; λ = - 089 + 407i

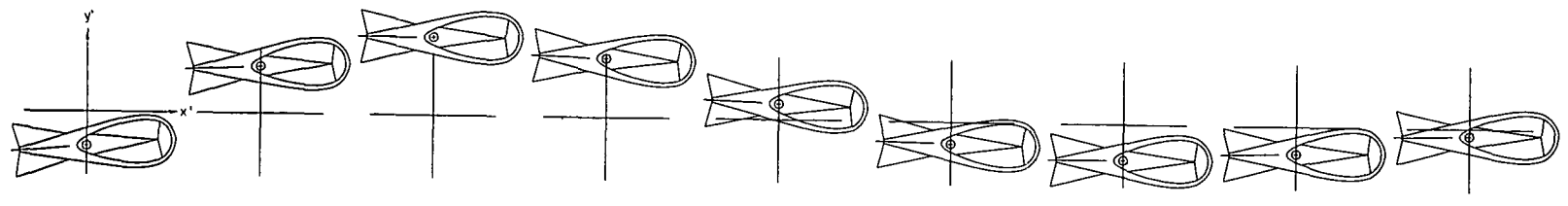

Mode 2 at V = 30 m/s, λ = - 109 + .439i.

(b) Mode 2.

Figure 29.- Continued.

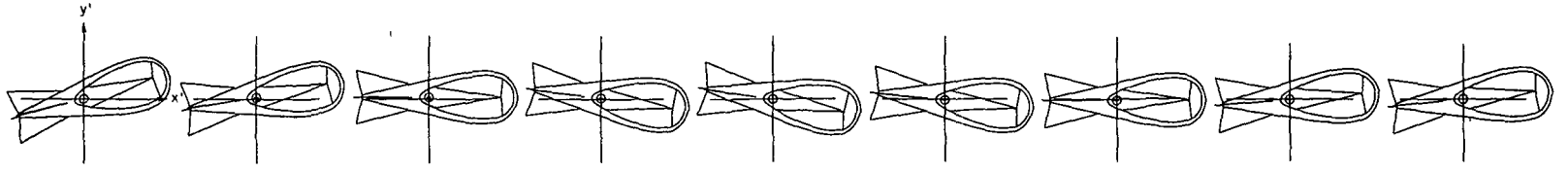

Mode 3 at V = 10 m/s, λ =- 900 + 5 54i

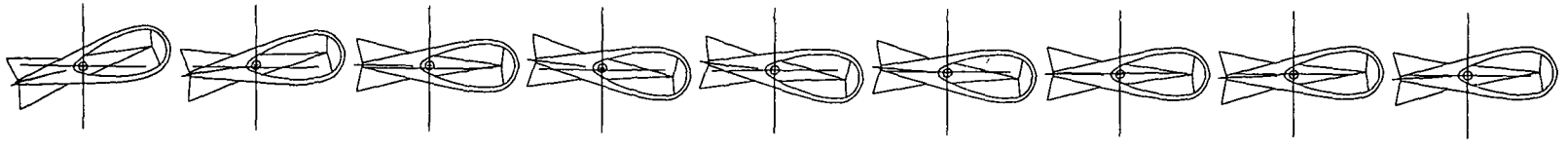

Mode 3 at V = 20 m/s, λ= -1 85 + 7 16i

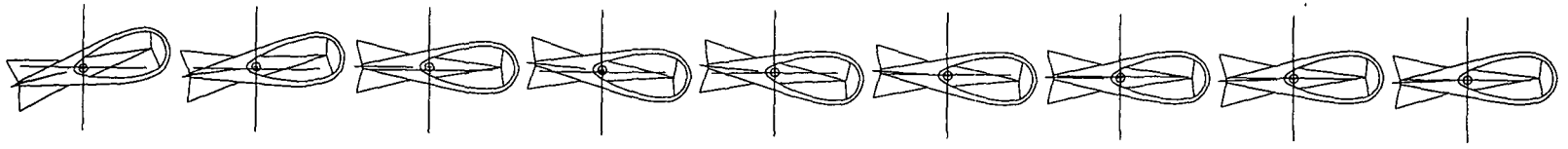

Mode 3 at V = 30 m/s; λ= -2 82 + 9.24i.

(c) Mode 3.

Figure 29.- Concluded.

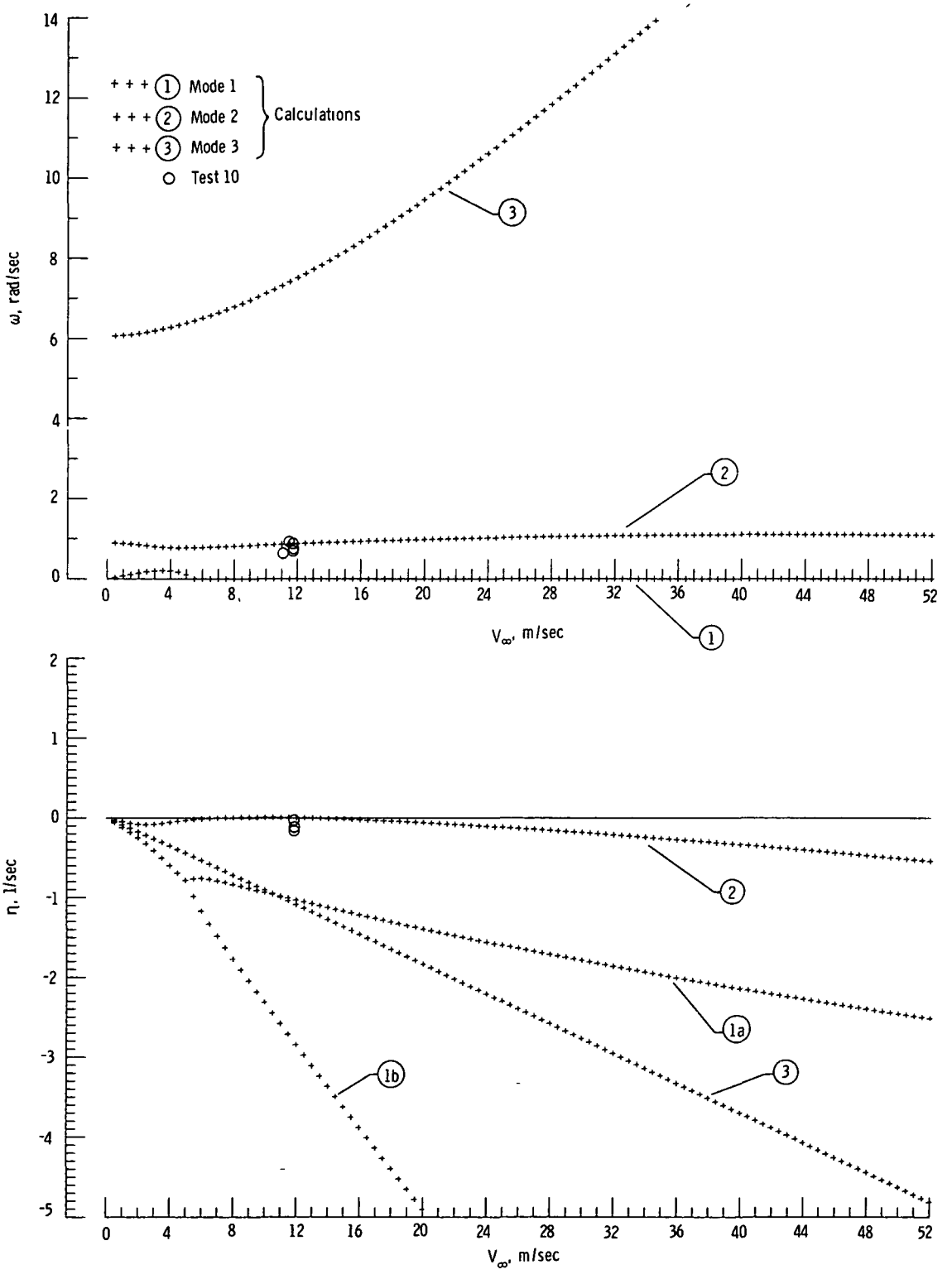

Figure 30.- Variation of lateral stability characteristics ω and η with V_∞ for configuration of test 10.

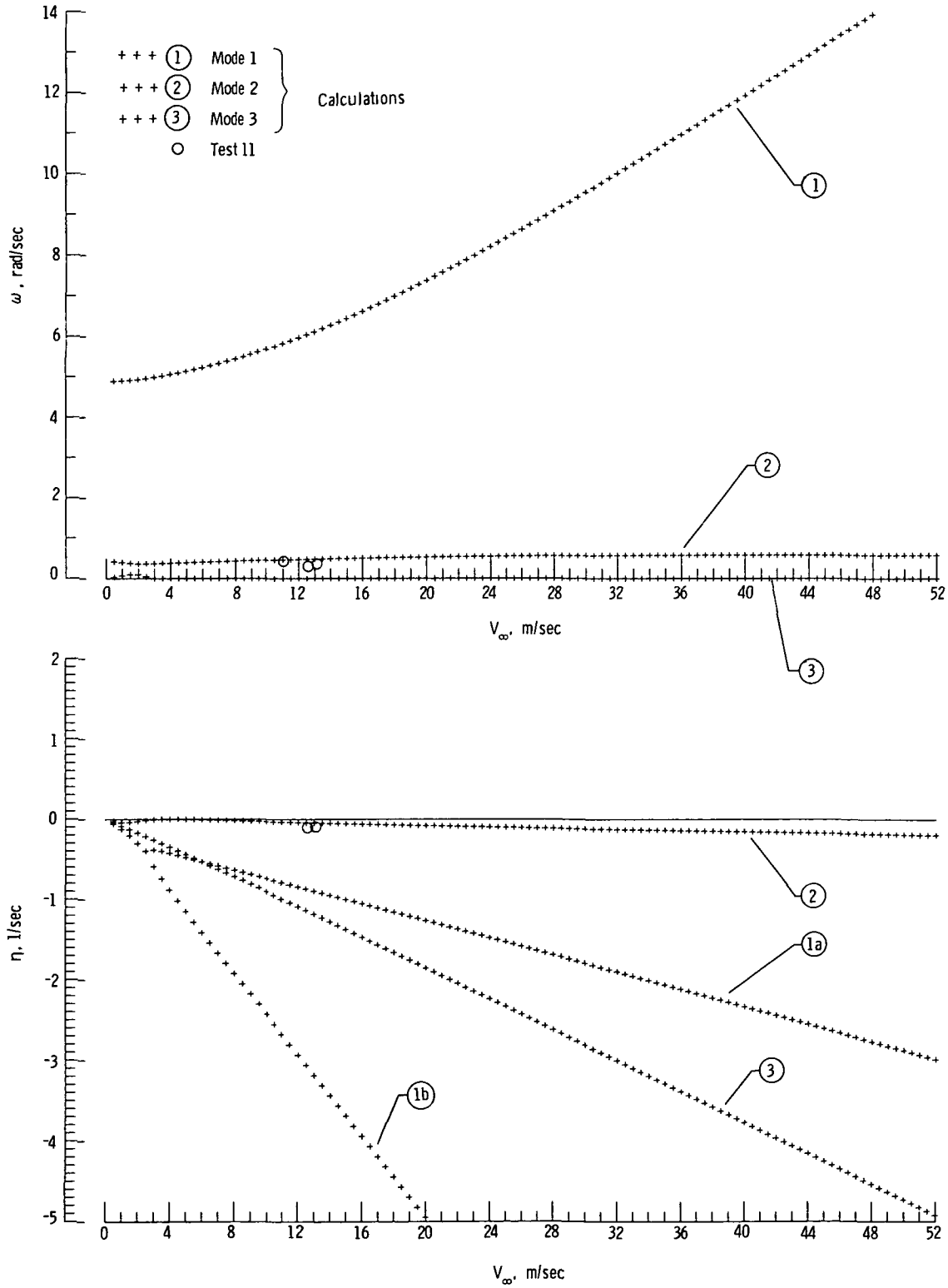

Figure 31.- Variation of lateral stability characteristics ω and η with V_∞ for configuration of test 11.

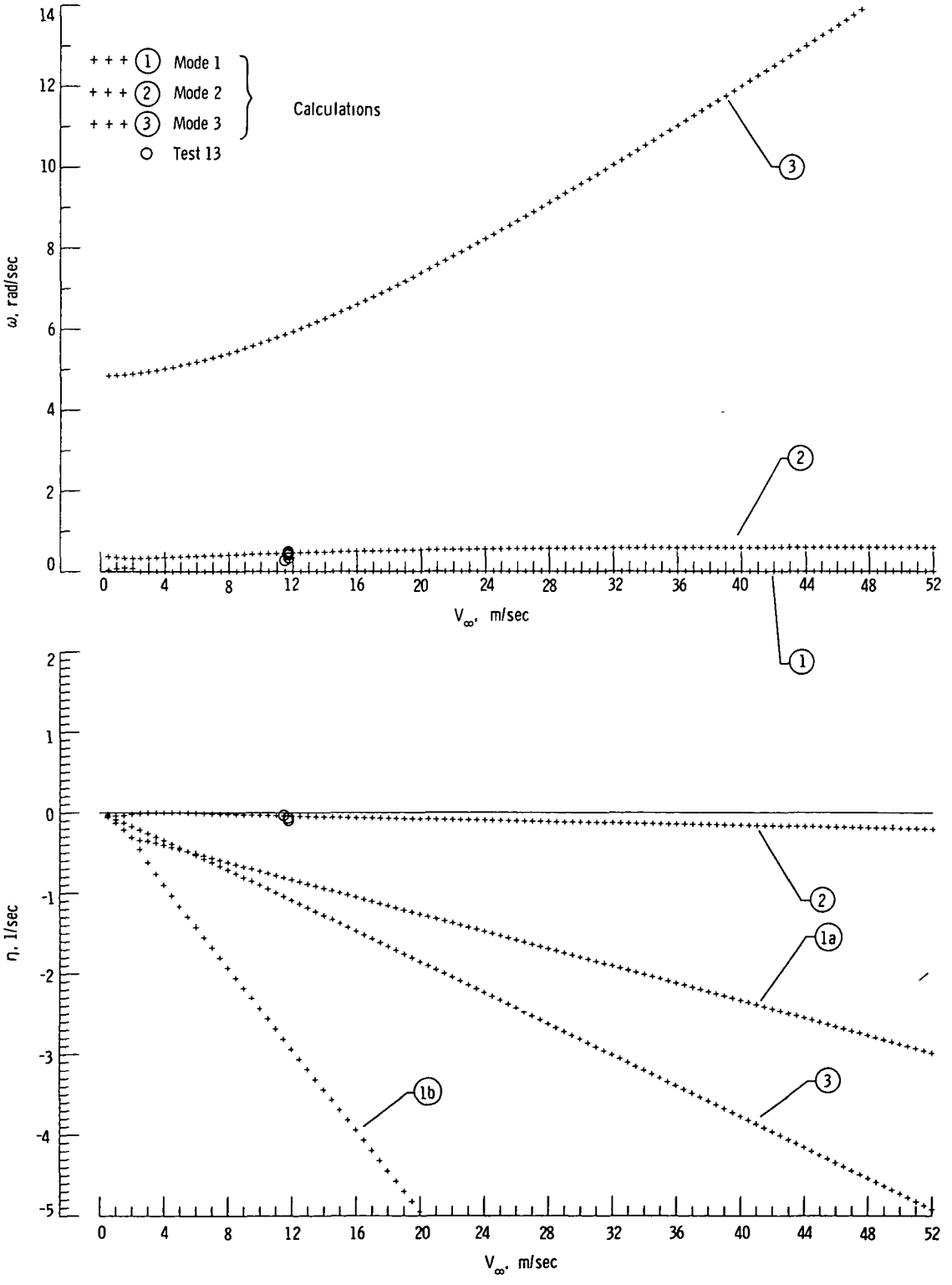

Figure 32.- Variation of lateral stability characteristics ω and η with V_∞ for configuration of test 13.

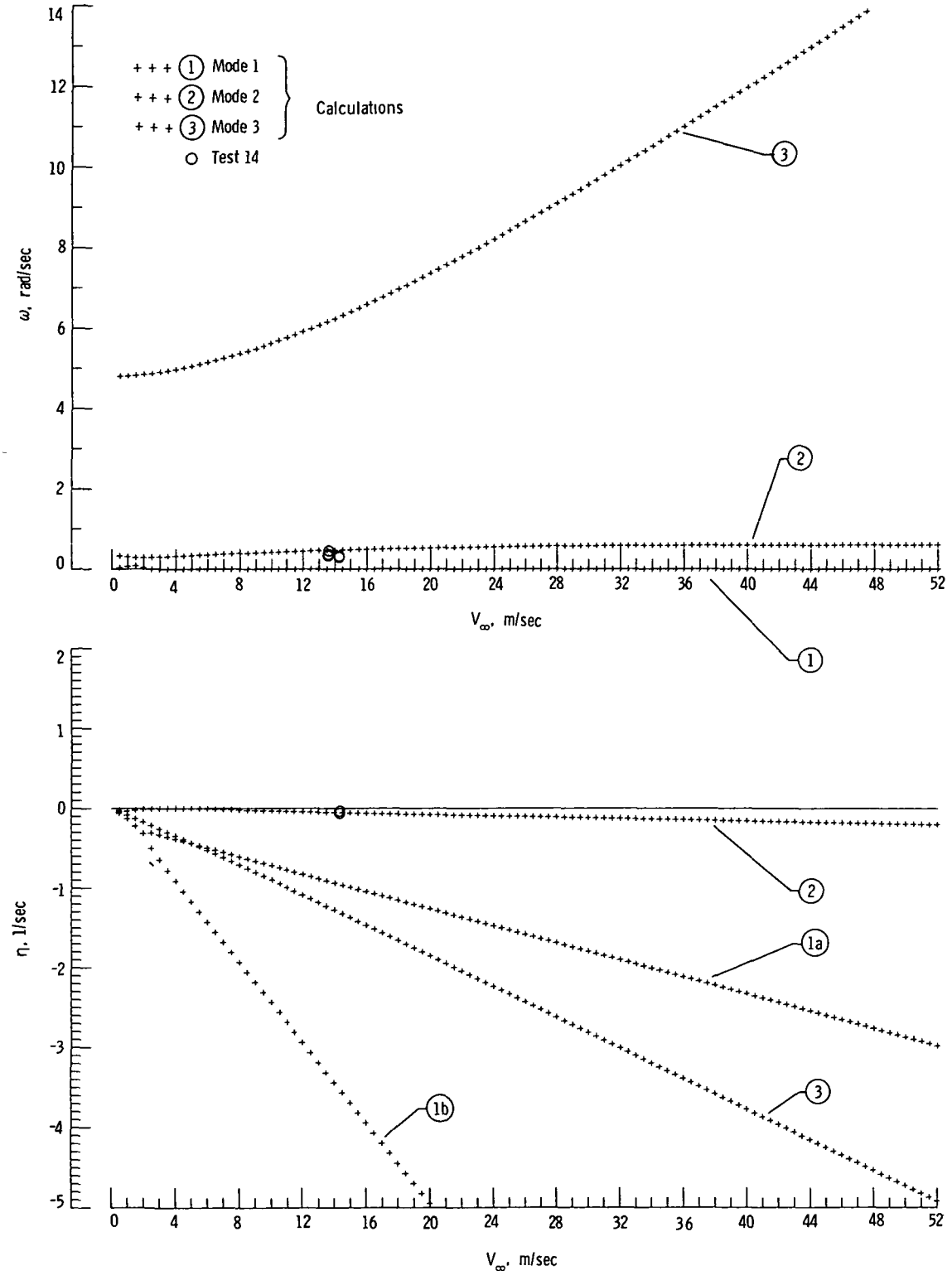

Figure 33.- Variation of lateral stability characteristics ω and η with V_∞ for configuration of test 14.

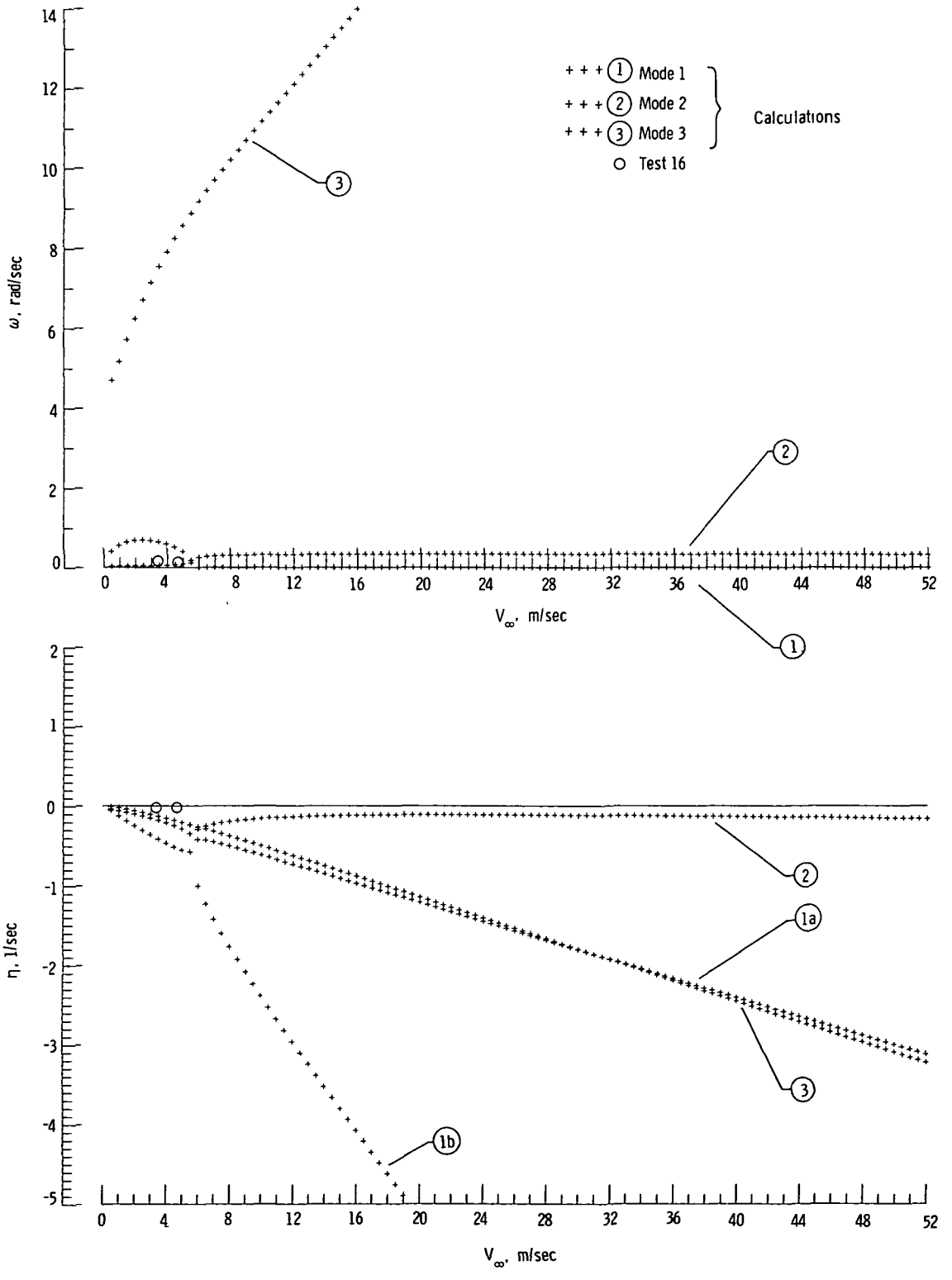

Figure 34.- Variation of lateral stability characteristics ω and η with V_∞ for configuration of test 16.

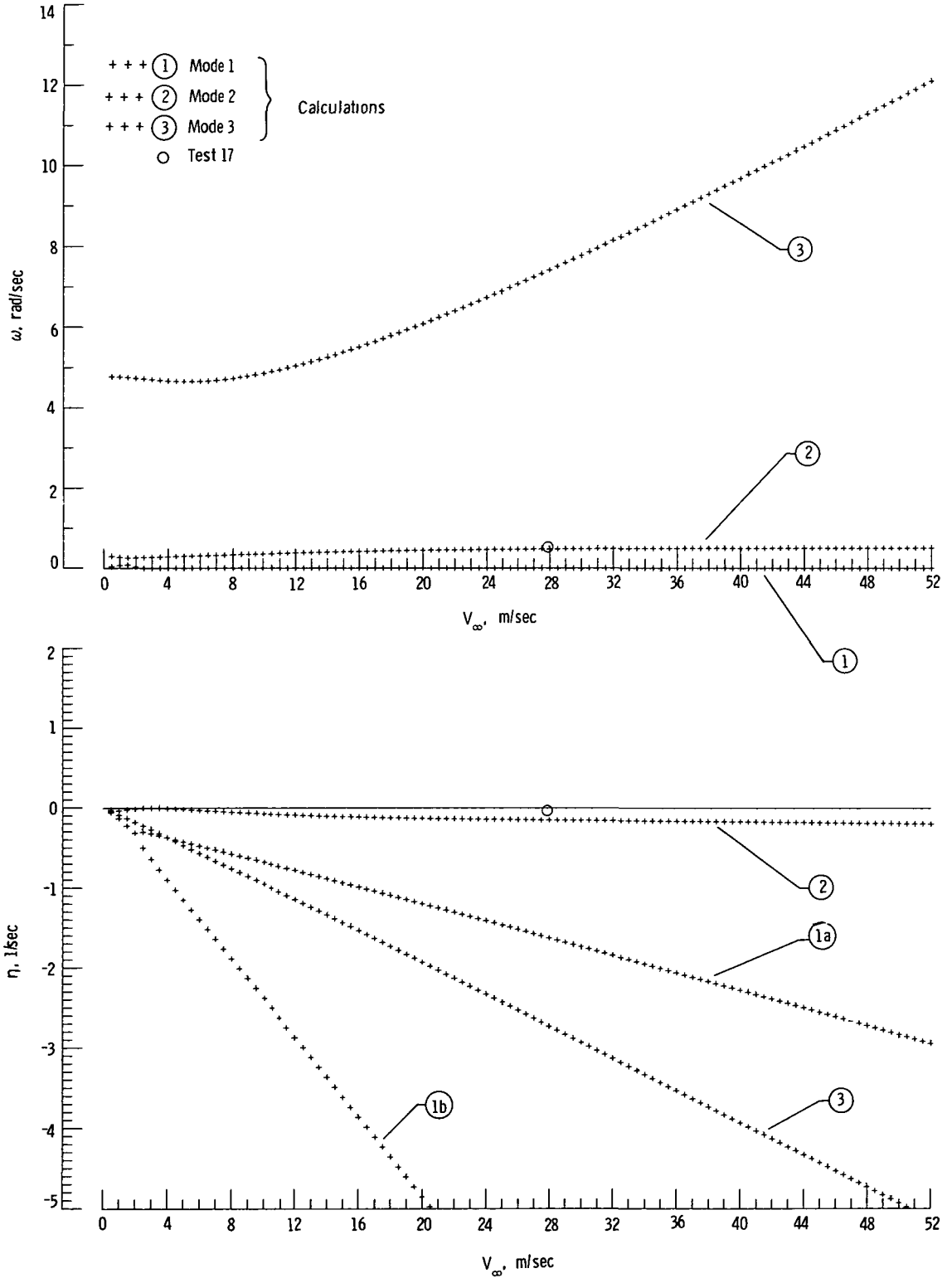

Figure 35.- Variation of lateral stability characteristics ω and η with V_∞ for configuration of test 17.

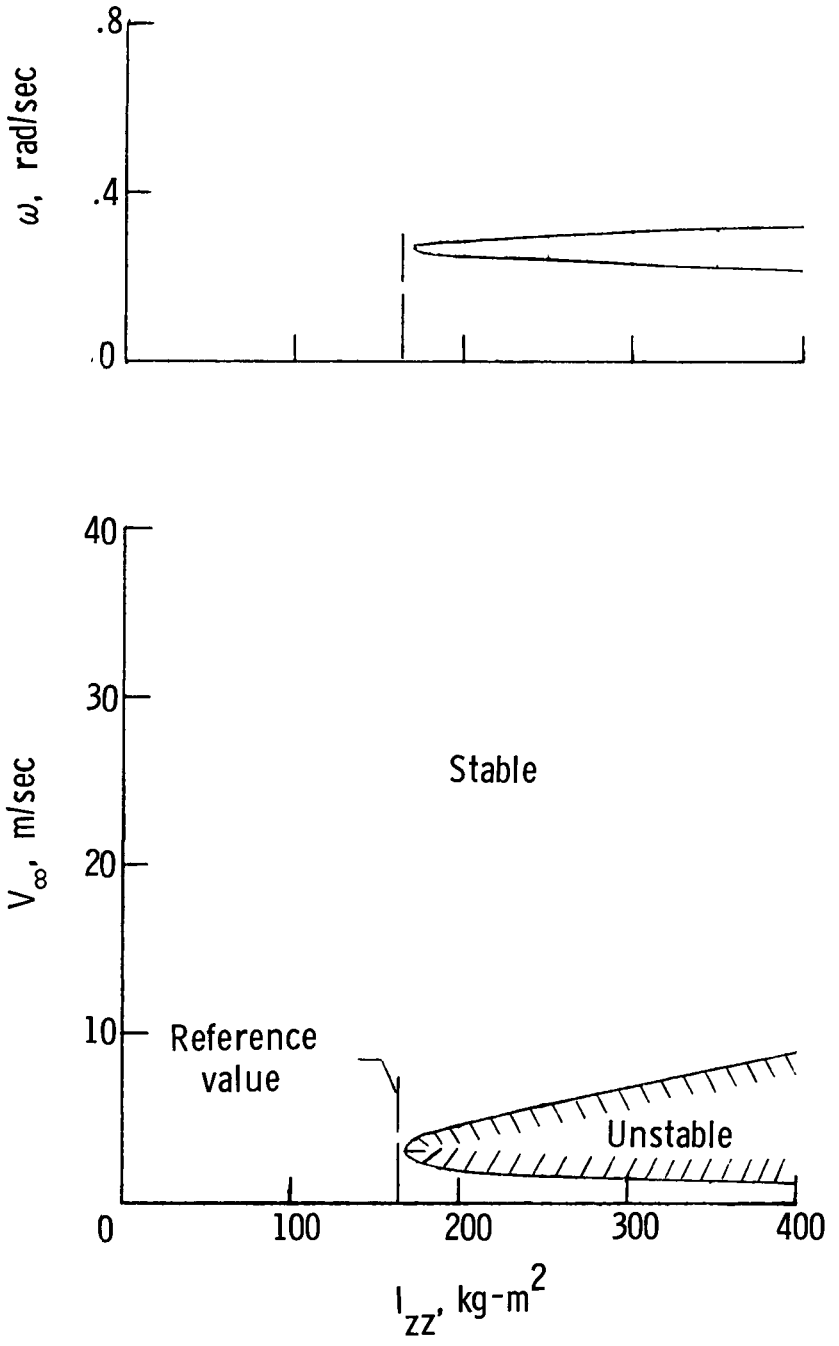

Figure 36.- Effect of I_{zz} on calculated lateral stability boundary.

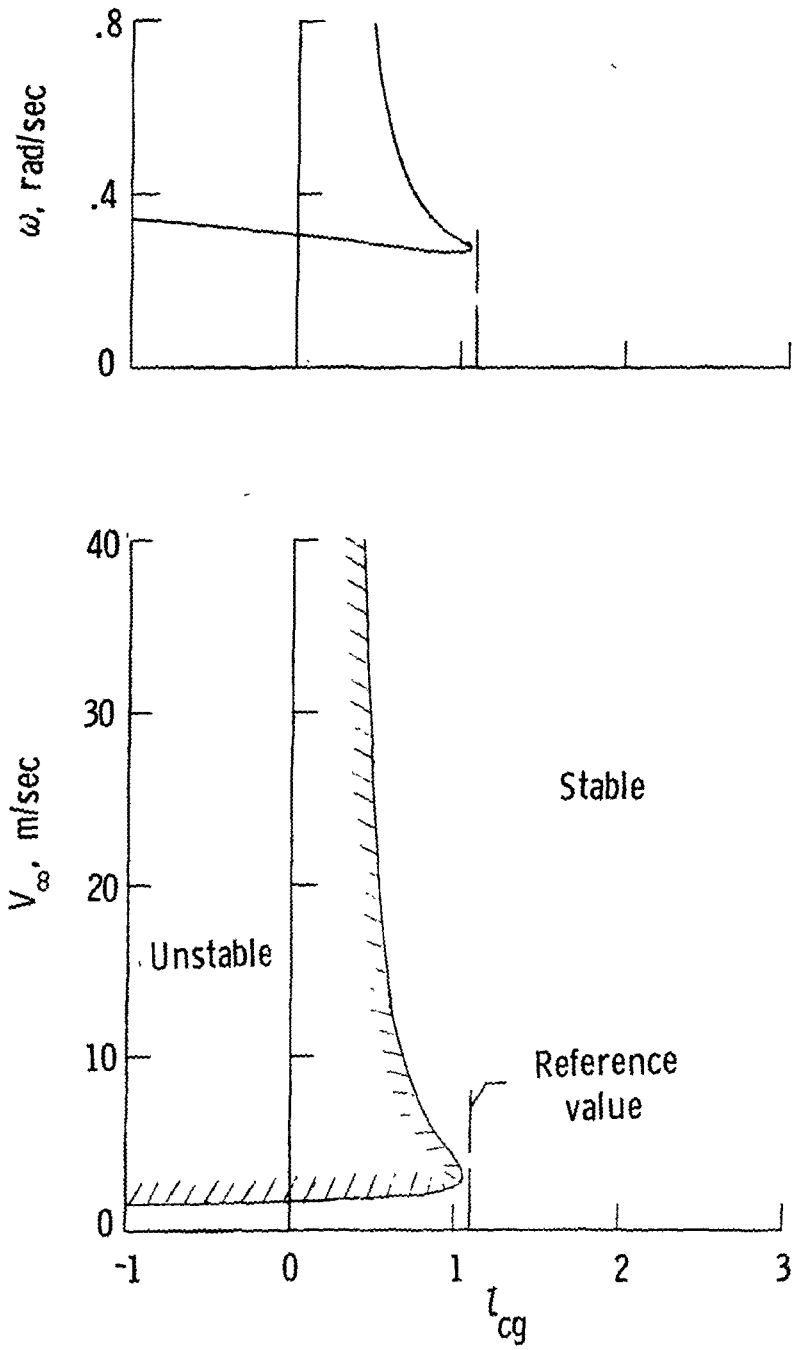

Figure 37.- Effect of l_{cg} on calculated lateral stability boundary.

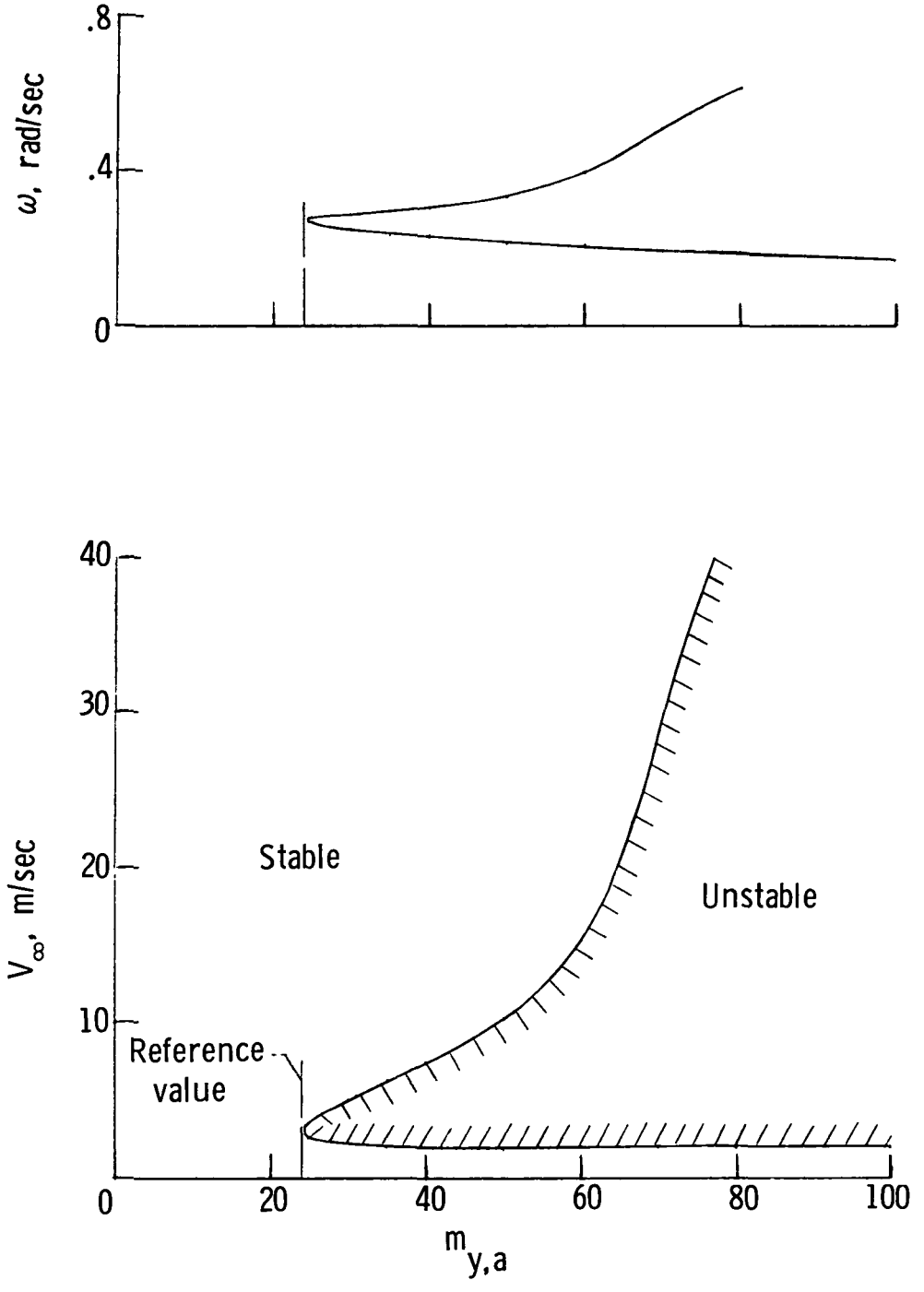

Figure 38.- Effect of apparent mass $m_{y,a}$ on calculated lateral stability boundary.

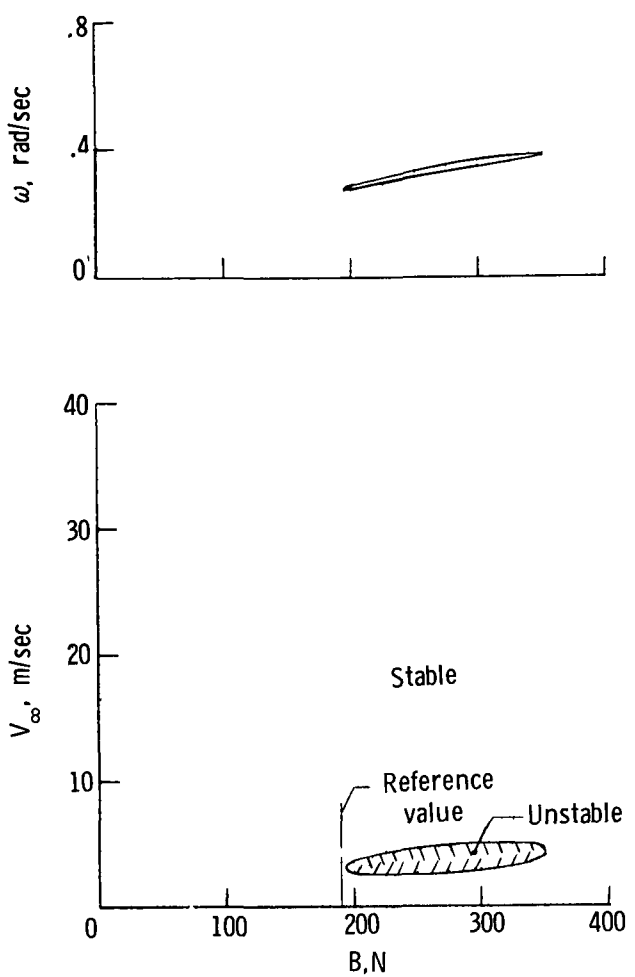

(a) Buoyancy force.

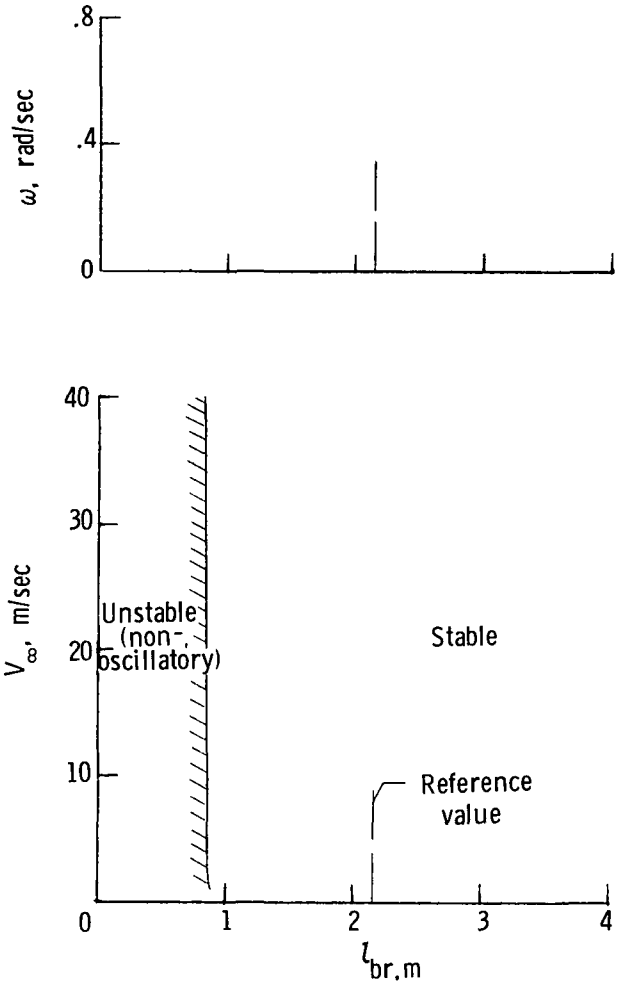

(b) Location of buoyancy force.

Figure 39.- Effect of buoyancy force on calculated lateral stability boundary.

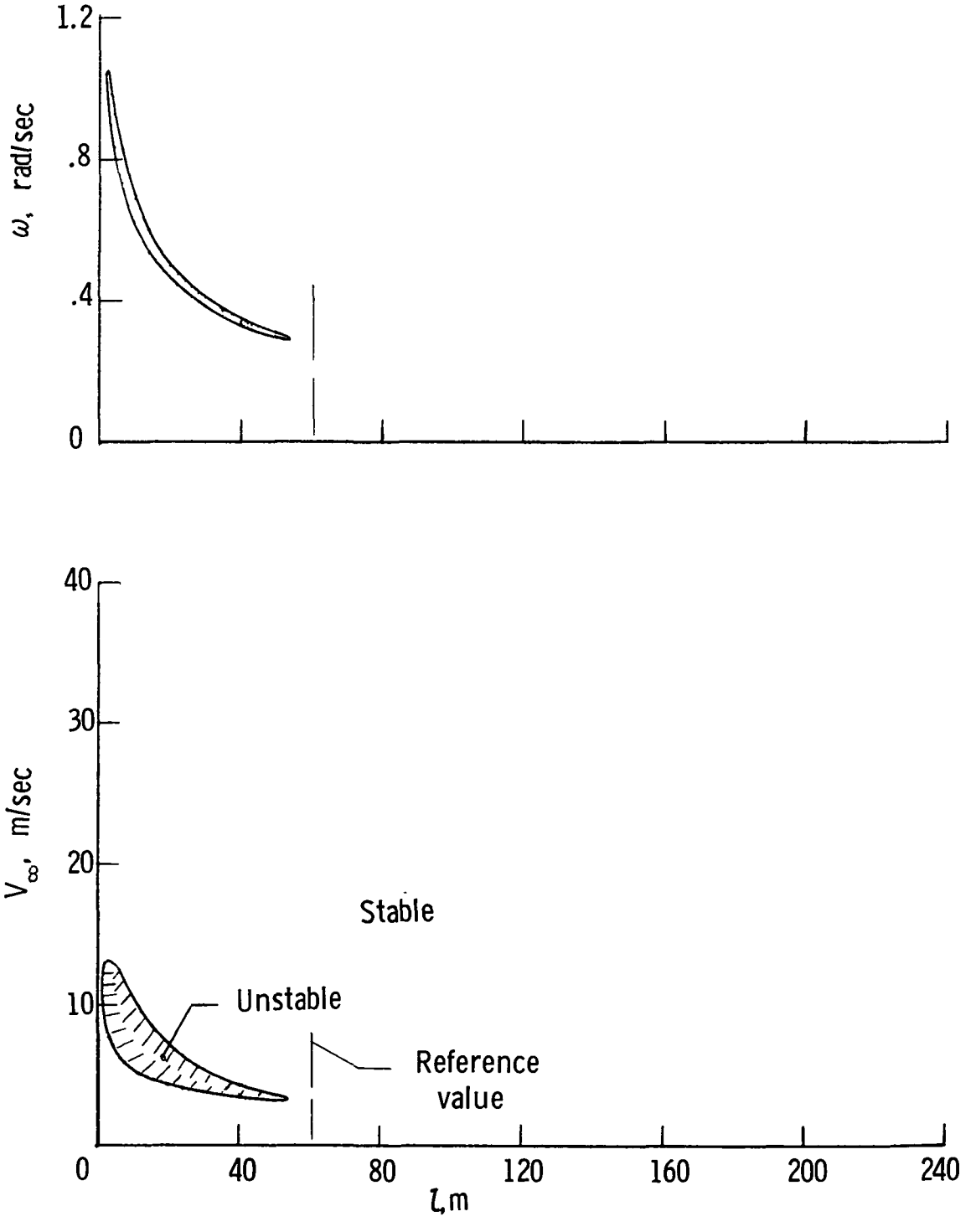

Figure 40.- Effect of tether-cable length on calculated lateral stability boundary.

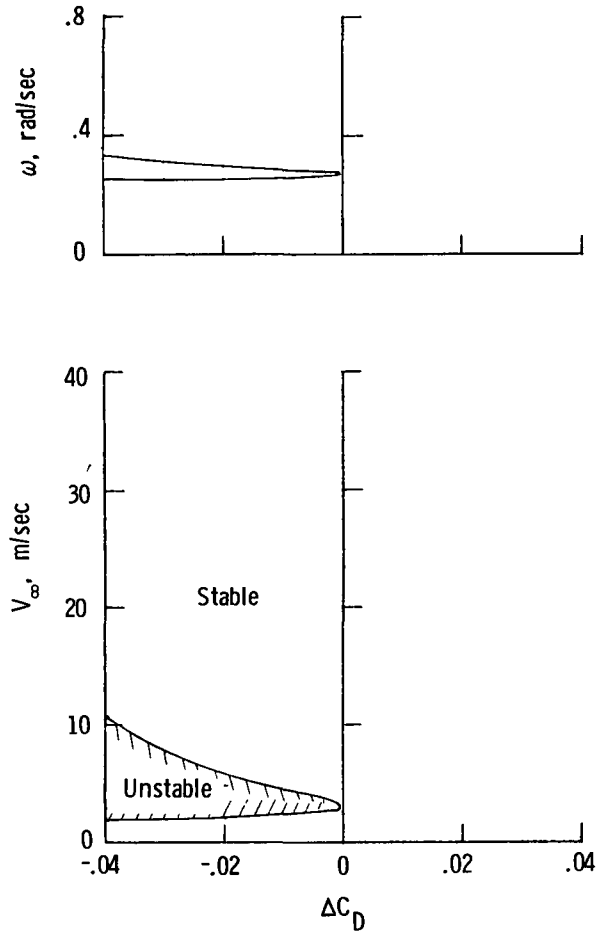

(a) Change in C_D.

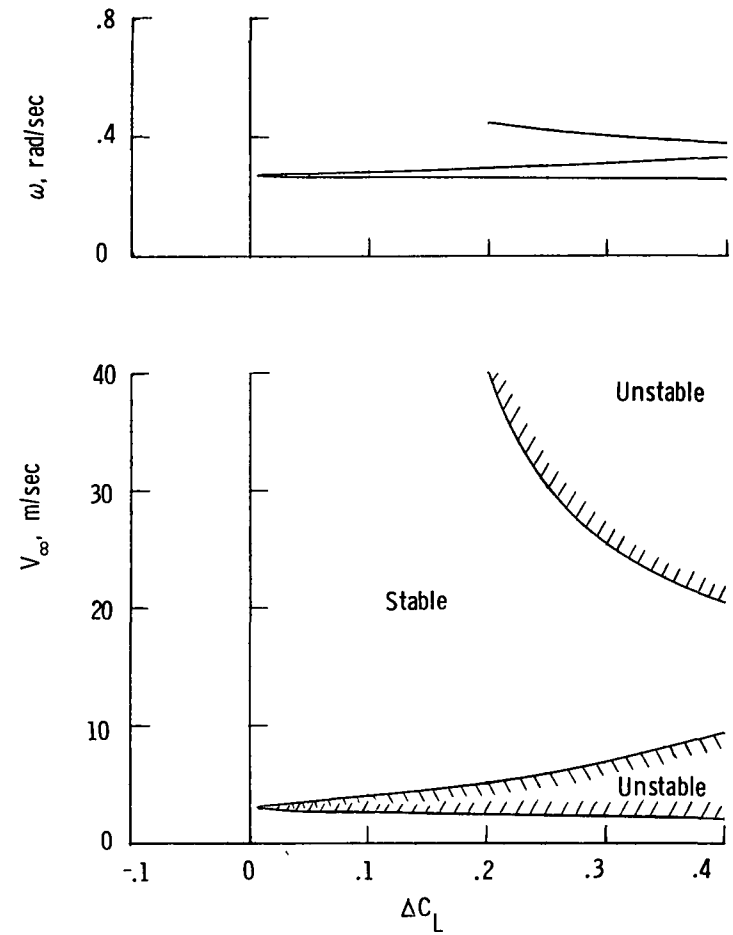

(b) Change in C_L.

Figure 41.- Effect of static aerodynamic coefficients on calculated lateral stability boundary.

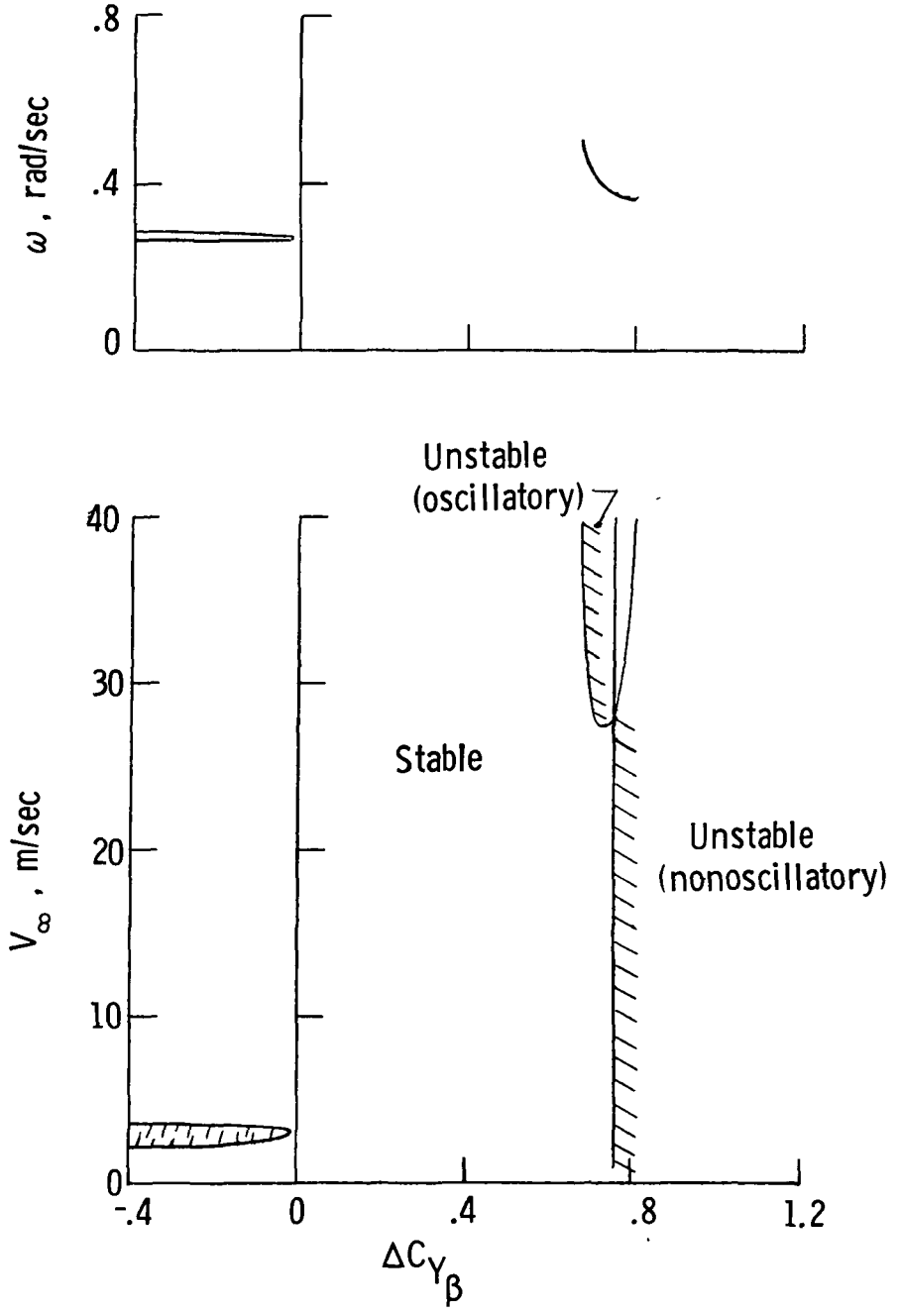

Figure 42.- Effect of ΔC_{Y_β} on calculated lateral stability boundary $\left(C_{Y_\beta} = -0.82 \text{ for reference configuration}\right)$.

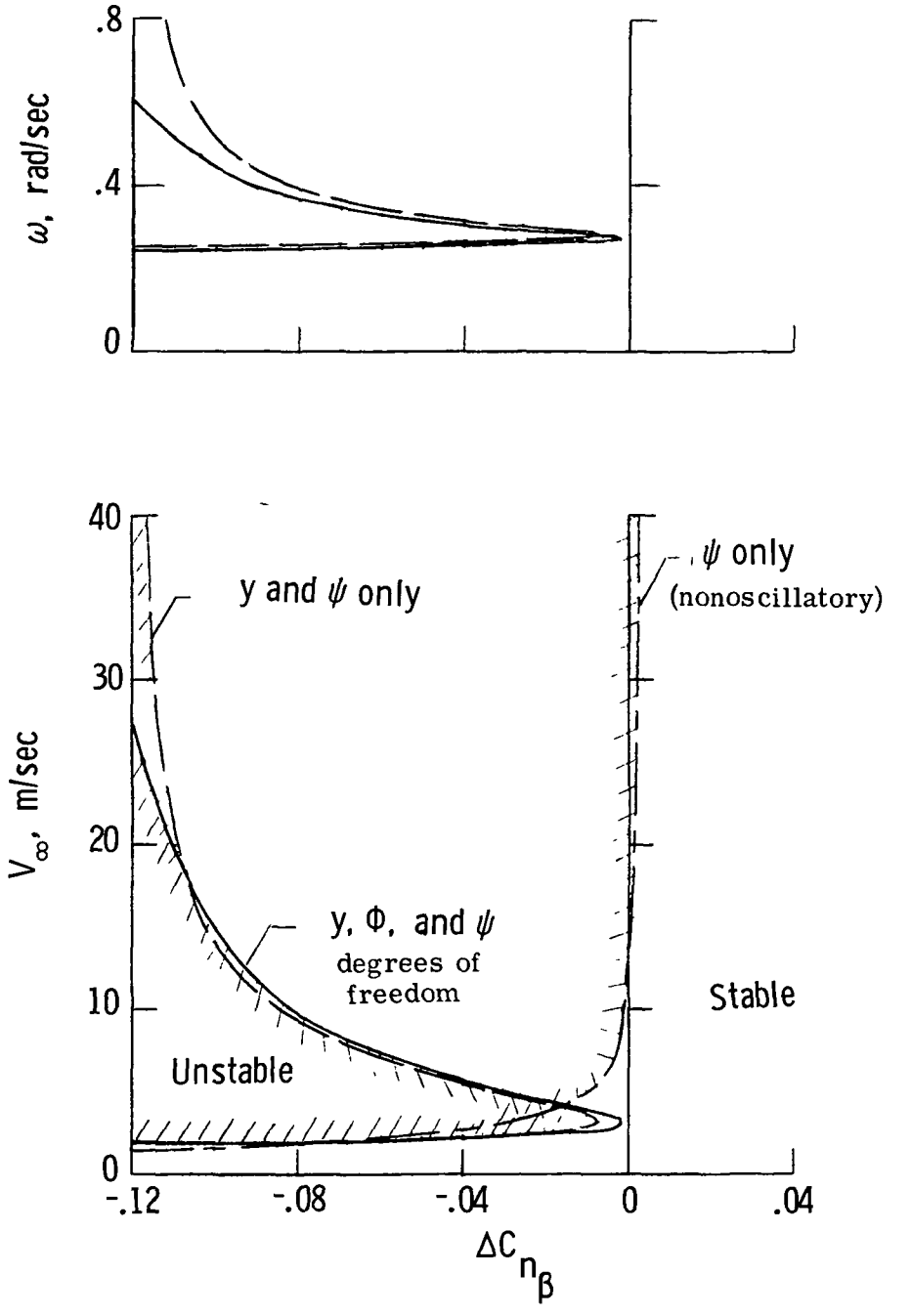

Figure 43.- Effects of including various degrees of freedom and of ΔC_{n_β} on calculated lateral stability boundary $\left(C_{n_\beta} = -0.0254 \text{ for reference configuration}\right)$.

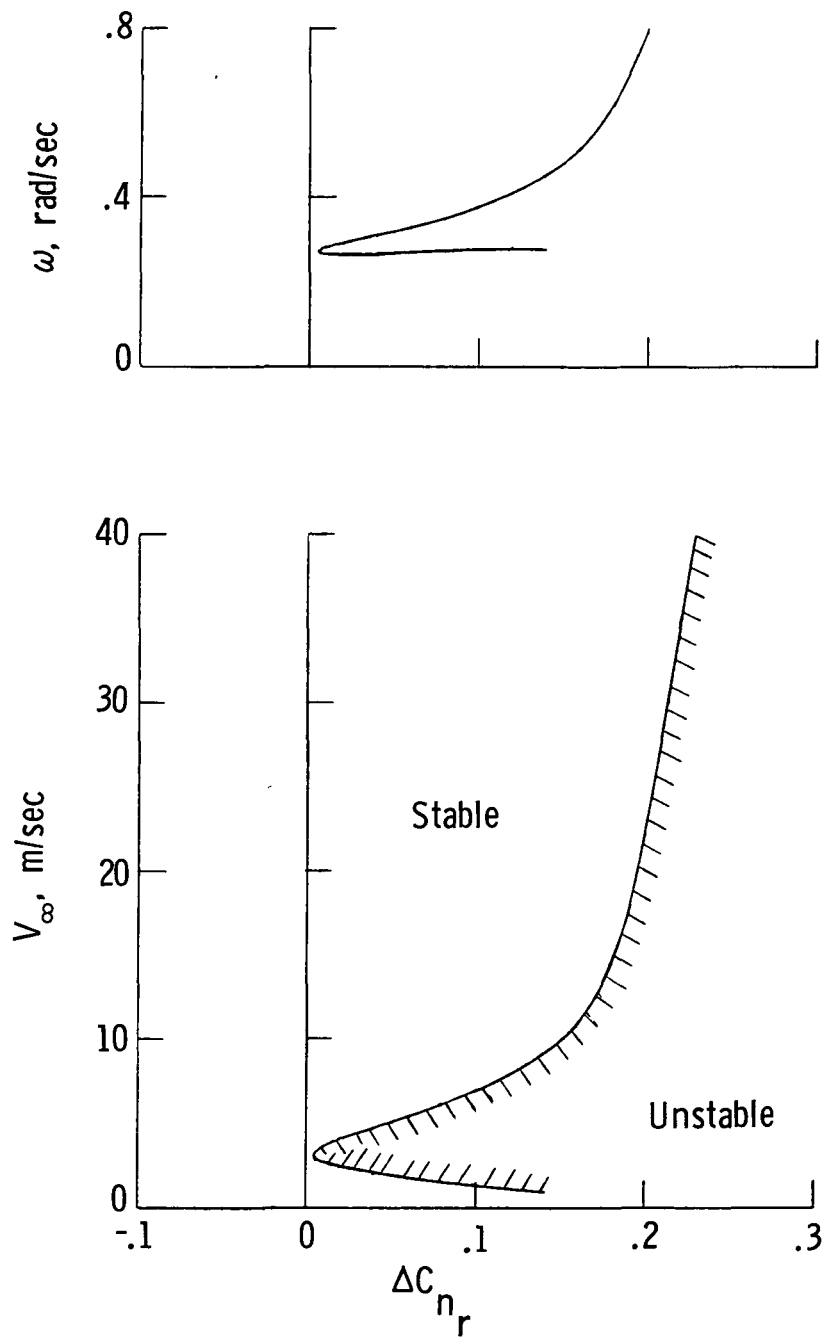

Figure 44.- Effect of ΔC_{n_r} on calculated lateral stability boundary (C_{n_r} = -0.280 for reference configuration).

A motion-picture film supplement L-1118 is available on loan. Requests will be filled in the order received. You will be notified of the approximate date scheduled.

The film (16 mm, 9 min, black and white, silent) shows computer generated longitudinal and lateral modes of motion for the 7.64-meter balloon tethered in steady winds of various velocities.

Film supplement L-1118 is available on request to:

NASA Langley Research Center
Att: Photographic Branch, Mail Stop 171
Hampton, Va. 23665

CUT

Date_____

Please send, on loan, copy of film supplement L-1118 to TN D-7272.

_____
Name of organization

_____
Street number

_____
City and State Zip code

Attention: Mr._____
Title_____

CUT

Place
Stamp
Here

NASA Langley Research Center
Att: Photographic Branch, Mail Stop 171
Hampton, Va. 23665

"The aeronautical and space activities of the United States shall be conducted so as to contribute . . to the expansion of human knowledge of phenomena in the atmosphere and space The Administration shall provide for the widest practicable and appropriate dissemination of information concerning its activities and the results thereof"

—NATIONAL AERONAUTICS AND SPACE ACT OF 1958

NASA SCIENTIFIC AND TECHNICAL PUBLICATIONS

TECHNICAL REPORTS Scientific and technical information considered important, complete, and a lasting contribution to existing knowledge

TECHNICAL NOTES Information less broad in scope but nevertheless of importance as a contribution to existing knowledge

TECHNICAL MEMORANDUMS Information receiving limited distribution because of preliminary data, security classification, or other reasons Also includes conference proceedings with either limited or unlimited distribution.

CONTRACTOR REPORTS Scientific and technical information generated under a NASA contract or grant and considered an important contribution to existing knowledge.

TECHNICAL TRANSLATIONS Information published in a foreign language considered to merit NASA distribution in English

SPECIAL PUBLICATIONS Information derived from or of value to NASA activities Publications include final reports of major projects, monographs, data compilations, handbooks, sourcebooks, and special bibliographies

TECHNOLOGY UTILIZATION PUBLICATIONS Information on technology used by NASA that may be of particular interest in commercial and other non-aerospace applications Publications include Tech Briefs, Technology Utilization Reports and Technology Surveys

Details on the availability of these publications may be obtained from:

SCIENTIFIC AND TECHNICAL INFORMATION OFFICE

NATIONAL AERONAUTICS AND SPACE ADMINISTRATION

Washington, D.C. 20546